

WETTABILITY AND NANOSTRUCTURE EFFECT ON OSCILLATING HEAT PIPES

A Dissertation

presented to

the Faculty of the Graduate School

at the University of Missouri-Columbia

In Partial Fulfillment

of the Requirements for the Degree

Doctor of Philosophy

by

FENG Z. ZHANG

Dr. Hongbin Ma, Dissertation Supervisor

December 2015

The undersigned, appointed by the Dean of the Graduate School, have examined the dissertation entitled

WETTABILITY AND NANOSTRUCTURE EFFECT ON OSCILLATING HEAT PIPES

presented by Feng Zhang,

a candidate for the degree of doctor of philosophy,

and hereby certify that, in their opinion, it is worthy of acceptance.

Professor Hongbin Ma

Professor Robert Winholtz

Professor Gary Solbrekken

Professor Qingsong Yu

Professor Haskell Taub

DEDICATION

To my parents, who have taught me hard work and education are the keys to a successful foundation for life. To Ken and Charlotte Norris, with their continual guidance, it has made my journey throughout this process much easier. To Randall and Kendra Young, who have given me great life advice and most importantly a second family. To my four legged critters, Theo, Luna, and Petri that bring a smile to my face every day.

Finally to my wife, Sydney Young, whose love and support never wavered especially through the tough times.

ACKNOWLEDGEMENTS

I would like to thank Dr. Hongbin Ma for his support and guidance throughout my education and research. Dr. Robert Winholtz became a great source for general advice on my graduate studies. Dr. Haskell Taub helped tremendously through giving me the opportunity to participate and learn in the National Science Foundation Integrated Graduate Education and Research Traineeship (NSF IGERT). A special mention must be made for Dr. Matt Maschmann for his regular advice and wonderful enthusiasm on novel ideas. I'd like to thank my colleagues present and past, Mike Wilson, Hanwen Lu, Dr. Aaron Hathaway, and Dr. Chris Smoot in their continual support and refreshing conversations throughout my many years in school. I cannot forget my favorite administrative tag team of Melanie Carraher and Marilyn Nevels for making bureaucracy more manageable along with excellent, humorous daily conversation.

TABLE OF CONTENTS

LIST OF FIGURES.....	v
LIST OF TABLES.....	ix
ABSTRACT.....	x
1 INTRODUCTION.....	1
1.1 THERMAL PROBLEM.....	1
1.2 CONVENTIONAL HEAT PIPES.....	1
1.3 OSCILLATING HEAT PIPES.....	4
1.3.1 Features of an OHP.....	6
1.4 REVIEW OF THE WETTABILITY OF THE OHP.....	6
1.5 RESEARCH OBJECTIVES.....	8
2 FABRICATION.....	10
2.1 TRADITIONAL MACHINING METHODOLOGY.....	10
2.2 CERAMIC OHP METHODOLOGY WITH ALUMINUM NITRIDE.....	13
2.2.1 Powder Preparation.....	14
2.2.2 Shaping Processes.....	16
2.2.3 OHP Integration into AlN.....	22
2.2.4 Sintering.....	27
2.3 SEALING.....	29
2.3.1 Brazing.....	29
2.3.2 Aluminum Brazing.....	31
2.3.3 Mechanical, Adhesive, and Groove (MAG) Technique.....	34
2.4 CHARGING.....	37
2.5 SUMMARY.....	39
3 PARTIALLY HYDROPHILIC FP-OHP WITH NEUTRON RADIOGRAPHY.....	41
3.1 EXPERIMENTAL INVESTIGATION.....	42
3.1.1 FP-OHP CNC Fabrication.....	42
3.1.2 Nanostructure Growth.....	43
3.1.3 Characterization.....	43

3.1.4	Assembling and Charging	45
3.2	THERMAL TESTING AND NEUTRON IMAGING.....	45
3.3	RESULTS	48
3.4	SUMMARY	58
4	HYBRID SUPERHYDROPHOBIC/SUPERHYDROPHILIC OSCILLATING HEAT PIPE	59
4.1	EXPERIMENTAL INVESTIGATION	59
4.1.1	FP-OHP CNC Fabrication.....	59
4.1.2	Nanostructure Growth	61
4.1.3	Plasma Polymer Nanocoating Deposition.....	62
4.1.4	Characterization	63
4.1.5	Assembling and Charging	66
4.2	THERMAL TESTING	67
4.3	RESULTS	69
4.4	SUMMARY	76
5	OPERATING LIMIT OF AN OSCILLATING HEAT PIPE	77
5.1	INTRODUCTION	77
5.2	THEORETICAL MODEL.....	80
5.3	RESULTS AND DISCUSSION	88
5.4	SUMMARY	96
6	CONTACT ANGLE EFFECT ON THE OSCILLATING MOTION OF AN OSCILLATING HEAT PIPE ..	97
6.1	INTRODUCTION	97
6.2	THEORETICAL MODEL.....	98
6.3	RESULTS	103
6.4	SUMMARY	109
7	CONCLUSIONS.....	110
8	REFERENCES.....	113
	VITA.....	119

LIST OF FIGURES

Figure 1.1. Schematic of a conventional heat pipe.	2
Figure 1.2. Schematic of tubular OHP (left) and flat plate OHP (right)	5
Figure 1.3. SEM images from Qu et al.[9] (a) clean substrate boiled in pure water, (b) a nanoparticle deposited substrate at the condenser, and (c) a nanoparticle-deposited substrate at the evaporator.	7
Figure 2.1. Miniature OHP at 12 mm x 100 mm with 0.5 mm square channels.	11
Figure 2.2. Flat Plate OHP with geometry of 10.16 mm x 10.16 mm.	11
Figure 2.3. A different version of a 10.16 mm x 10.16 mm Flat Plate OHP.	12
Figure 2.4. Dry press system: (a) powder added to die, (b) pressure applied to compact powder, (c) compacted powder release, (d) process starts again [17].	17
Figure 2.5. Slurry system: (a) initial pouring of slurry into mold; (b) particles build up as liquid is absorbed through the permeable material; and (c) the slip casting surface is separated leaving the cast mold.	18
Figure 2.6. Tool hardened steel dies.	19
Figure 2.7. Acrylic mold greased with silicone.	19
Figure 2.8. Dry pressed AlN piece	20
Figure 2.9. Slip casted AlN piece.	20
Figure 2.10. Machined green body AlN with impregnated gypsum.	21
Figure 2.11. First concept OHP cavity designs.	23
Figure 2.12. Smaller OHP cavity designs at 1 in x 1 in.	24
Figure 2.13. OHP cavity with plastic mold.	24
Figure 2.14. Slip casted AlN with impregnated OHP cavity.	25
Figure 2.15. Crack development minutes after removal from mold.	26
Figure 2.16. Major crack development after one day.	26
Figure 2.17. Dry pressed OHP integration: (left) burnout of plastic OHP cavity, (right) original green body with OHP cavity.	27
Figure 2.18. Microstructural changes during high temperatures. (a) green body structure, (b) coalescence of particles begin, (c) final sintering structure [17].	28
Figure 2.19. Schematic of brazing process.	29
Figure 2.20. Brazing temperature versus time for OHP.	31
Figure 2.21. Magnesium chips after the brazing process.	32
Figure 2.22. Rough aluminum after brazing process.	33
Figure 2.23. Edge machined to see the brazed attachment.	33
Figure 2.24. Explode version of a flat plate OHP with cover plate.	34
Figure 2.25. Cross sectional view of the tongue and groove.	35

Figure 2.26. View of the OHP tongue.	36
Figure 2.27. View of the cover plate groove.....	36
Figure 2.28. EPOTEK-301 epoxy set.	37
Figure 2.29. Charging system.....	38
Figure 2.30. Charging ports for vacuum, fluid, and OHP.	39
Figure 3.1. Schematic of the FP-OHP investigated (all dimensions in mm). Purple circles indicate thermocouple location. Blue dashed line is the condenser section, green dashed line indicates the adiabatic section and red dashed line indicates the evaporator section.	41
Figure 3.2. Fabricated FP-OHP without the cover plate.	42
Figure 3.3. SEM images of the CuO nanostructures with magnifications of 10,000X (left) and 138,061X (right).	44
Figure 3.4. Sessile drop test on nontreated copper at 60 degrees contact angle (left) and treated copper with CuO surface nanostructures (right), showing a hydrophilic contact angle of about 12 degrees.....	44
Figure 3.5. Schematic of the entire experimental setup at the NCNR.	46
Figure 3.6. Detailed view of the thermal portion of the experimental setup.	47
Figure 3.7. Thermal resistance plot with changing input power.	49
Figure 3.8. Temperature difference as a function of power input.	50
Figure 3.9. Liquid and vapor distribution in the condenser nanostructures configuration at a power input of 75 W.	52
Figure 3.10. Liquid and vapor distribution in the condenser nanostructures configuration at a power input of 225 W.	53
Figure 3.11. Liquid and vapor distribution in the evaporator nanostructures configuration at a power input of 115 W.	53
Figure 3.12. Liquid and vapor distribution in the evaporator nanostructures configuration at power input of 225 W.	54
Figure 3.13. CuO in evaporator temperature difference measurements with data after 1.5 years.	55
Figure 3.14. CuO in condenser temperature difference measurements with data after 1.5 years.	56
Figure 3.15. Comparison of average performance 1.5 years later to the original untreated OHP.	57
Figure 3.16. Temperature difference plot of a nanofluid OHP comparison from Ma et al [8]. ...	57
Figure 4.1. Schematic of a large FP-OHP investigated (all dimensions in mm). Purple circles indicate thermocouple location. Blue dashed line is the condenser section, green dashed line indicates the adiabatic section and red dashed line indicates the evaporator section.	60
Figure 4.2. Fabricated FP-OHP with cover plate.	61

Figure 4.3. Template to cover hydrophilic FP-OHP and expose surface for plasma polymer treatment.....	63
Figure 4.4. SEM image of the CuO nanostructures with magnification of 100,00X.....	64
Figure 4.5. Contact angle measurements; (a) sessile drop test on a treated CuO (top) with contact angle of 0°; (b) nontreated copper (middle) with contact angle ~60°; and (c) a treated CuO with an additional plasma polymer layer with contact angle of ~152°-154°.....	65
Figure 4.6. XPS analysis.....	66
Figure 4.7. Schematic of the entire experimental setup.....	68
Figure 4.8. Comparison of temperature difference with multiple runs of the hybrid FP-OHP....	70
Figure 4.9. Thermal resistance versus power input.....	71
Figure 4.10. Condenser temperature comparison as a function of power input.....	72
Figure 4.11. Evaporator temperature comparison as a function of power input.....	72
Figure 4.12. Steady state temperature oscillation in the evaporator at 100 W.....	73
Figure 4.13. Normalized temperature oscillations at 100 W heat input in the evaporator.....	74
Figure 4.14. Temperature oscillations in condenser at 100 W heat input.....	74
Figure 4.15. Normalized temperature oscillations in condenser at 100 W heat input.....	75
Figure 4.16. Standard deviation comparison of the evaporation temperature versus power. ..	75
Figure 4.17. Standard deviation comparison of the condenser temperature versus power.....	76
Figure 5.1. Taylor bubble [44].....	78
Figure 5.2. Flow regime [44].....	78
Figure 5.3. Top is a small scale FP-OHP design using neutron radiography [38], Bottom is a much larger 12 turn 3D tubular OHP size [33].....	79
Figure 5.4. Taylor bubble schematic from Bretherton [41].....	80
Figure 5.5. Schematic of the thin film region where b is the film thickness [41].....	81
Figure 5.6. Experimental data from Taylor 1961 [37].	82
Figure 5.7. Han and Shikazono results comparing working fluid [43].	83
Figure 5.8. Schematic of a typical slug flow with the film thickness in a tube.....	84
Figure 5.9. Schematic of an initial condition case where there is no movement and no film thickness.	85
Figure 5.10. Schematic of limiting case where flow is annular.	86
Figure 5.11. Radius effect on the maximum film thickness with water at 100°C, length of 20 cm and charging ratio of 50%.	88
Figure 5.12. Radius effect on the velocity with water at 100°C, length of 20 cm and charging ratio of 50%.	89
Figure 5.13. Radius effect on the maximum heat transfer rate with water at 100°C, length of 20 cm and charging ratio of 50%.	89
Figure 5.14. Charging ratio effect on the film thickness with water at 100°C, length of 20 cm and radius of 1 mm.	91

Figure 5.16. Charging ratio effect on velocity with water at 100°C, length of 20 cm and radius of 1 mm.	91
Figure 5.17. Charging ratio effect on the maximum heat transfer rate with water at 100°C, length of 20 cm and radius of 1 mm.	92
Figure 5.18. Length effect on film thickness with water at 100°C, radius of 1 mm and charging ratio of 50%.	92
Figure 5.19. Length effect on the velocity with water at 100°C, radius of 1 mm and charging ratio of 50%.	93
Figure 5.20. Length effect on the maximum heat transfer rate with water at 100°C, radius of 1 mm and charging ratio of 50%.	93
Figure 5.21. Acetone as working fluid at 100°C, length of 20 cm, and charging ratio of 50%.	94
Figure 5.22. Refrigerant 123 as working fluid at 100°C, length of 20 cm, and charging ratio of 50%.	95
Figure 5.23. Comparison of three different working fluids at 100°C, length of 20 cm, and charging ratio of 50%.	95
Figure 6.1. Schematic of liquid plug(the dotted line is the equilibrium angle while the solid lines near FS, R, FS, A are the receding and advancing contact angle forces when there is a movement).....	98
Figure 6.2. Position with various contact angles (Water is the working fluid with the following parameters: $L=25\text{mm}$, $D=1\text{mm}$, $\phi=50\%$, $T_e=40^\circ\text{C}$, $\Delta T=3^\circ\text{C}$).	103
Figure 6.3. Peak Position as a function of contact angle (working fluid is water).	104
Figure 6.4. Velocity with various contact angles (water is the working fluid with the following parameters: $L=25\text{mm}$, $D=1\text{mm}$, $\phi=50\%$, $T_e=40^\circ\text{C}$, $\Delta T=3^\circ\text{C}$).	105
Figure 6.5. Peak velocity as a function of contact angle.	106
Figure 6.6. Position effect from contact angle (acetone is working fluid change with parameters: $L=25\text{mm}$, $D=1\text{mm}$, $\phi=50\%$, $T_e=60^\circ\text{C}$, $\Delta T=3^\circ\text{C}$).	107
Figure 6.7. Velocity effect from contact angle (acetone is working fluid change with parameters: $L=25\text{mm}$, $D=1\text{mm}$, $\phi=50\%$, $T_e=60^\circ\text{C}$, $\Delta T=3^\circ\text{C}$).	108

LIST OF TABLES

Table 2.1. Comparison of ceramic material..... 14
Table 2.2. Material selection matrix. 22
Table 5.1. List of relevant nondimensional numbers. 81

ABSTRACT

As electronics technologies rapidly develop with a demand for more power and miniaturization, effective thermal management of these systems becomes much more important. The oscillating heat pipe (OHP) is a promising highly efficient heat transfer device that is great for high heat flux applications common in the electronics industry. In the current investigation, the wettability effect on the heat transfer performance of OHPs has been conducted:

- 1) Extensive experimental investigation of the inner surface wettability on the heat transfer performance of an OHP has been conducted. The inner surface of OHP evaporator was first treated to determine whether the hydrophilic surface treatment can enhance the heat transfer performance. Then, an experimental investigation of hybrid half hydrophilic/half hydrophobic OHP was conducted to determine their effects on the oscillating amplitude, frequency and heat transfer performance. The overall performance of configuration of hydrophilic evaporator/ hydrophobic condenser and hydrophobic evaporator/ hydrophilic condenser was worse than the nontreated OHP, however; the oscillations were much damper when comparing the amplitudes.
- 2) In order to visualize the wettability effect on the oscillating motion and frequency, neutron image technology has been utilized to study the hydrophilic surface effect on the oscillating motion. An OHP with dimensions of 88 mm x 40 mm was fabricated and tested. Results show that high oscillating motion occurs in the OHP

with the hydrophilic surface while low oscillating motion occurs in the untreated OHP.

- 3) In order to find the mechanism how the wettability affects the oscillating motion and amplitude, a mathematical model was developed. The model considers the effects of frictional force, driving force, and receding and advancing contact angles. Results show that as contact angle increases the oscillating motion decreases.
- 4) In addition, based on the Taylor bubble flow, a theoretical model predicting the operating limitation is developed. The model considers the effects of radius of the channel, charging ratio, length of the OHP, and multiple working fluids. Results show that radius and charging ratio has a large effect on the maximum heat transfer limit while length has a relatively small contribution. When comparing working fluids such as water, acetone, and R123, water has a significantly higher upper heat transfer limit than acetone and R123.

1 INTRODUCTION

1.1 THERMAL PROBLEM

With demand for high powered electronic components and packaging, thermal management has become one of the critical bottlenecks posing many engineering challenges. The types of applications can range from central processing units (CPUs) to light emitting diodes (LEDs). Even large scale systems such as supercomputers, power plants, and military avionics can find huge benefits utilizing highly efficient thermal solutions.

1.2 CONVENTIONAL HEAT PIPES

Passive two-phase heat transfer devices that do not require an active power are extremely attractive solutions to the ever increasing energy demands. Conventional heat pipes (CHP) are one of these types of passive thermal technologies as seen in Figure 1.1. The first use of fluids as a way of enhancing heat transfer in a tube is credited to Perkins and Buck in a United Kingdom patent in 1892 [1]. The use of a wick structure in a two phase device was not conceived until 1944 by Gaugler [2]. However interest in CHPs did not occur until space exploration began. The name “heat pipe” was first coined by Grover et al in 1964 [3].

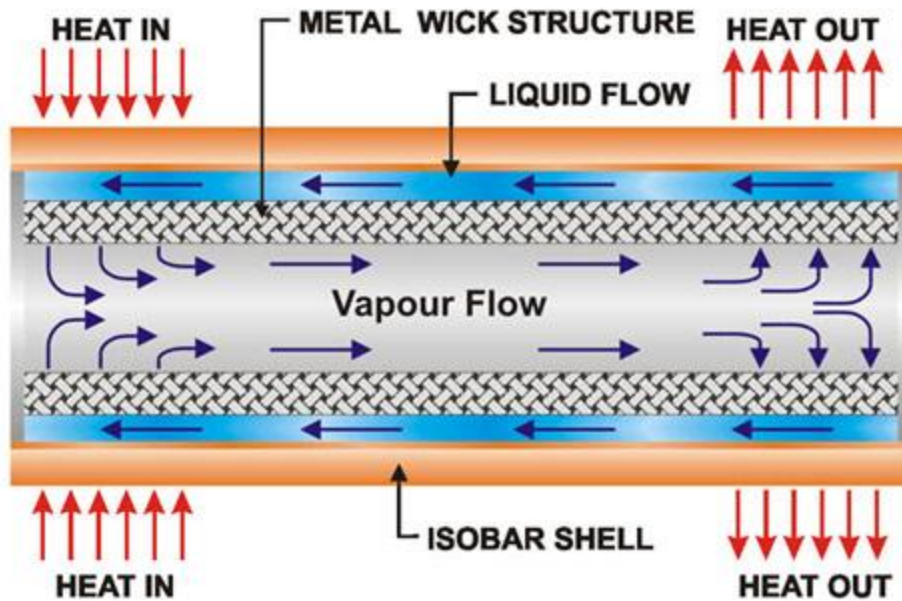


Figure 1.1. Schematic of a conventional heat pipe.

Years later the invention of the personal computer has made conventional heat pipes readily available everywhere due to its low cost and its high effective thermal conductivity relative to any known common material such as diamond, silver, or copper. For example, copper has a thermal conductivity value of 400 W/mK, but a typical heat pipe can easily achieve an effective thermal conductivity higher than 10,000 W/mK.

The conventional heat pipe is a heat transfer device that effectively utilizes evaporation and condensation to transfer heat for a long distance. A heat pipe consists of a container charged with a working fluid. This sealed container is divided into three sections: 1) the evaporator where heat is added, 2) the adiabatic section where no heat transfer exists, and 3) the condenser where heat is rejected. In a typical conventional heat pipe, the container has a

cylindrical pipe-like shape. One pure working fluid exists in this sealed pipe. When heat is added onto the evaporator section, the heat is transferred through the container wall and reaches the working fluid inside. When the temperature achieves the saturation temperature corresponding to the local saturation pressure and is higher than required superheat, the working fluid vaporizes, and vapor generates in the evaporator section. In the condenser section, the temperature is lower than the evaporator section. The saturation pressure corresponding to the condensation temperature in the condenser is lower than the saturation pressure in the evaporator. The pressure difference caused by the temperature difference between the evaporator and condenser makes vapor flow from the evaporator section to the condenser section. The condensate in the condenser is pumped back by the capillary force. In this way, the heat is transported from the evaporator to the condenser.

As the power density increases, the heat transfer mechanisms existing in CHPs limit the heat transport capability. For example, in a CHP, the capillary limitation is that the capillary pressure generated in the heat pipe cannot be higher than the total pressure drops and there exists a limitation. When heat added on the evaporator section in a CHP is higher than this limitation, the heat pipe dries out and reaches the capillary limitation. In addition, the boiling limitation is another factor limiting the heat transport capability in a CHP.

1.3 OSCILLATING HEAT PIPES

In the past, the electronics have been low enough in power that conventional heat pipes can provide the necessary heat transfer to meet the needs of the industry. However as the electronics industry has continually miniaturize and increase in process power, conventional heat pipes have started to hit its limits. One promising technology that has been in development for the past two decades is the oscillating heat pipe (OHP). Akachi was the first to develop this device which can be seen from his 1990 [4] and 1993 [5] patents. Over the last two decades, extensive investigations on OHPs have been investigated resulting in a big increase in research articles investigating oscillating heat pipes.

The heat added in the evaporating section produces vaporization causing vapor volume expansion, and the heat removed on the condensation section generates vapor condensation causing vapor volume contraction. The expansion and contraction of vapor volume produces the oscillating motion of liquid plugs and vapor bubbles in the system. In addition to the oscillating motion in the system, the pulsating motions of liquid plugs and vapor bubbles co-exist at the same time. For this reason, the OHP is sometimes called a pulsating heat pipe (PHP). The phase change heat transfer in the evaporator and the condenser are the primary driving forces for the oscillating/pulsating motion in the system. The thermally excited oscillating/pulsating motion is the primary means used to transport heat from the evaporator to the condenser. The oscillating/pulsating motions in the OHP depends on the surface conditions, dimensions, working fluid, operating temperature, heat flux and total heat load, orientation, number of meandering turns, and, most importantly, the filling ratio.

The OHP typically is made up of a long meandering channel embedded inside the device. These channels will look similar to the schematics shown in Figure 1.2. Working fluid will then be charged or filled into the previously voided channels. A certain ratio of liquid to vapor ratio will be set from this charging step. Once charged and sealed, there will be a train of vapor bubbles and liquid slugs of working fluid throughout the system. The basic geometric shape of the OHP can come in two main forms, tubular oscillating heat pipe (T-OHP) and flat plate oscillating heat pipe (FP-OHP) as seen in Figure 1.2. The T-OHP can be made from any impermeable tube but it is typically made from readily available copper tubing. The FP-OHPs are typically copper or aluminum flat plates that have grooves machined to form the channels.

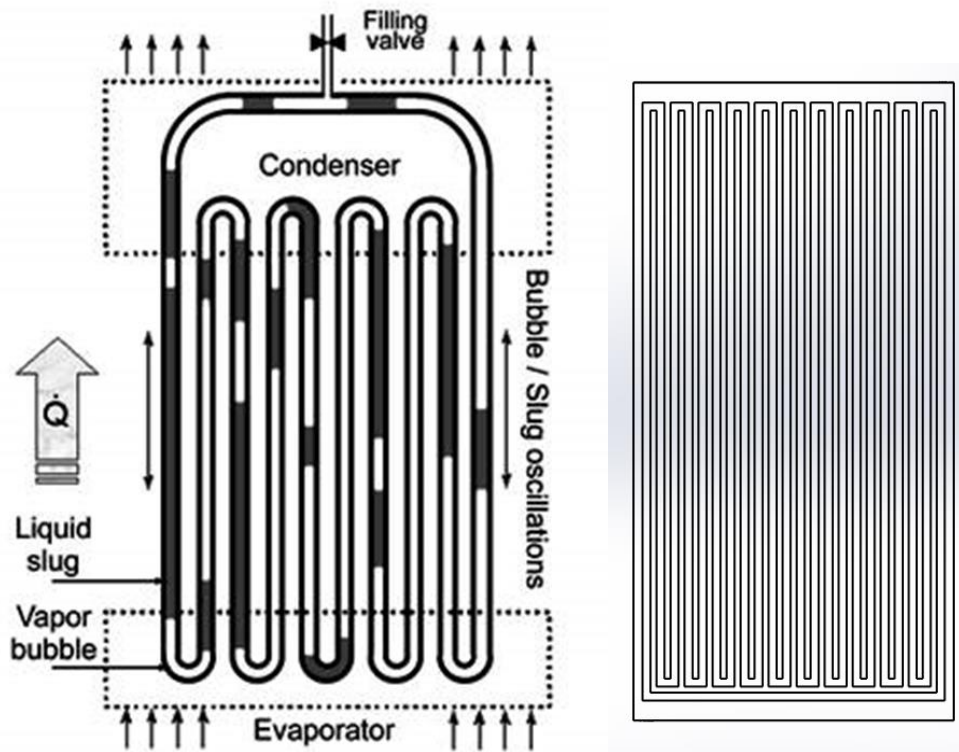


Figure 1.2. Schematic of tubular OHP (left) and flat plate OHP (right)

1.3.1 Features of an OHP

There are five favorable features that the OHPs have over the CHPs: (1) OHPs convert some of thermal energy added on the evaporator section directly to kinetic energy to move the liquid slugs to create sustained oscillations. (2) Concurrent flow occurs due to the liquid and vapor forming along the same direction which is more advantageous than the countercurrent setup that CHPs have. (3) Thin film evaporation plays an important role to cause significant thermal enhancement due to the fluid slugs leaving thin films as they are oscillating. (4) As the movement of fluid oscillating between the evaporator and condenser, force convection is enhanced in addition to phase change heat transfer therefore improving heat transfer performance. (5) Typically as power increases, the thermal performance increases due to more oscillations and thin film evaporation.

1.4 REVIEW OF THE WETTABILITY OF THE OHP

The initial interest in the wettability effect starts with the investigations into the nanofluid effect on the thermal performance of the OHP with different nanoparticle additives such as silver[6], diamond [7, 8], alumina[9, 10] and silica[10]. The nanofluid research has shown improvement in thermal performance in the OHP which led to Qu et al. [9] cutting a section of an experimentally investigated nanofluid OHP and performing scanning electron microscopy to view the microstructures in the internal channels of the OHP. Figure 1.3 shows that the nanofluid in the OHP will deposit onto the surface with most of the deposition in the evaporator.

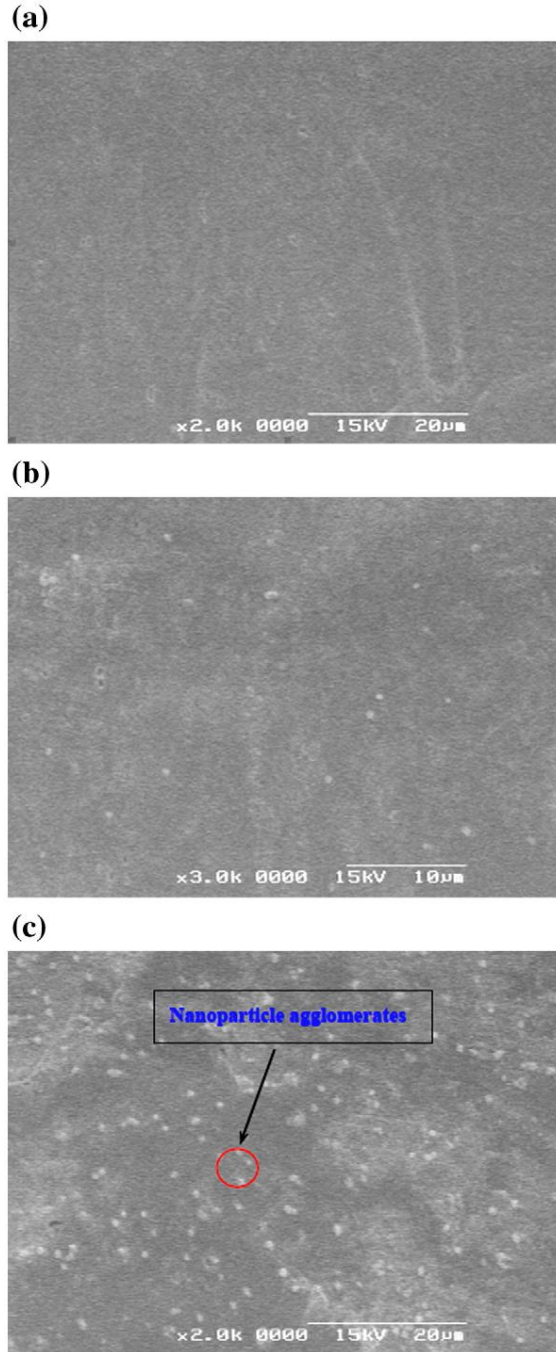


Figure 1.3. SEM images from Qu et al.[9] (a) clean substrate boiled in pure water, (b) a nanoparticle deposited substrate at the condenser, and (c) a nanoparticle-deposited substrate at the evaporator.

The agglomeration of the nanoparticle shows that there could be possible benefits in directly manipulating the internal channels of the OHP. Ji et al. [11, 12] investigated the wettability effect in a T-OHP with full hydrophobic [12] and full hydrophilic [11] experiments. The investigation into the hydrophobic T-OHP showed no improvement of the thermal performance but showed that oscillating still occurs. The hydrophilic T-OHP showed drastic improvement in the thermal performance when compared to a non-treated T-OHP. However no work has been done on a FP-OHP that is partial wettability treatments, hybrid hydrophilic/hydrophobic treatments, and modeling of the wettability effect on the oscillating motion in an OHP.

1.5 RESEARCH OBJECTIVES

As summarized above, the OHP has a potential to efficiently transport heat high power density. The fabrication cost is one of limitations for the wide application. Therefore, the fabrication process is first reviewed and investigated in order to find an innovative fabrication process for a new type of OHPs. Using the summarized fabrication process, a number of OHPs are fabricated. The experimental investigation of the inner surface wettability on the heat transfer performance of an OHP is conducted. The inner surface of OHP evaporator is first treated to determine whether the hydrophilic surface treatment can enhance the heat transfer performance. Then, an experimental investigation of hybrid half hydrophilic/half hydrophobic OHP is conducted to determine their effects on the oscillating amplitude, frequency and heat transfer performance. In order to visualize and better understand the wettability effect on the oscillating motion and frequency, neutron image technology is utilized to study the hydrophobic/hydrophilic surface effect on the oscillating motion. In order to find the mechanism how the wettability affects the oscillating motion and amplitude, a mathematical

model was developed. The model considers the effects of frictional force, driving force, and receding and advancing contact angles with a focus on the contact angle effect on the oscillation frequency and amplitude. In addition, based on previous investigation of Taylor bubble flow in a tube, a theoretical investigation is conducted to predict the operating limitation existing in an OHP.

2 FABRICATION

A detailed description of the techniques used to manufacture an oscillating heat pipe has been fragmented in literature. During the experimental investigation of OHPs, a number of manufacturing methods have been investigated. The most common or well established fabrication techniques will be reviewed first. The later sections novel manufacturing concepts will be addressed.

2.1 TRADITIONAL MACHINING METHODOLOGY

The commonly used fabrication technique for oscillating heat pipes is the use of machining techniques such as manual ball-mill machining, computer controlled cutting (CNC) machining or electric discharge machining (EDM). The machining method allows flat plate OHPs to have great geometrical freedom for applications that need specific geometries especially in confined spaces such as laptops. For example a very small oscillating heat pipe as seen in Figure 2.1 at comparable size to conventional heat pipes found in laptops. In order to fabricate such a small size OHP, EDM was used exclusively for accurate, low stress machining as to not bend the piece due to built-in stresses in the metal. Larger systems such as the 10.16 mm x 10.16 mm OHPs seen in Figure 2.2 and Figure 2.3 can be done with conventional machining involving CNC machining for the complicated curvatures which was done for the OHP in Figure 2.2 or manually which is easier for Figure 2.3 since the relative movement of the ball mill only needs straight lines.

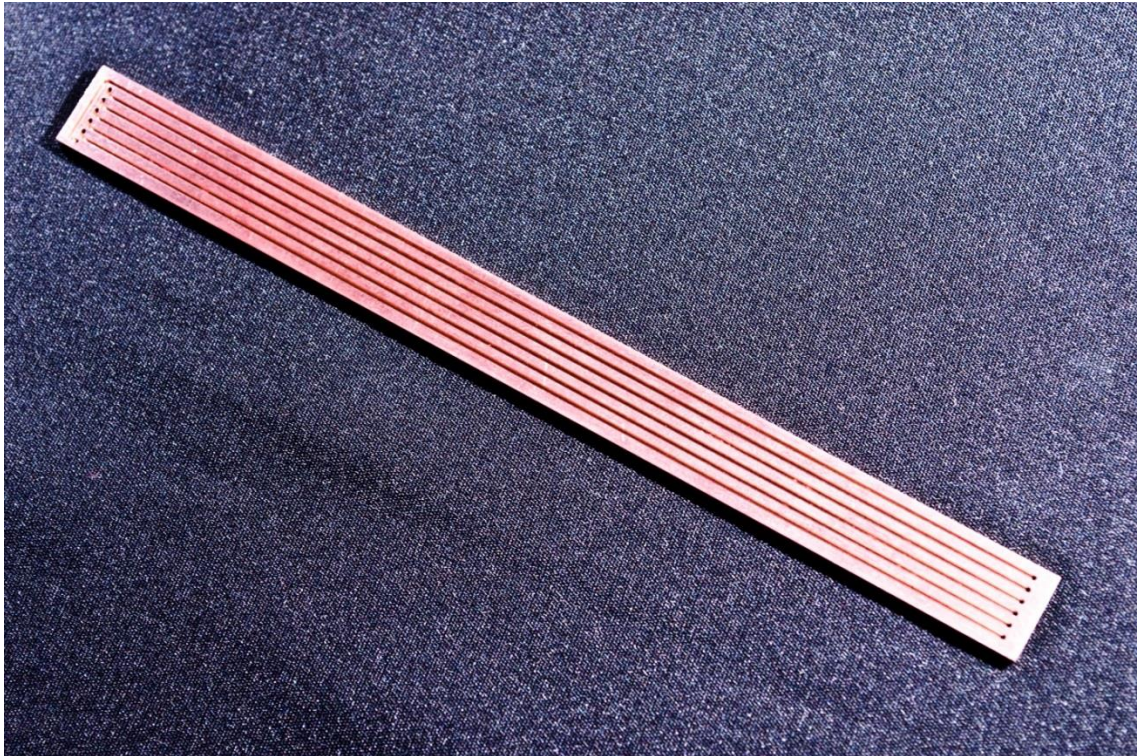


Figure 2.1. Miniature OHP at 12 mm x 100 mm with 0.5 mm square channels.

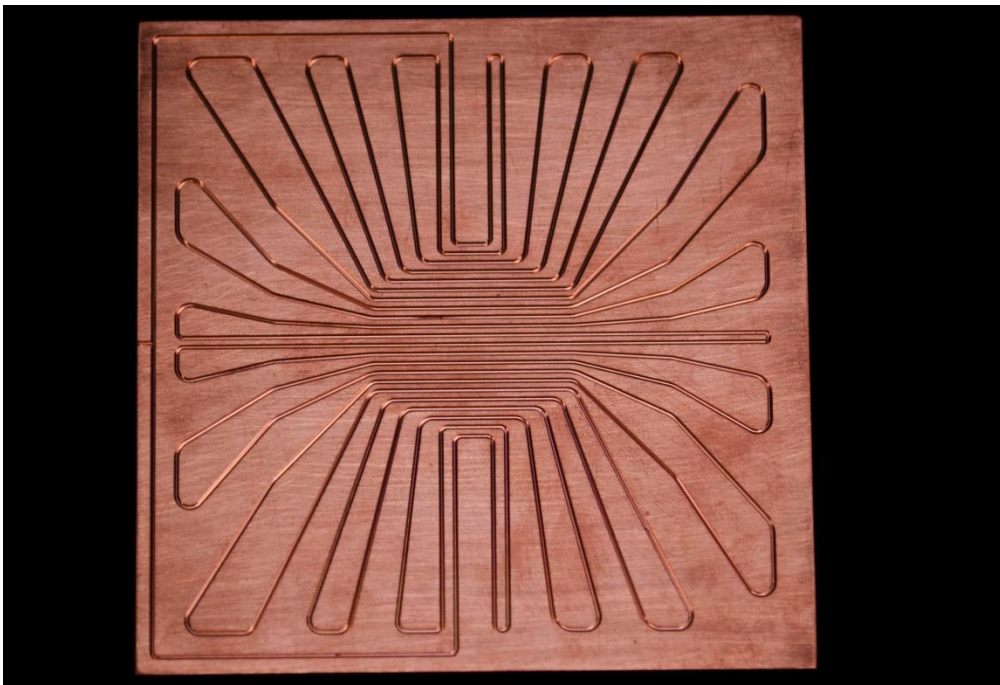


Figure 2.2. Flat Plate OHP with geometry of 10.16 mm x 10.16 mm.

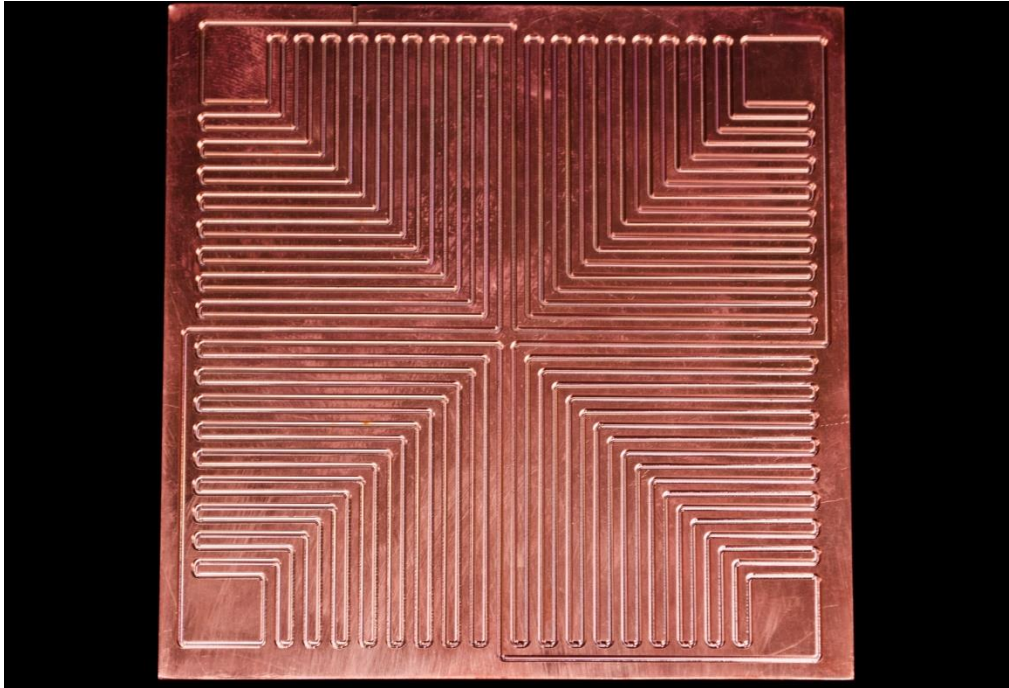


Figure 2.3. A different version of a 10.16 mm x 10.16 mm Flat Plate OHP.

Aluminum 6061-T6 and copper 110 alloys are the preferred choices for this methodology due to the high thermal conductivity and relatively easy to machine. Less common are ceramics due to the exceptionally high level of hardness and brittleness making them unacceptable choices for machining especially once cost and tooling are factored. Plastics tend to be straightforward to process, but with the low thermal conductivity, they tend to not be used very commonly even though the cost is very low. Another issue with plastics is the outgassing of the compounds impregnated internally. Therefore strict selection of low outgassing, non-porous plastics are important. One important design consideration is to make sure that the FP-OHPs must be as flat as possible. A misalignment between the grooved channels and the cover plate will lead to gaps. This makes machined OHPs prone to leaking in the sealing process.

2.2 CERAMIC OHP METHODOLOGY WITH ALUMINUM NITRIDE

Ceramics in general have low CTE and are electrical insulators. Therefore a development of a ceramic OHP becomes important in order to satisfy these two constraints. However, thermal conductivity of ceramics is poor, but with recent manufacturing techniques, engineering ceramics with high thermal conductivity are available.

A review of ceramic literatures [13-17] has been conducted and two major candidates have been chosen for the ceramic OHP. One is beryllium oxide (BeO), and the other is aluminum nitride (AlN). Table 1 shows comparison of these two ceramics with other typical materials. Silicon will be the benchmark in terms of CTE, and copper will be the benchmark for k values. As one may notice AlN and BeO both have adequately high thermal conductivities to copper and have a low enough CTE to match the Si. The Cu and Al both have CTEs that are way too high for use while the Al_2O_3 had too low of thermal conductivity for an effective OHP. Light weight especially in regards to aerospace applications has prompted the comparison of densities. All the materials except for copper have pretty similar light weight densities. The key difference that separates AlN and BeO is the toxicity. MSDS has stated that BeO is extremely toxic by inhalation and ingestion [18]. Therefore with similar CTE, acceptable thermal conductivity, low density and nontoxic, AlN is the material of choice for a ceramic OHP.

Table 2.1. Comparison of ceramic material

Material	k (W/mK)	ρ (g/cm ³)	CTE (10 ⁻⁶ /°C)	Toxic
BeO	370	3.01	5.5	Yes
AlN	320	3.26	4.5	No
Cu	401	8.94	18.3	No
Al	237	2.7	23.1	No
Al ₂ O ₃	18	3.95	8.1	No
Si	149	2.3	2.6	No

In order to create an AlN OHP, a detailed fabrication process of AlN ceramic needs to be determined. The fabrication process of ceramic has been around for generations, and a number of fabrication processes for ceramics have been developed. A typical fabrication process consists of three main steps as follows: powder preparation, shaping process, and sintering process [15-17]. The development of AlN OHP involves the integration of heat pipe and ceramic fabrication technology, which includes powder preparation, shaping process, OHP integration, sintering process, and charging process.

2.2.1 Powder Preparation

When ceramic parts are made, they are typically fabricated from powder first. Additives are added to the powder to enhance special needs that may arise throughout the process. There are three main additives that are relevant to this application, i.e., binders, sintering aids, plasticizers.

Binders give the ceramic powder strength when it is shaped to different geometries or forms. They can range from a number of products such as polymers, starchy materials, etc. To get a clearer picture of the importance of binder, imagine a child building a sand castle on the beach. It is much harder for that child to build a sand castle without the sand being somewhat damp. In this case the sand is the ceramic, and the water is the binder. Binders give strength and structural integrity to the ceramic. For the AlN, polyvinyl butyral (PVB) will be the primary binder [16].

Sintering aids are typically used to improve densification throughout the sintering process. In the sintering process the ceramic will become smaller and denser. Sintering aids will help fill small pockets of vacancies in the structure as the ceramic compacts and fuses together during the sintering process. In the case of AlN, the main purpose of the sintering aid is to improve thermal conductivity of the final piece [19-23].

The main function of plasticizers is to soften the binder and increase the flexibility of the green body or presintered state. Also plasticizers tend to improve the mixing between the additives and ceramic powder keeping everything suspended. The plasticizer of choice will be dibutyl phthalate [16, 24].

The chemical components in percent mass for the ceramic powder are as follows:

- AlN-94% (Ceramic Powder)
- PVB-2% (Binder)
- Y_2O_3 -2% (Sintering Aid)
- Dibutyl Phthalate (DBP)-2% (Plasticizer)

These are the main four materials used throughout the experiments. A solvent used to mix these chemicals is ethanol. When mixed with the ethanol, this creates a slurry (wet mixture).

In order to create a high thermal conductivity, the particle size is important. When the particles are extremely thin, this also enhances material properties of the final ceramic piece [16, 17]. Ball milling is the primary particle size reduction technique used throughout the investigation. These were easy to obtain and simple to operate compared to some of the more expensive laboratory equipment. Ball milling technique involves usually a cylindrical container turning at a constant velocity with grinding media inside along with the ceramic slurry. The container turns, and the grinding media pounds the ceramic particles breaking them into smaller pieces. The size of the final particles is a function of how long it's left in the ball milling process. Typical time throughout the ball milling is 24 hours to ensure fine particle size.

2.2.2 Shaping Processes

When the ceramic powder is properly prepared, different shaping methods can be employed. The two main techniques will be dry pressing and slip casting. These are the two most common industrial techniques used to form ceramics.

Dry pressing is a method as shown in Figure 2.4 where dried prepared ceramic powders are placed into a die and pressure is applied to compact the powder into a shaped piece [15]. This shaped piece is usually known as green body form. The structure is held together by the binder and applied pressure which means the particles are still separate.

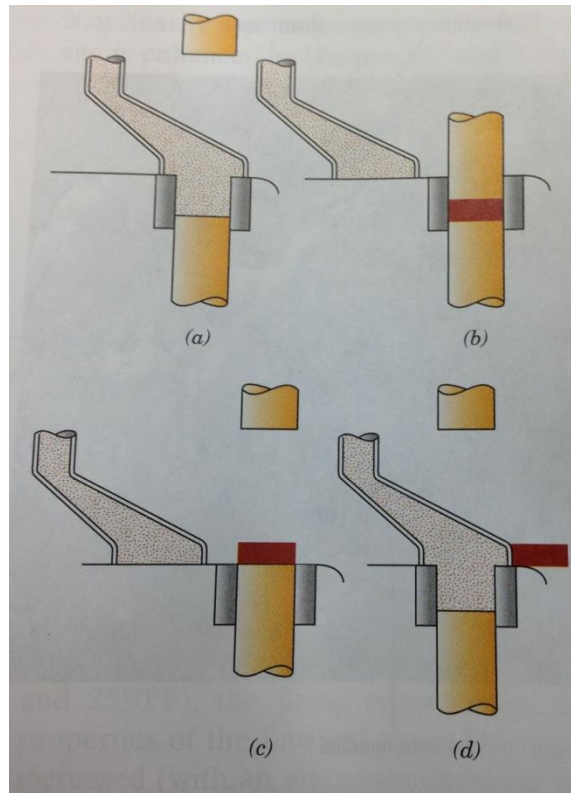


Figure 2.4. Dry press system: (a) powder added to die, (b) pressure applied to compact powder, (c) compacted powder release, (d) process starts again [17].

Slip casting is when a ceramic slurry is poured into a permeable mold such as plaster of paris. The liquid in the slurry is allowed to exit through the permeable mold and the resulting piece that's left is the green body ceramic part. Figure 2.5 gives a better representation of the process.

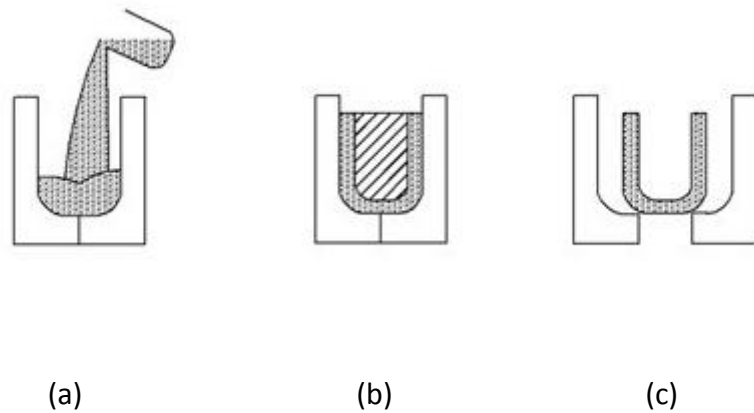


Figure 2.5. Slurry system: (a) initial pouring of slurry into mold; (b) particles build up as liquid is absorbed through the permeable material; and (c) the slip casting surface is separated leaving the cast mold.

To better understand this process, both methods were employed during the investigation using available equipment. The methods were mainly to observe any unique characteristics that AlN in particular had during the shaping process.

Tool hardened steel dies and mechanical presses were utilized for the dry press method as seen in Figure 2.6, and acrylic plastic molds placed on top of plaster of paris were used for the slip cast method as seen in Figure 2.7. Figure 2.8 and Figure 2.9 show the results from these two methods, respectively. Both processes prove successful in forming the desired structures.

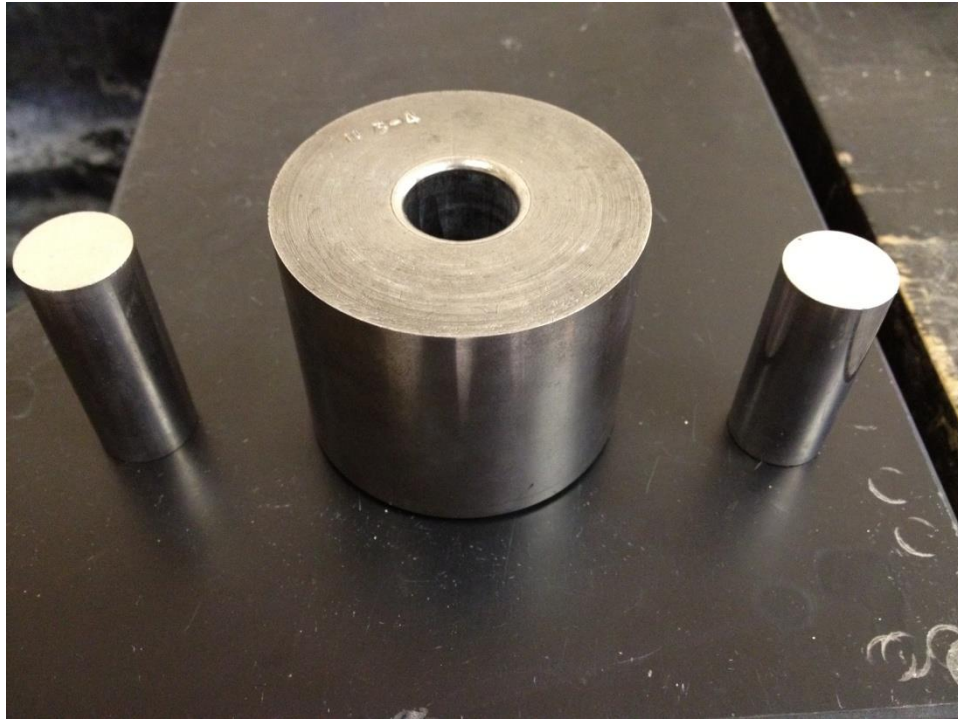


Figure 2.6. Tool hardened steel dies.

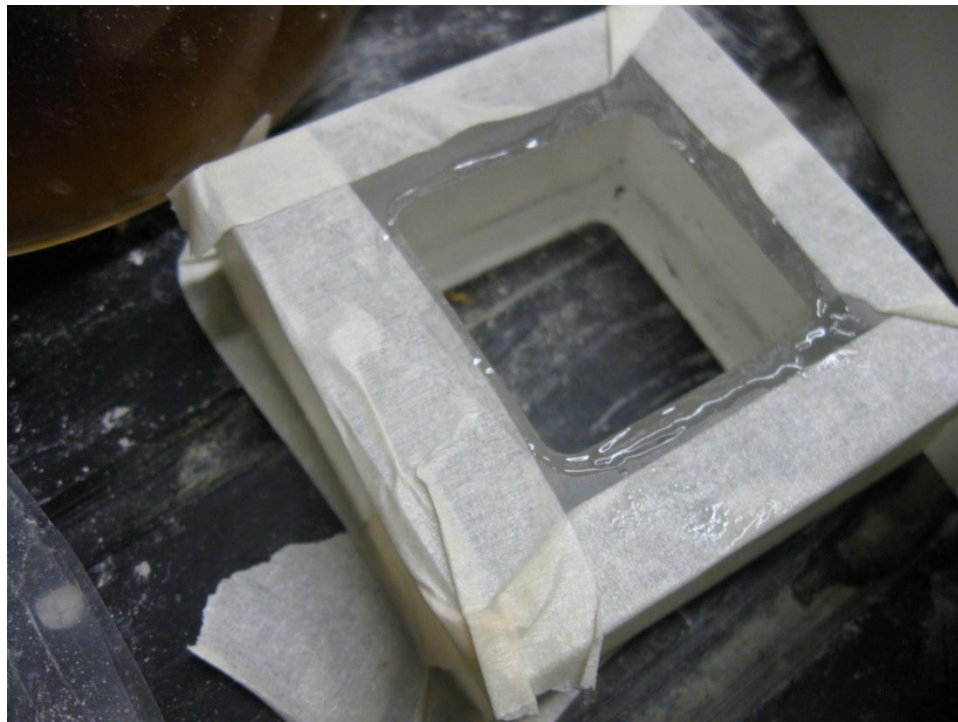


Figure 2.7. Acrylic mold greased with silicone.



Figure 2.8. Dry pressed AlN piece



Figure 2.9. Slip casted AlN piece.

To take the dry press method one step further, machining was introduced to see the machinability of green body AlN pieces. To compare to other previous OHPs, a square geometry was desirable. Figure 2.10 shows the effect on machining on a dry pressed AlN. A small piece of gypsum was added to also see if internal may cause any problems during machining. In the literature, green body ceramic bodies can be machined carefully [15-17]. This observation confirms that claim. The slip cast method was never machined due to the incredibly fragile structure compared to dry press.



Figure 2.10. Machined green body AlN with impregnated gypsum.

2.2.3 OHP Integration into AlN

Throughout this experimental investigation, the most challenging part has to integrate OHP channels inside the ceramic part. A tough material that can withstand high pressures without breaking is highly desirable. Other constraints involved low cost, ease of manufacturability, and burnout capabilities during sintering. The idea is to place a channel piece inside the slip casted or dry pressed AlN and later burn the positive part out leaving a channel cavity inside the AlN part.

Table 2.2. Material selection matrix.

Material	Cost	Burning	Structural Integrity	Manufacturability	Hazard	Useable Time	Total
Ice	10	8	3	1	10	1	33
Salt	10	5	8	1	10	10	44
Gypsen	8	4	6	5	10	10	43
Naphthalene	5	10	3	1	3	7	29
Plastic LSM	8	8	7	9	8	10	50
Higher Number is Better							

Six different materials were chosen to determine their capabilities in creating the necessary OHP channel as seen on Table 2.2. Along with the materials six main parameters were selected to better assess the material decision. Low cost is always a factor in any engineering/research project. Burning means how well these materials can vaporize during the sintering process. Structural integrity indicates how well the system can reliably stay intact especially during dry pressed processes. Manufacturability is the ease at which the desired shapes can be made. Hazard is the overall safety of the material. Useable time is how long the material will last before deteriorating. With these materials and parameters, the plastic from the laser sintering machine is the most desirable.

Through the use of the laser sintering rapid prototyping technology available, different OHP cavity designs can easily be made as seen in Figure 2.11 and Figure 2.12. Also slip cast molds can be made from these techniques also as seen in Figure 2.13.

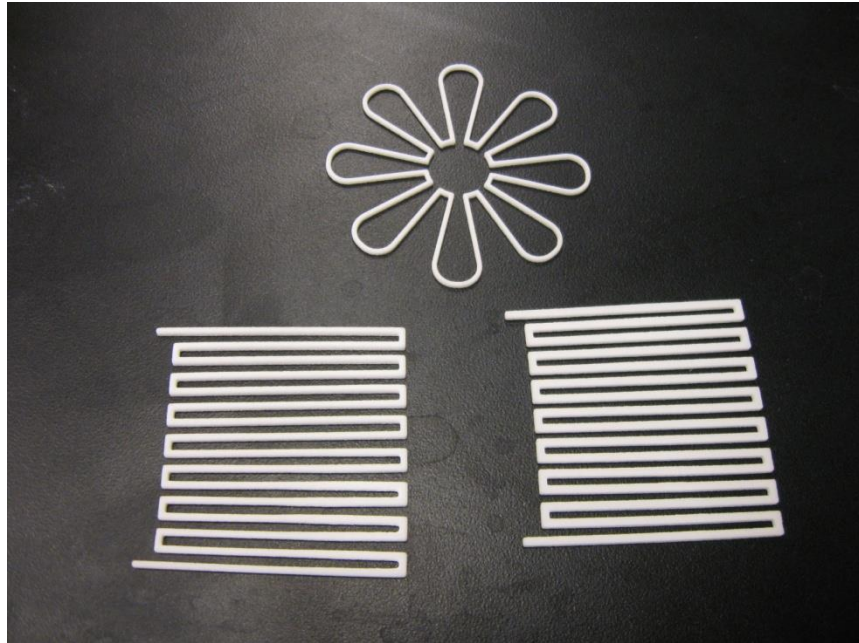


Figure 2.11. First concept OHP cavity designs.

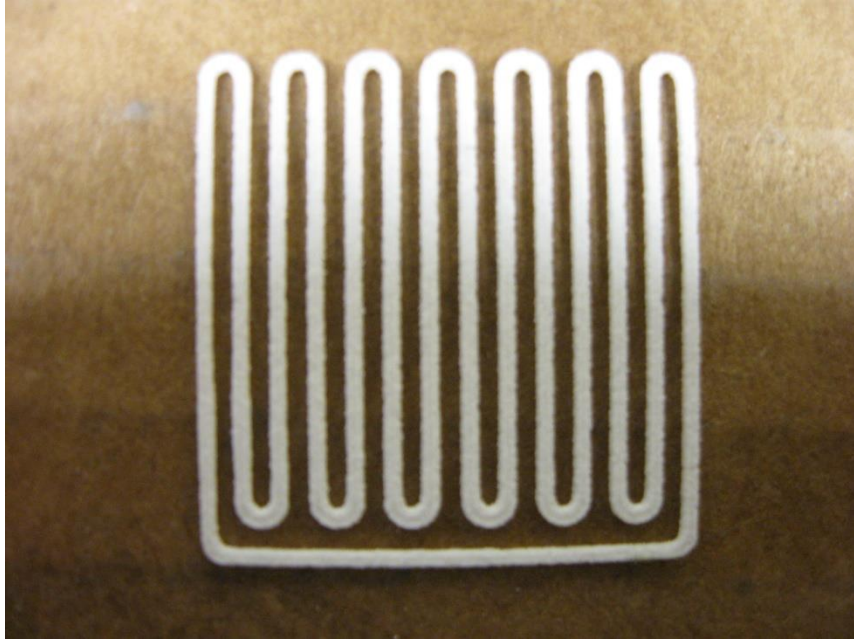


Figure 2.12. Smaller OHP cavity designs at 1 in x 1 in.

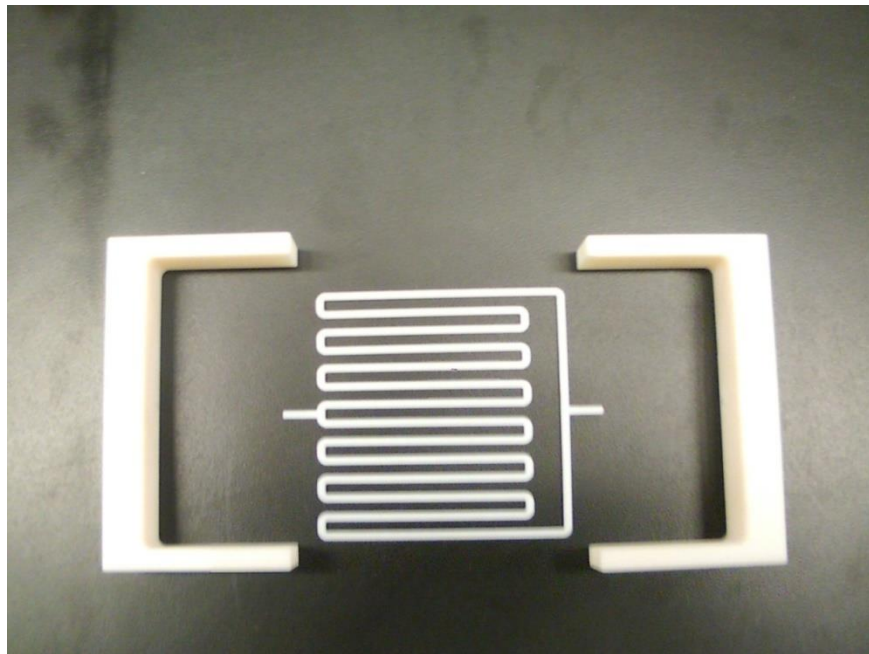


Figure 2.13. OHP cavity with plastic mold.

Next, integration of the OHP cavities along with the two ceramic processing methods was employed. First the slip casting method is employed with the impregnated OHP system as seen in Figure 2.14. A big issue became apparent during the fabrication. One is the crack development that occurs especially through the slip cast method. An important observation for the slip cast method is that as the time increases and the AlN dries, more cracks formed as seen from Figure 2.15 and Figure 2.16. However a promising non-cracked cavity burnout was successfully manufactured for the dry pressed method as seen in Figure 2.17.

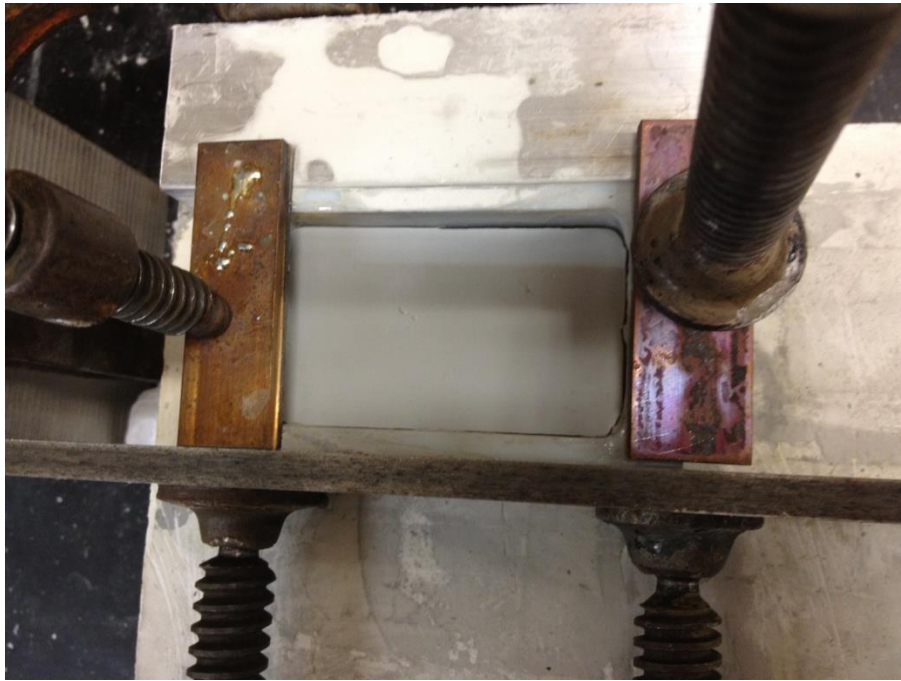


Figure 2.14. Slip casted AlN with impregnated OHP cavity.



Figure 2.15. Crack development minutes after removal from mold.



Figure 2.16. Major crack development after one day.

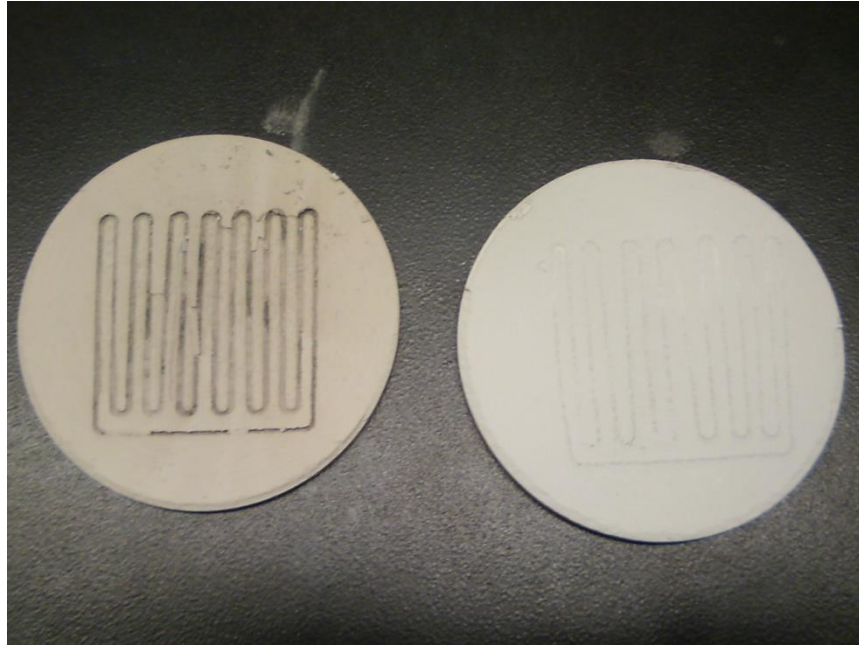


Figure 2.17. Dry pressed OHP integration: (left) burnout of plastic OHP cavity, (right) original green body with OHP cavity.

2.2.4 Sintering

In order to form a high thermal conductivity AlN sample, a sintering process must be employed. Sintering occurs usually at about 80% of the melting point of the material. It is the fusing of powder particles at high temperatures. This reduces the pores present in the structure and increases the density overall [16, 17]. An illustration of this process can be seen in Figure 2.18.

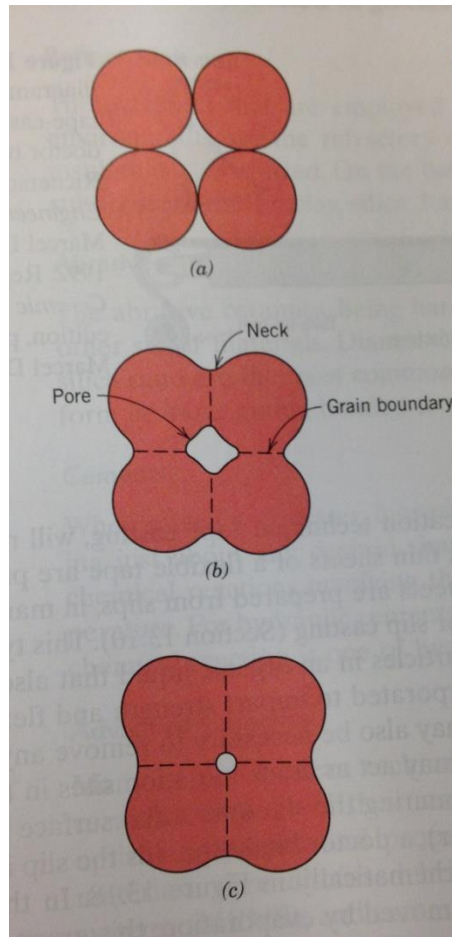


Figure 2.18. Microstructural changes during high temperatures. (a) green body structure, (b) coalescence of particles begin, (c) final sintering structure [17].

For AlN the sintering temperature ranges from 1700-1800°C, and the environment must be in an inert gas such as argon or the native gas of nitrogen [19-25]. During these temperatures, AlN becomes very sensitive to oxygen which could turn the AlN to Al₂O₃ (alumina) which is undesirable in this application. The typical times for sintering can range from 2-24 hrs depending on how dense the sample needs to be. Due to the limitations in the current investigation, a furnace reaching those temperatures cannot be achieved.

2.3 SEALING

One of the largest issues facing OHPs is the method of sealing especially for the flat plate configurations since they need a cover plate. Tubular OHPs only need to be sealed in one or two openings depending on if it's a closed or open looped design. A number of techniques are presents when trying to seal the OHP. Each has their advantages and limitations.

2.3.1 Brazing

The most established method for sealing the cover plate to the OHP is the method of brazing. Brazing is a metal joining process where a filler metal usually in a foil is place between two metal pieces to be joined as seen in Figure. 2.19. All three pieces are then placed in an inert environment usually vacuum or argon atmosphere and taken up to the melting point of the filler material but below the melting point of the joining metals. Once melted the brazing material then will join the parts through capillary action.

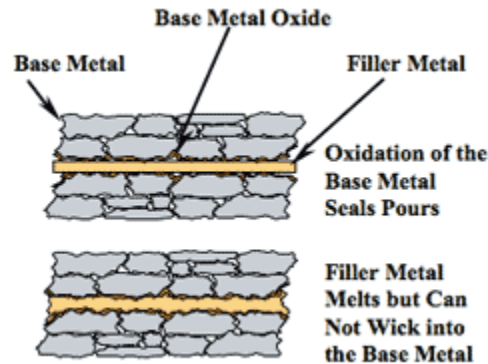


Figure 2.19. Schematic of brazing process.

The brazing process is great for OHPs but it needs to be done carefully. All pieces, the bottom part of the OHP with channels, the cover plate, and the brazing foil need to be soaked in Duraclean (weak acid) to get rid of excess oxide. Then immediately distilled water is needed

to wash excess Duraclean away and acetone is followed to finish up the cleaning. Pressurized is used to speed up the drying process.

Once cleaned the all three pieces must be stacked carefully directly on top making sure no large overhang of foil is showing. The entire stack is then placed in a stainless steel or any high temperature container with a hole on top. This hole will be the access point for the argon or argon + hydrogen mixture from the gas tank to flow through. The flowing of the inert gas will provide the stable environment for the brazing foil flux to react with the plates so no new oxide forms when brazing starts.

At this point all the containers and gas flow are in the oven. The oven temperature is set to 500°C as a quick ramp for 30 minutes then a slower ramp of 2 hours to about 660°C is executed. At 660°C, the OHP is allowed to dwell at that time for 15 minutes. Afterwards oven is allowed to ramp back down indefinitely. Typically once the temperature reaches below 100°C, the oven door can be opened. The temperature ramp setup can be viewed in Figure 2.20.

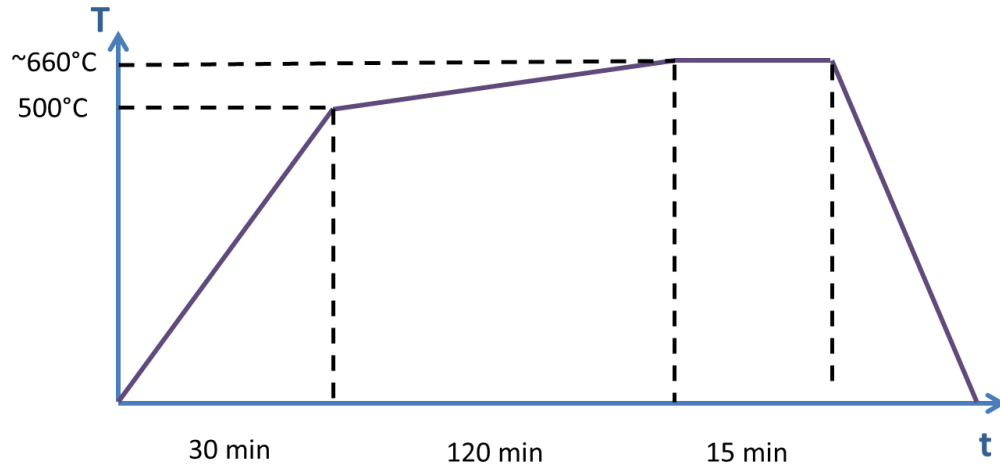


Figure 2.20. Brazing temperature versus time for OHP.

Once brazing is the OHP is submerged in water and air is blown through the charging tube. If air bubbles exits the seams, then leakage has occurred. If no bubbles have formed then the OHP has successfully been sealed from the brazing process and charging can now be done.

2.3.2 Aluminum Brazing

There are certain important parameters to consider when attempting to braze aluminum. Oxygen and water in the atmosphere is very undesirable for vacuum brazing [26]. When there are too much of these contaminants, there simply would not be a brazed aluminum product. When filler metal is used between the aluminum pieces, Miller [27, 28] discovered that the presence of magnesium vapor enhanced the bonding of aluminum.

Later Terrill [29] further refined Miller's observation with the introduction of metal activators in fluxless vacuum brazing. Using activators, the chemical reaction takes place as





Equation (2.1) shows the magnesium reacting with the oxygen in the atmosphere forming a magnesium oxide byproduct as seen in Figure 2.21. The magnesium chips holes corroded around the edges from the oxygen magnesium reaction. This means that the temperature was sufficient for the reaction therefore a successful reaction. Equation (2.2) shows the reaction of magnesium to water which produces a molecule of magnesium oxide along with hydrogen. The other interesting observation which agrees with Miller is in Equation (2.3) the magnesium reacts with the aluminum oxide which is the film that develops across the aluminum surface when open to atmosphere. The byproduct is a magnesium oxide and 2/3 aluminum molecule. Other metals were tested also but magnesium had the highest vacuum pressure of 5×10^{-4} torr which means less vacuum needs to be pulled.

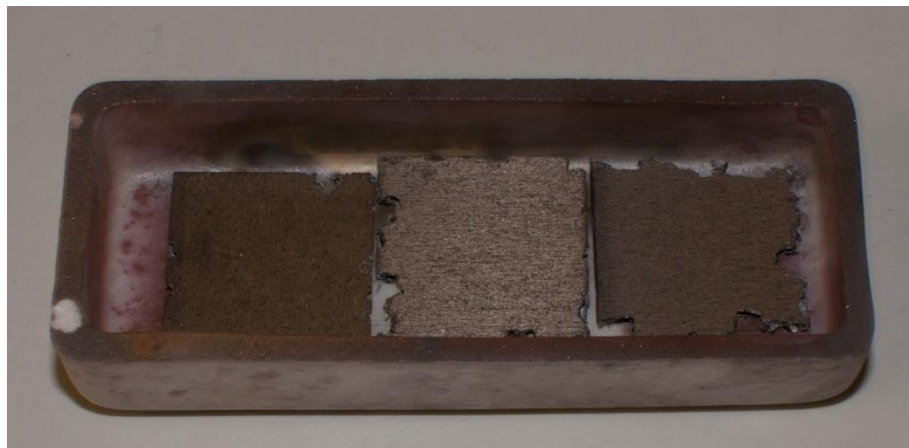


Figure 2.21. Magnesium chips after the brazing process.

Generally brazing temperatures between 582°C to 615°C would be satisfactory. The vacuum needs to be at least 10^{-4} torr to 10^{-6} torr for minimal oxygen and water in the atmosphere. Certain elements in the aluminum filler materials also promotes brazing such as 7.5-12.5% silicon and 1.5-2.5% magnesium tends to have the best results [26].

In Figure 2.22, a rough aluminum piece was taken out of the furnace after the process was completed. In order to better visualize the brazing joint, machining was done for a better view as seen in Figure 2.23. With the successful oxidation of the magnesium chips with the oxygen and hydrogen left in the vacuum as shown in Figure 2.21 and the precise seam developed as shown in Figure 2.23. The aluminum methodology was a success.

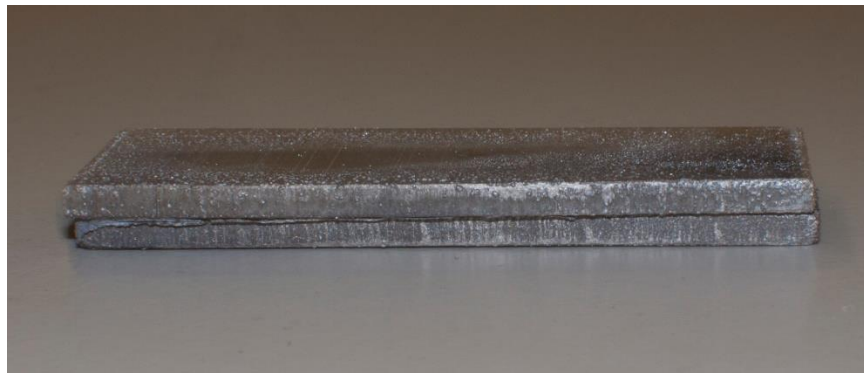


Figure 2.22. Rough aluminum after brazing process.



Figure 2.23. Edge machined to see the brazed attachment.

2.3.3 Mechanical, Adhesive, and Groove (MAG) Technique

The brazing method is not typically suitable for nanostructured oscillating heat pipes due to the destruction caused from the high temperature ranges. A method is used utilizing adhesives for the sealing and mechanical strength from the screws and tongue/groove setup. This method has the advantage of being doable at room temperature. However it does require additional geometrical designs to make this possible.

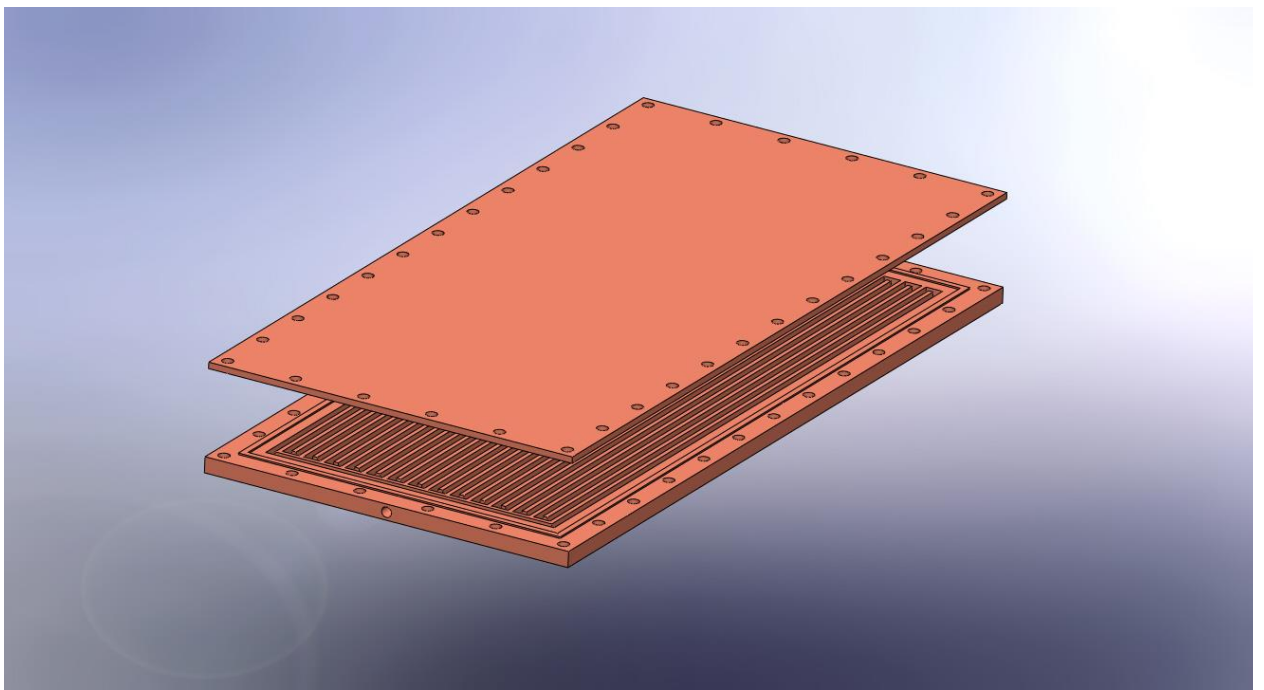


Figure 2.24. Explode version of a flat plate OHP with cover plate.

The overall MAG integrated design of a flat plate OHP is shown in Figure 2.24. First a tongue and groove surrounding the internal channels of the OHP needs to be added as seen in Figure 2.24 and a cross sectional view in Figure 2.25. The OHP has a tongue surrounding the channels and the cover plate has what is called a groove to have a slotted fit as seen in Figure 2.26. With a gap, adhesive can be used to fill this gap as well as sealing the OHP. Additional

views of the tongue can be seen in Figure 2.27 and the groove can be seen in Figure 2.27. The external lip will then have holes for screw and nuts to provide additional mechanical strength. Usually the charging tube can also be sealed from adhesive. The adhesive used for all the experiments is EPO-TEK 301 as seen in Figure 2.28.

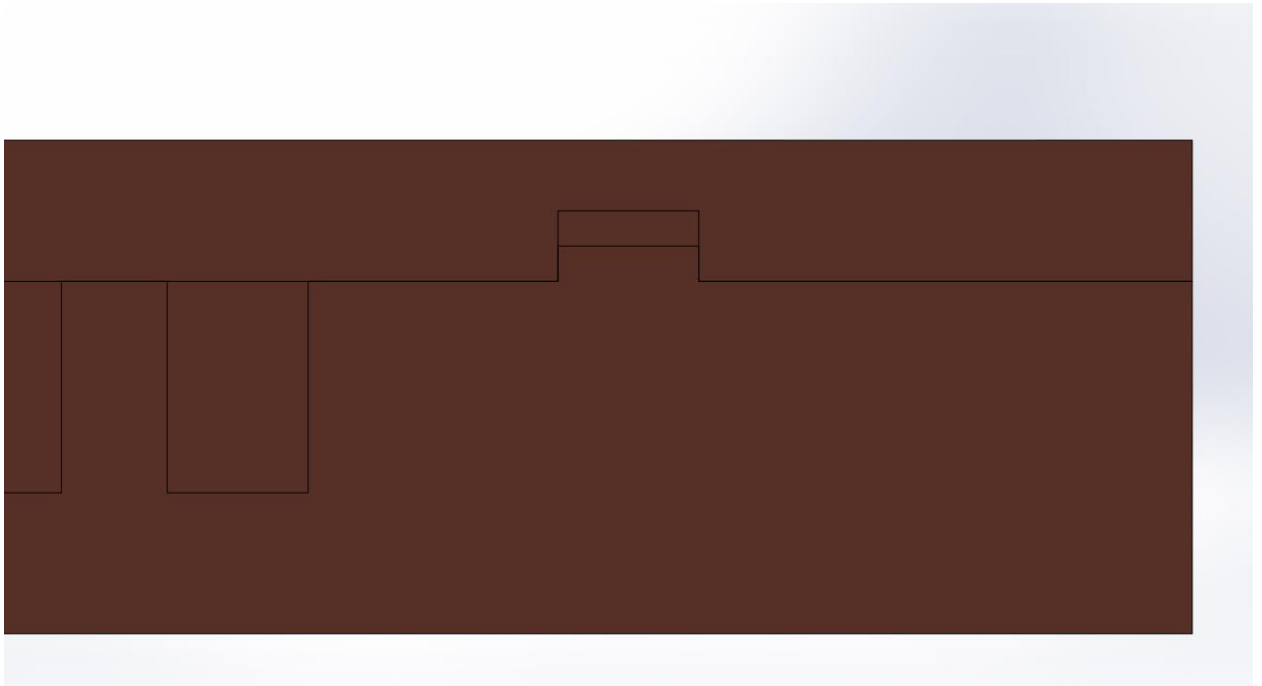


Figure 2.25. Cross sectional view of the tongue and groove.

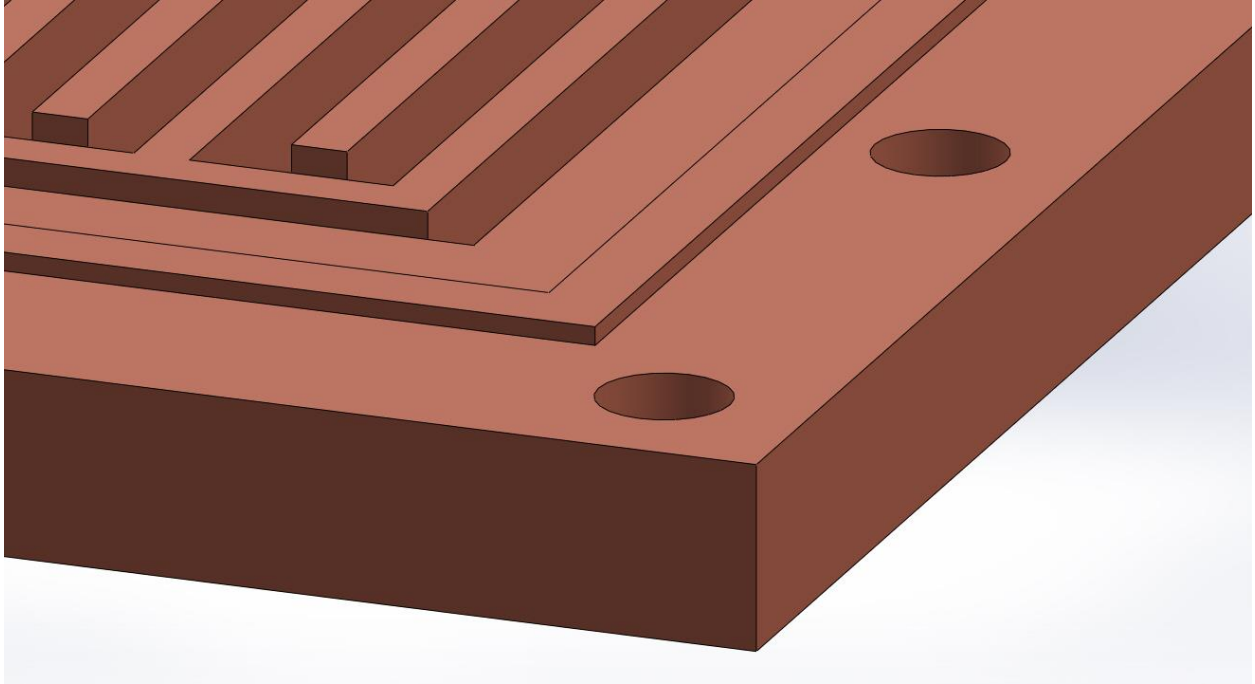


Figure 2.26. View of the OHP tongue.

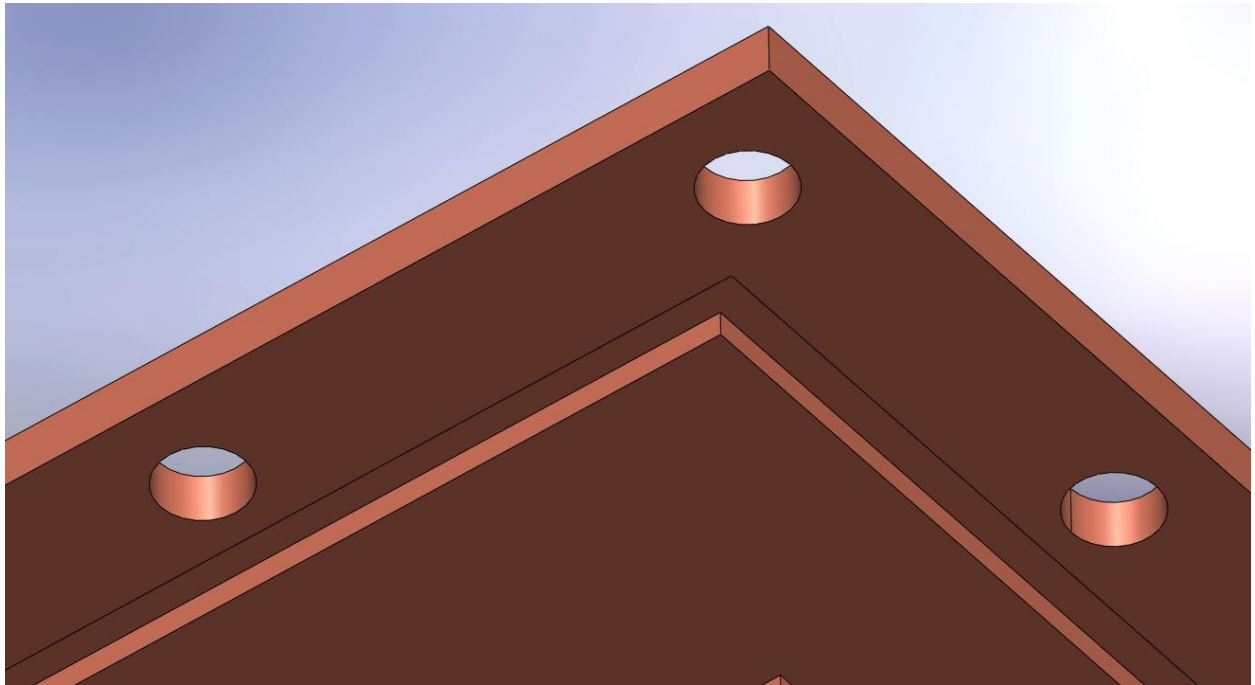


Figure 2.27. View of the cover plate groove.



Figure 2.28. EPOTEK-301 epoxy set.

2.4 CHARGING

Once sealing is done, the final step is correctly charging the oscillating heat pipe which can be accomplished with a system as shown in Figure 2.29. Typically a charging tube is attached to the end of the oscillating heat pipe for fluid insertion. First a three line system as seen in Figure 2.30 is used where one line is for the OHP, another is for the fluid to be added, and the last one is attached to the vacuum line. A rotary vacuum that can go down to at least 10^{-3} torr is needed.



Figure 2.29. Charging system

First the OHP is vacated until down to 10^{-3} torr. Usually this takes about an hour or two. The vacuum line is then closed and the fluid line is opened. Because the OHP is internally under vacuum, the fluid will fill the entire OHP. Once filled, the OHP is allowed to evacuate again and in some instances a hot plate can be used to help move the fluid out faster. The filling and evacuating will happen a couple more times to make sure no air is in the OHP. Once done. The OHP will then be partially vacated with the aid of a scale until the desired charging ratio is met.

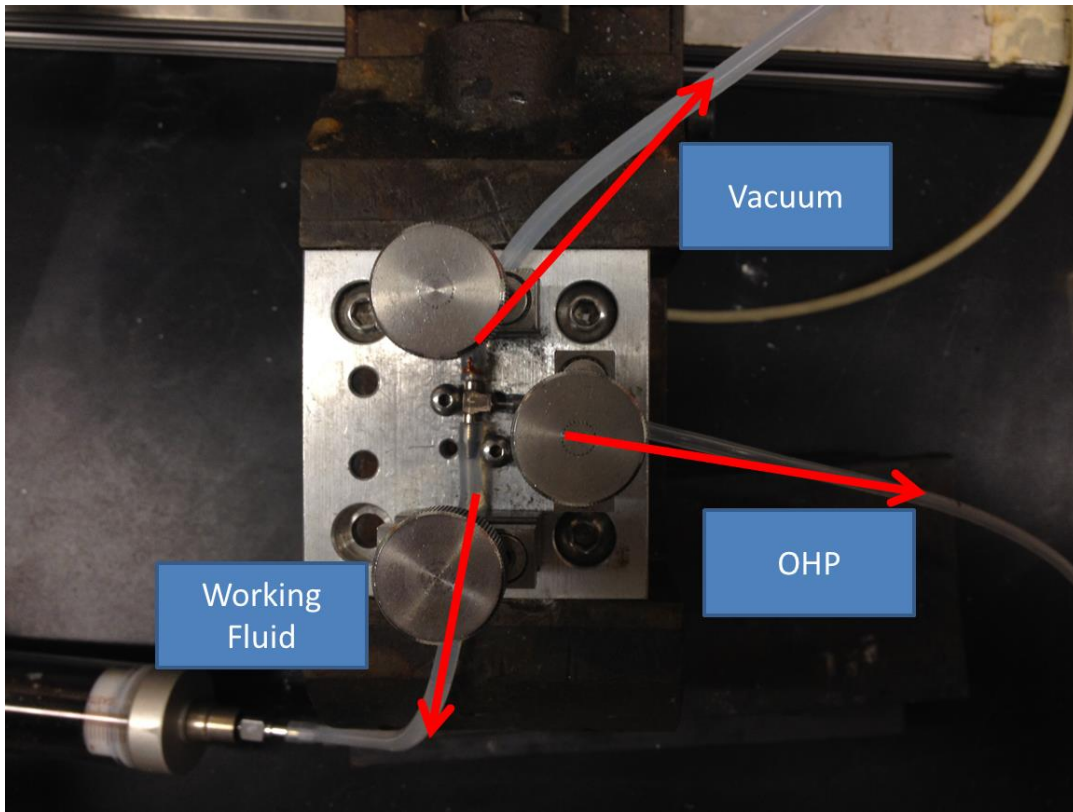


Figure 2.30. Charging ports for vacuum, fluid, and OHP.

2.5 SUMMARY

Manufacturing of the OHP can be done in a multitude of ways. Machining which consist of manual manipulation of the metals, computer controlled cutting (CNC), and electric discharge machining (EDM) will be the most common and readily available form of fabrication especially for metals. Ceramics can be manufactured using the proposed methodologies of slip casting or dry press. Slip casting will need further investigation to a solution that prevents cracking in order to be viable in the future. Dry press method seems to be the most viable for creating a ceramic OHP however further research into the actual sintering portion needs to be performed to check proof of concept.

Sealing methodologies include brazing and the mechanical, adhesive, groove (MAG) methodology. The most common sealing method currently involves the use of brazing foils between the OHP channels and the cover plate. The entire process is placed in a high temperature inert atmosphere to finish the brazing process. The MAG method can be used for low temperature applications where nanostructures are used. This method involves of simultaneous use of screws for mechanical strength, adhesives for further mechanical strength, and a tongue and groove system to keep movement between plates to a minimal.

3 PARTIALLY HYDROPHILIC FP-OHP WITH NEUTRON RADIOGRAPHY

In this study, a hydrophilic treatment of the OHP channel surfaces in selected regions was investigated to study the effect of wetting on the heat transfer performance of a FP-OHP. Three FP-OHP configurations were investigated: 1) only the evaporator section was treated hydrophilically; 2) only the condenser treated; and 3) both untreated. In addition, SEM was used to characterize the surface structures, a sessile drop test was used to measure the contact angle, i.e., determine the wetting condition, and neutron images were recorded to investigate wetting effects on the fluid oscillations.

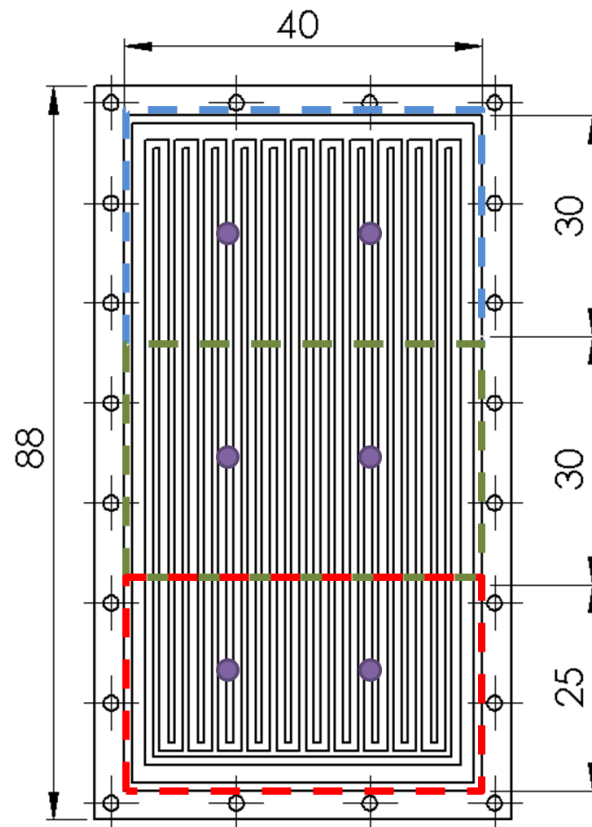


Figure 3.1. Schematic of the FP-OHP investigated (all dimensions in mm). Purple circles indicate thermocouple location. Blue dashed line is the condenser section, green dashed line indicates the adiabatic section and red dashed line indicates the evaporator section.

3.1 EXPERIMENTAL INVESTIGATION

3.1.1 FP-OHP CNC Fabrication

In order to investigate the nanostructured surface effect on the heat transfer performance, a FP-OHP as shown in Figure 3.1 was developed. The FP-OHP design consists of the evaporator, adiabatic section, and condenser with the overall dimensions of FP-OHP being 88 mm x 50 mm x 3.5 mm. The evaporator section has a heated area of 25 mm x 40 mm; the adiabatic has an area of 30 mm x 40 mm; and the condenser section has a cooling area of 30 mm x 40 mm. The internal channels consist of 10 turns with dimensions of 1 mm width x 1.5 mm depth for better neutron imaging contrast. The fabrication process used Cu 110 alloy for its low cost and excellent thermal conductivity. Each FP-OHP, as shown in Figure 3.2, is CNC machined with the exposed groove side lapped to a flatness difference between maximum and minimum height of less than 0.001" for optimal sealing.



Figure 3.2. Fabricated FP-OHP without the cover plate.

3.1.2 Nanostructure Growth

In the chemical treatment process, the hierarchical cupric oxide (CuO) nanostructures were produced on the surfaces using the procedure outlined in Liu *et al.* [30]. The machined FP-OHP and its cover plate were ultrasonically cleaned in 3.0 M HCl aqueous solution for 10 minutes. Ethanol and distilled water were used to remove residual HCl. The nanostructures were prepared by then immersing the copper in a 30 mM NaOH aqueous solution. To confine the nanostructured surface to the selected region, only the evaporator section of the FP-OHP, along with one third of the cover plate, was submerged in the solution. The entire treatment was performed inside a glass beaker that was sealed using Parafilm® and the nanostructured CuO was allowed to grow in an oven at 60 °C for 20 hours. The FP-OHP was then washed with distilled water and allowed to dry before assembling the FP-OHP and cover plate following the sealing method described later.

3.1.3 Characterization

SEM (FEI Quanta) was used to characterize the surface structure as shown in Figure 3.3. The CuO structures are well distributed throughout the FP-OHP as seen in the top image in Figure 3.3. The magnified objects in the bottom image of Figure 3.4 confirm the presence of hierarchical grass-like sheets of CuO reported previously [30]. Each grass-like sheet has what appears to be a sharp tip with additional roughness along the edges. This morphology greatly increases the roughness of the surface and thereby alters its wettability. A conventional sessile-drop technique employing a goniometer setup (VCA 2500 XE) was used to determine the wettability of the structures. In Figure 3.4, the untreated copper (top) has a contact angle of ~60° compared to an extremely hydrophilic CuO surface (bottom) with a contact angle of ~12°.

This result suggests a Wenzel behavior [31] in which contact angle decreases as roughness increases, confirming the effect of the surface nanostructures.

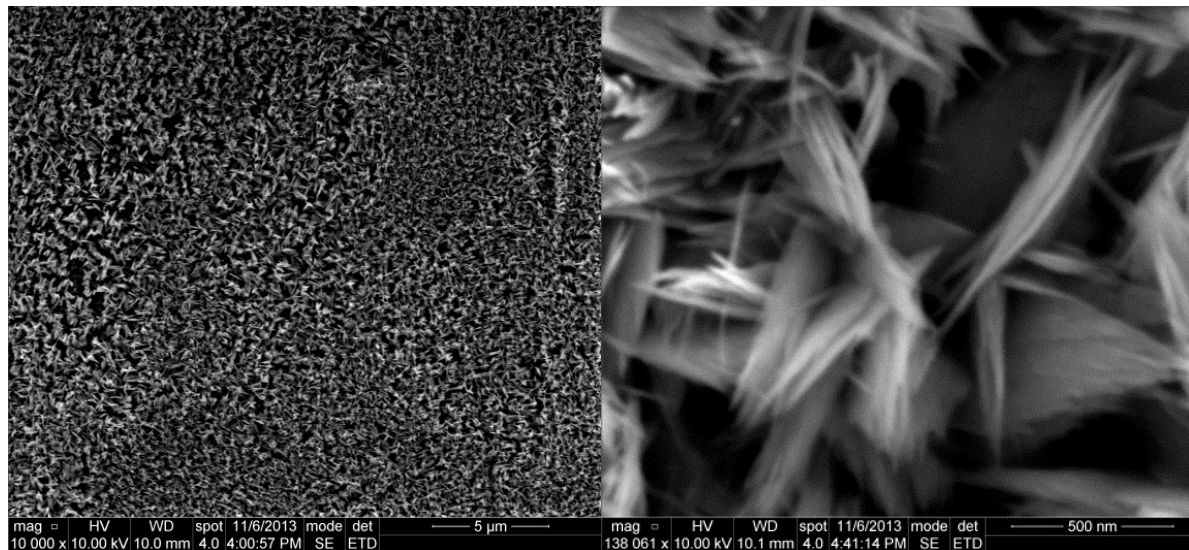


Figure 3.3. SEM images of the CuO nanostructures with magnifications of 10,000X (left) and 138,061X (right).



Figure 3.4. Sessile drop test on nontreated copper at 60 degrees contact angle (left) and treated copper with CuO surface nanostructures (right), showing a hydrophilic contact angle of about 12 degrees.

3.1.4 Assembling and Charging

The use of nanostructures limits sealing of the assembly to low-temperature methods (< 200 °C). The FP-OHP incorporates adhesives, a tongue and groove joint, and a mechanical seal to meet these requirements. Once the nanostructures were grown on the FP-OHP and characterized, the groove surrounding the interior channels (see Figure 3.2) was filled with EPO-TEK-301, a low outgassing epoxy adhesive. The cover plate had a matching tongue partially filling the groove. The holes outside the tongue were used for screws, which applied an additional mechanical force to join the plates. Afterwards, Vacseal® was applied along the exterior seam between the plates to achieve a vacuum tight seal.

After a day of curing, fluid charging can be started. First, the base weight of the system is measured with only air in the channels. Then the newly sealed channels are evacuated using a rotary pump. Once the vacuum is at an acceptable level ($< 10^{-3}$ Torr), the is isolated and high-performance liquid chromatography (HPLC) grade water is then circulated in the FP-OHP system via an additional line. The completely filled FP-OHP is then weighed. At this point, the HPLC line is closed and the vacuum line is opened to pull out 35% of the water resulting in a charging ratio of 65%. The FP-OHP is then reweighed and the charging tube lines are crimped and soldered to prevent any leaking.

3.2 THERMAL TESTING AND NEUTRON IMAGING

Neutron imaging techniques [32, 33] have been utilized to elucidate the fluid motions in OHPs. Neutrons from the reactor are incident on the FP-OHP, which is oriented with its plane perpendicular to the beam. The detector records the neutrons transmitted through the FP-OHP thus forming intensity difference images much like in x-ray radiography. Neutron imaging

experiments were performed at the National Institute of Standards and Technology Center for Neutron Research in Gaithersburg, Maryland using the Neutron Imaging Facility [34] on beam tube 2 (BT-2) with the setup shown in Figure 3.5. The dash-dotted line surrounding the top half of Figure 3.5 delineates the part of the experimental setup inside the shielded cave.

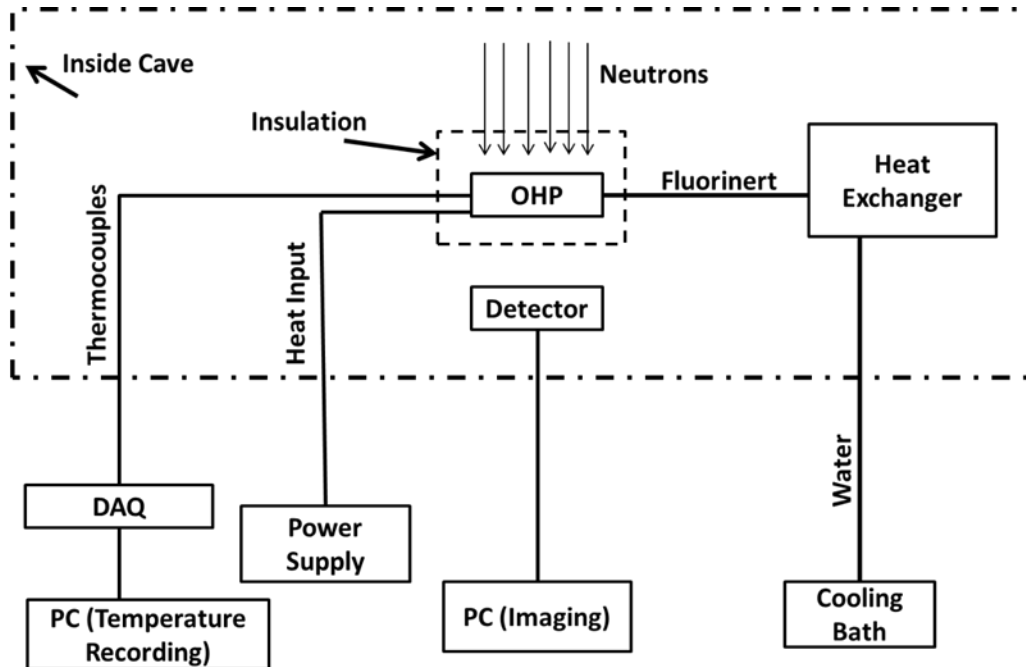


Figure 3.5. Schematic of the entire experimental setup at the NCNR.

The thermal portion of the experimental setup, shown in Figure 3.6, consisted of one 750 W power supply for the resistance heaters in the aluminum heating block attached to the evaporator of the OHP, one custom aluminum cooling block for the condenser, a heat exchanger, one high-capacity cooling bath to remove heat from the heat exchanger, and a data acquisition system (DAQ) to record temperatures. Note that fluorinert (liquid Teflon[®]) was used as the fluid in the cooling block because it did not contain hydrogen thus avoiding interference with the neutron imaging. A total of 6 type-T thermocouples were used to measure the

temperatures in three regions of the FP-OHP, as shown in Figure 3.1. Each pair of thermocouples was placed in the center of evaporating, adiabatic, and condenser sections equidistant along the short side. Temperatures on all thermocouples were recorded at 500 Hz using a National Instruments SCXI-1000 box with SCXI-1303 card for the data acquisition system with SignalExpress software.

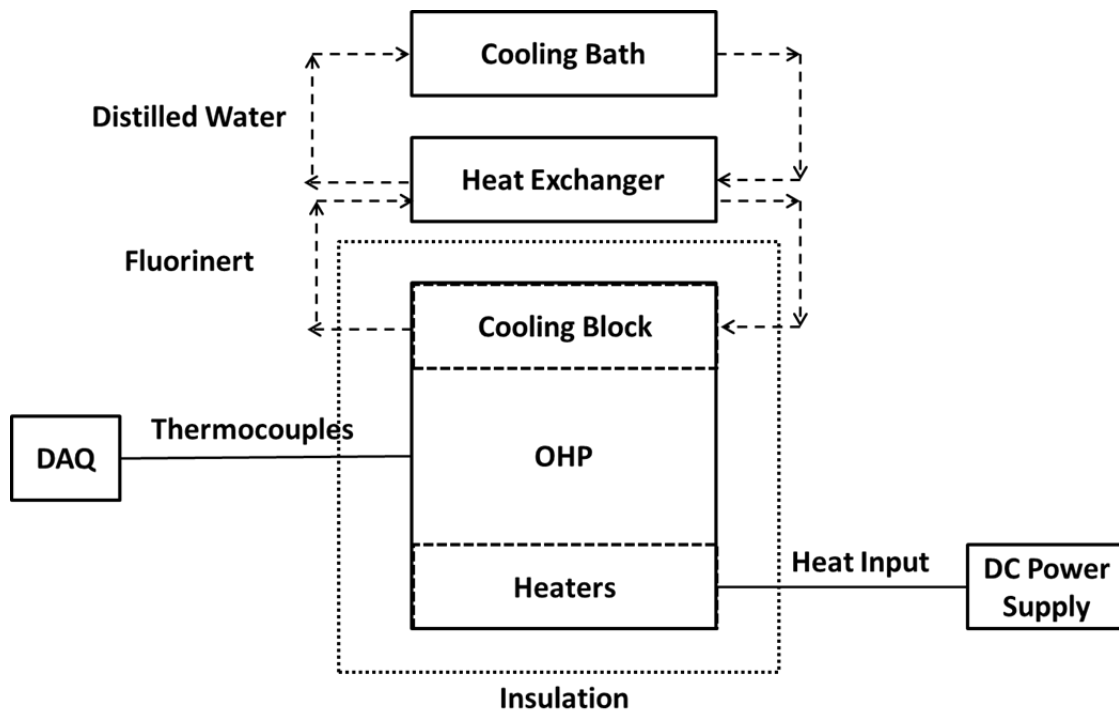


Figure 3.6. Detailed view of the thermal portion of the experimental setup.

The FP-OHPs were set in a vertical orientation for all tests with the condenser on top. Heat was conducted onto the FP-OHPs with a $40 \times 25 \text{ mm}^2$ footprint, while the other end of the FP-OHP was cooled with a flow-through block of area $40 \times 30 \text{ mm}^2$. The heat input was controlled with an Agilent N5750A power supply with a resolution of $\pm 0.01 \text{ W}$. Coolant was circulated through the aluminum cooling block and temperature-controlled to $20 \text{ }^\circ\text{C}$ ($\pm 0.5 \text{ }^\circ\text{C}$) with the cooling bath (Julabo FP40). Four C-clamps held the cooling block and the heating

elements onto the FP-OHP. Thermal paste (Omegatherm “201”) was used between all contact surfaces to reduce thermal resistance. Fiberglass was used to insulate the system from the surrounding environment.

The system was first allowed to reach steady state with no heat input. Then heat input was increased in steps and the FP-OHP allowed reaching a steady state with temperature data collected for 3 minutes at each step. The maximum heat input was 275 W, which is the maximum output of the cartridge heaters. All thermocouple data were read through the DAQ and recorded on the personal computer.

Three tests were conducted, measuring thermal performance over a range of heat input. First, a control FP-OHP with no surface treatments was tested to provide a baseline data set. Second, the FP-OHP with the CuO nanostructures was tested with the CuO in the evaporator; and third, the FP-OHP was flipped and the heating and cooling blocks switched so as to place the CuO nanostructures in the condenser.

3.3 RESULTS

Figure 3.7 compares the thermal performance of the FP-OHPs in the three configurations plus a thermal shock test where the power input instantaneously increases from zero to the desired wattage. The temperature difference plotted as seen in Figure 3.8 is the average of the two evaporator thermocouples minus the average of the two condenser thermocouples. A smaller temperature difference implies better thermal performance of the FP-OHP. The untreated FP-OHP shows a nearly linear dependence of the temperature difference on heat input before the fluid inside begins moving, acting like a solid material

transferring heat by conduction. At about 115 W, the fluid begins to move and the FP-OHP deviates significantly from linearity, showing enhanced performance over a solid material. Fluid motion is confirmed at this point by neutron imaging. The two configurations with the nanostructures also exhibit linear behavior at low heat input, but they show fluid motion and accompanying deviation from linearity at lower heat inputs than the untreated FP-OHP. The nanostructured configurations also show a significant drop in temperature difference as the fluid begins moving in contrast to the untreated FP-OHP, which shows more of a plateau in performance upon onset of fluid motion.

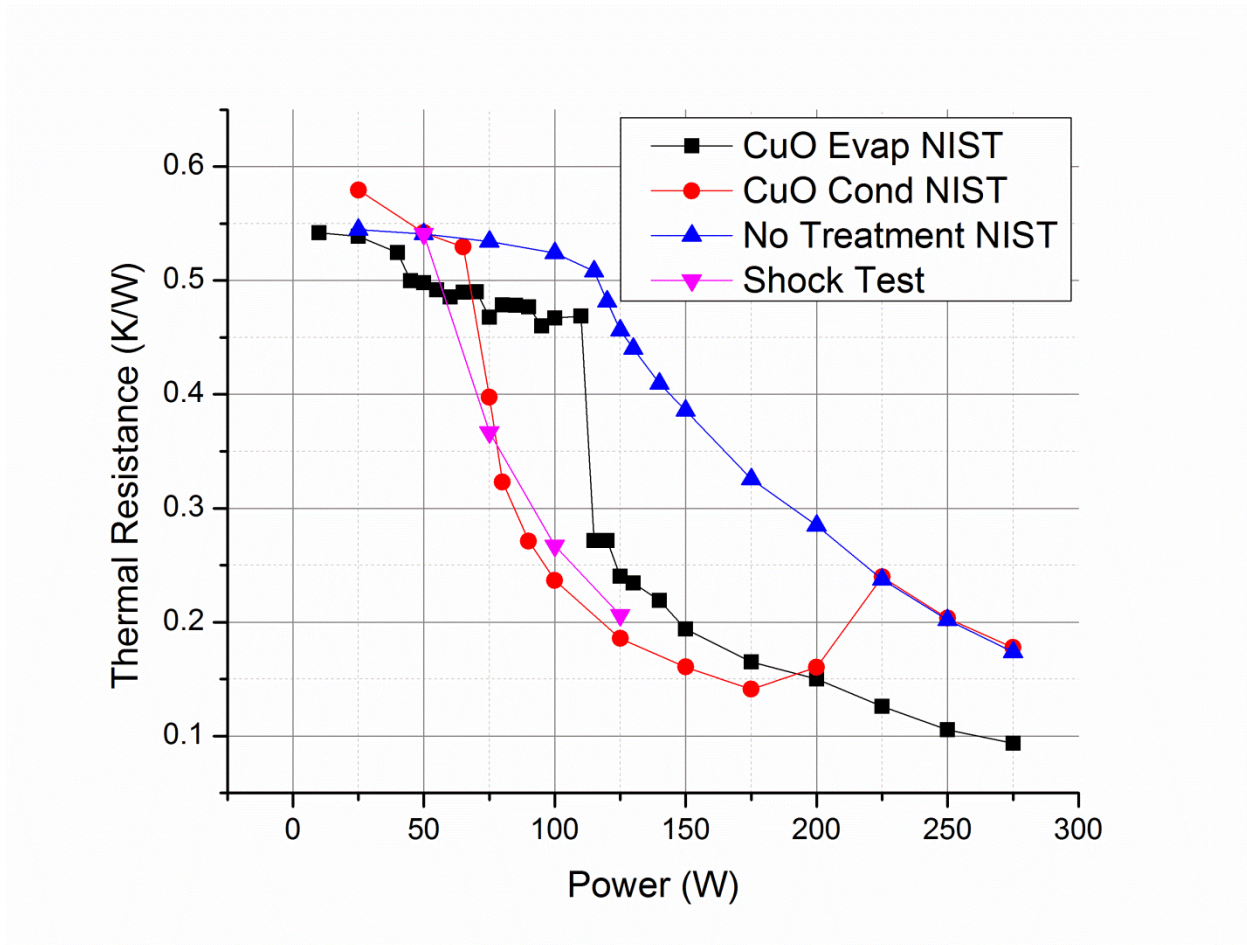


Figure 3.7. Thermal resistance plot with changing input power.

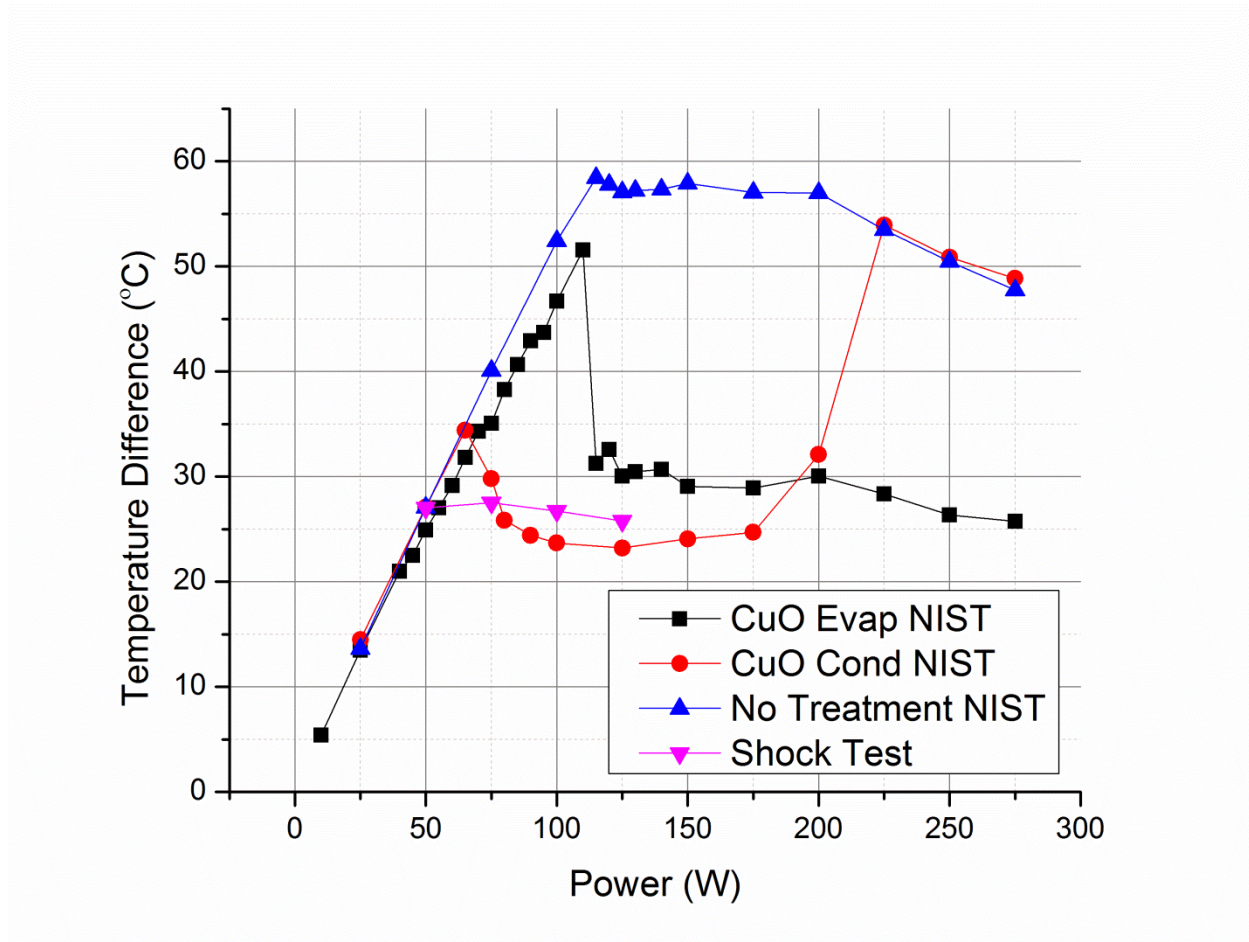


Figure 3.8. Temperature difference as a function of power input.

Placing the nanostructured surfaces in the evaporator or in the condenser produce very different results. With CuO in the evaporator, the performance continually improves, compared to no treatment, up to a heat input of 275 W, which is the cartridge heater limit. The reason is likely the enhanced thin film evaporation from the nanostructured surface in the evaporator as liquid slugs leave behind a thin liquid film after traveling through the evaporator.

In contrast, by placing the CuO nanostructures in the condenser, the start-up of the fluid motion began at a lower heat input of 75 W, compared to the onset at 115 W without treatment or when the CuO was in the evaporator. Also, the configuration with the

nanostructures in the condenser shows the best performance of the three over the heat input range of about 75-175 W. At 175 W, the performance of the condenser nanostructures configuration deteriorates sharply until it matches the performance of the control FP-OHP at 225 W. At 125 W, the maximum contrast between the temperature difference in the control and in a treated OHP was seen, 57.0 °C and 23.2 °C, respectively, about a 60% improvement in performance.

The neutron imaging gives some insight into these behaviors. Figure 3.9 and Figure 3.10 show the distribution of the liquid and vapor phases of the working fluid for the condenser nanostructures configuration at selected times during operation after achieving steady-state conditions at 75 and 225 W heat input respectively. Figure 3.11 and Figure 3.12 show the steady state conditions at 115 W and 225 W heat input, respectively, for the evaporator nanostructures configuration. For both the condenser configuration at 75 W and evaporator configuration at 115 W, the fluid motion is rapid and the liquid is distributed throughout the FP-OHP as can be seen in Figure 3.9 and Figure 3.11. There is vapor in contact with the hydrophilic nanostructured surface in the condenser configuration, which can enhance condensation thereby increasing the latent heat transfer and pressure differences driving the fluid motion. At 225 W for the condenser configuration in Figure 3.10, the fluid still moves rapidly; but the range of motion of individual liquid slugs is lower, and the liquid largely remains in the condenser. However for the evaporator configuration in Figure 3.12, at 225 W the liquid and vapor are both still well distributed similar to Figure 3.10 and Figure 3.11. The nanostructures in the condenser configuration remain covered with liquid and cannot contribute to enhanced condensation of the vapor phase at higher heat inputs. This results in the performance of the

condenser nanostructures configuration matching the no treatment FP-OHP performance at higher heat input. When the nanostructures are covered with liquid in the condenser, the FP-OHP performs the same as when the nanostructures are absent. In contrast, for the evaporator configuration with the larger liquid slug movements and wider distribution of the liquid phase, the nanostructures remain in contact with both the liquid and vapor phases throughout the heat input range studied and its performance exceeds the nontreated and condenser-treated FP-OHPs at the higher heat inputs.

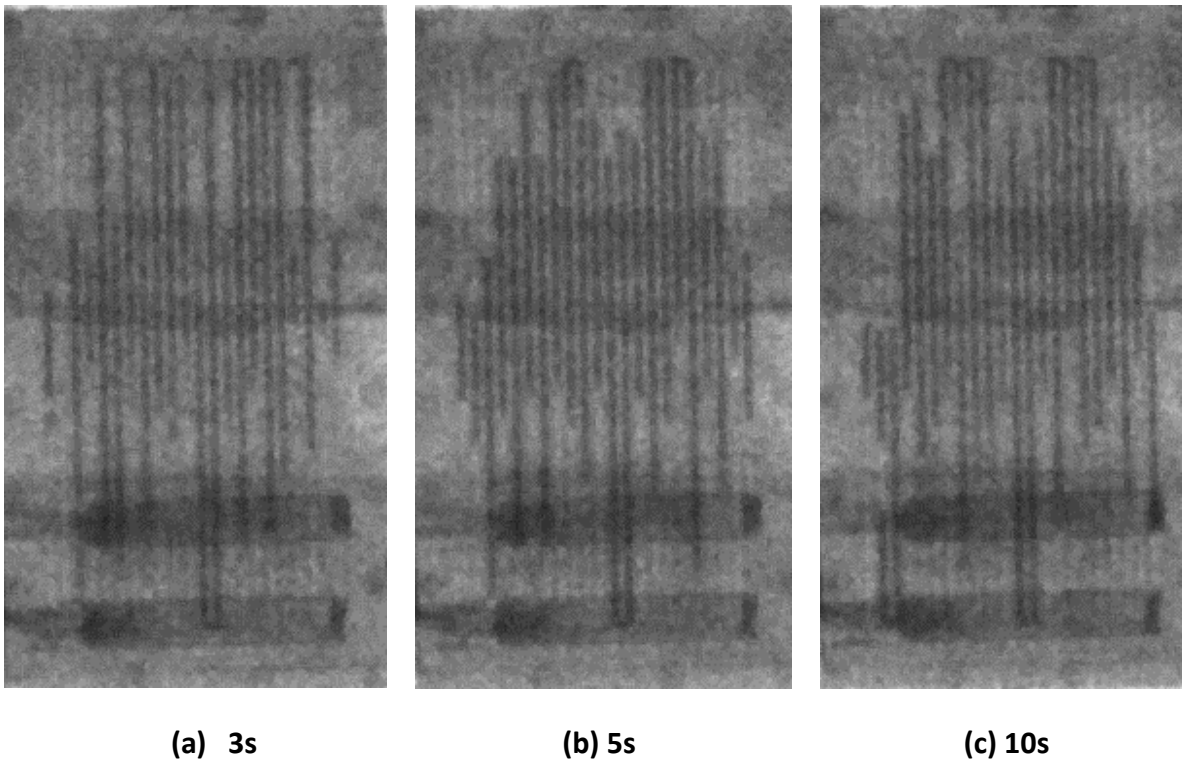


Figure 3.9. Liquid and vapor distribution in the condenser nanostructures configuration at a power input of 75 W.

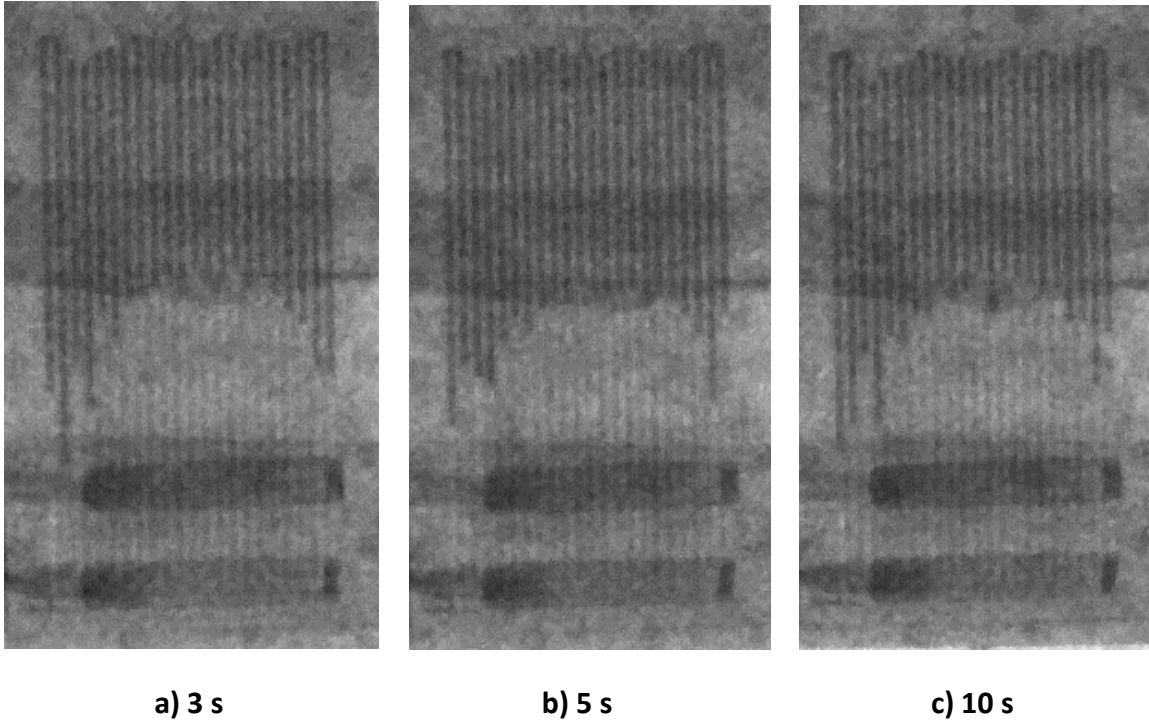


Figure 3.10. Liquid and vapor distribution in the condenser nanostructures configuration at a power input of 225 W.

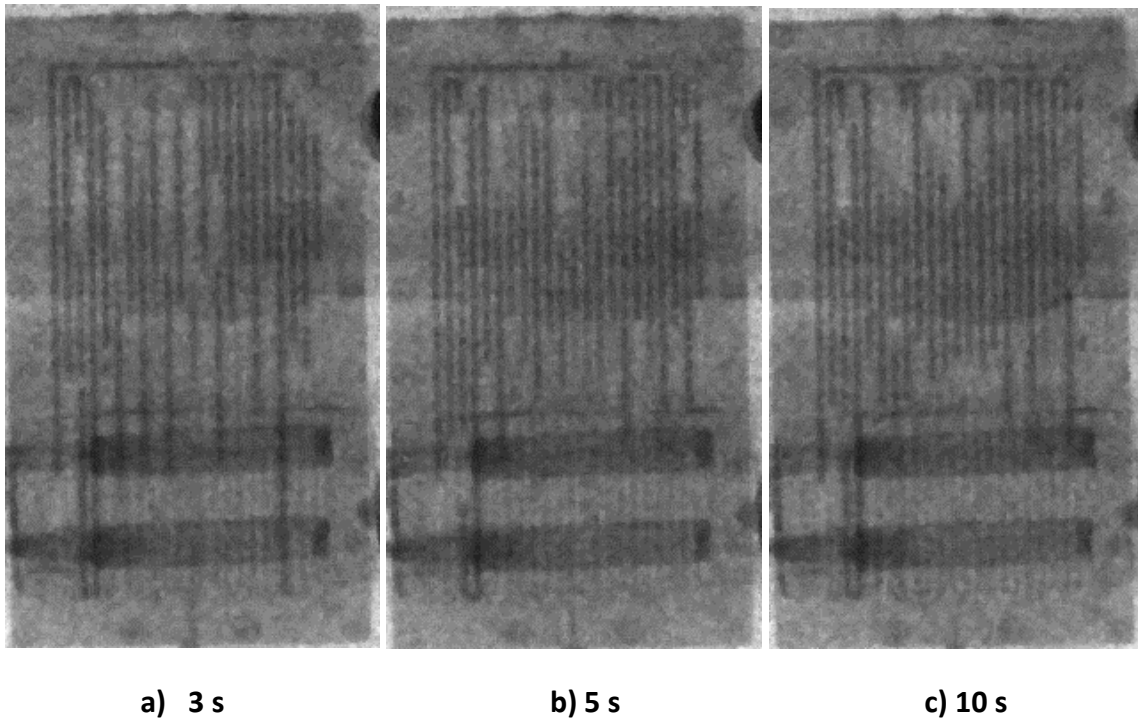


Figure 3.11. Liquid and vapor distribution in the evaporator nanostructures configuration at a power input of 115 W.

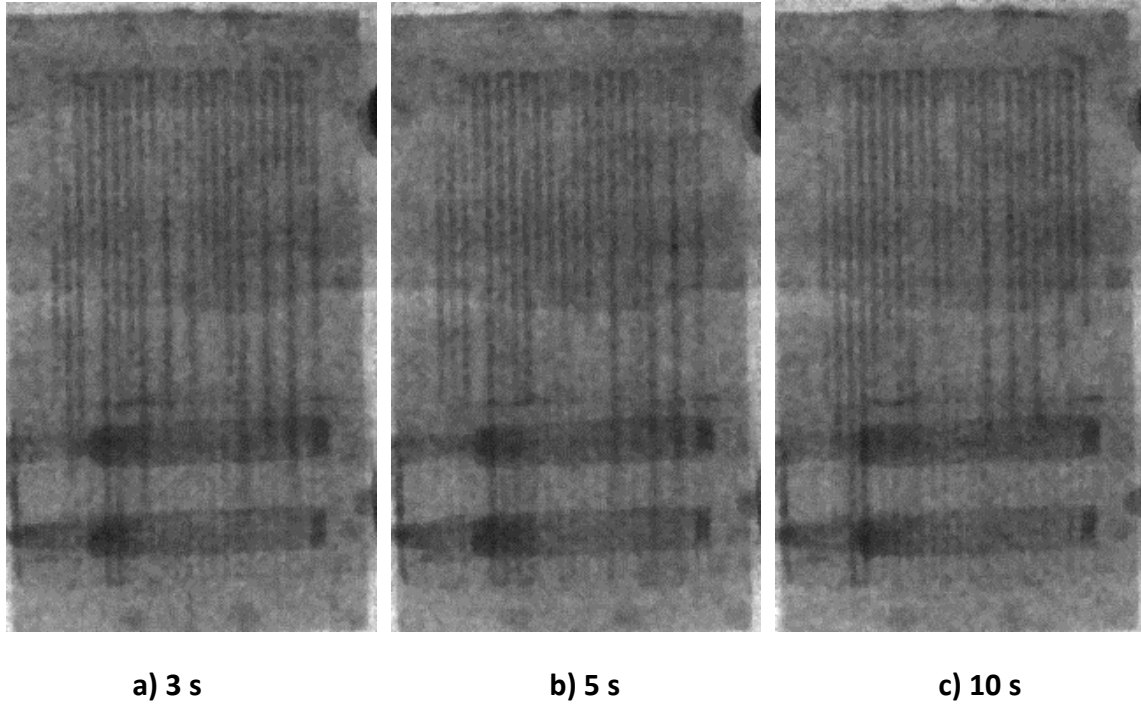


Figure 3.12. Liquid and vapor distribution in the evaporator nanostructures configuration at power input of 225 W.

After 1.5 years, a repetition of the thermal tests was completed. The results shown in Figure 3.13 and Figure 3.14 demonstrate a loss in performance most likely due to leakage from the seams where the OHP channels connect to the cover plate. The worst performance is the second 1.5 year test (T2) which immediately occurs after T1 was tested. The immediate testing seems to be the commonality for both the CuO evaporator and CuO condenser tests. This means that high usage is not recommended after 1.5 years.

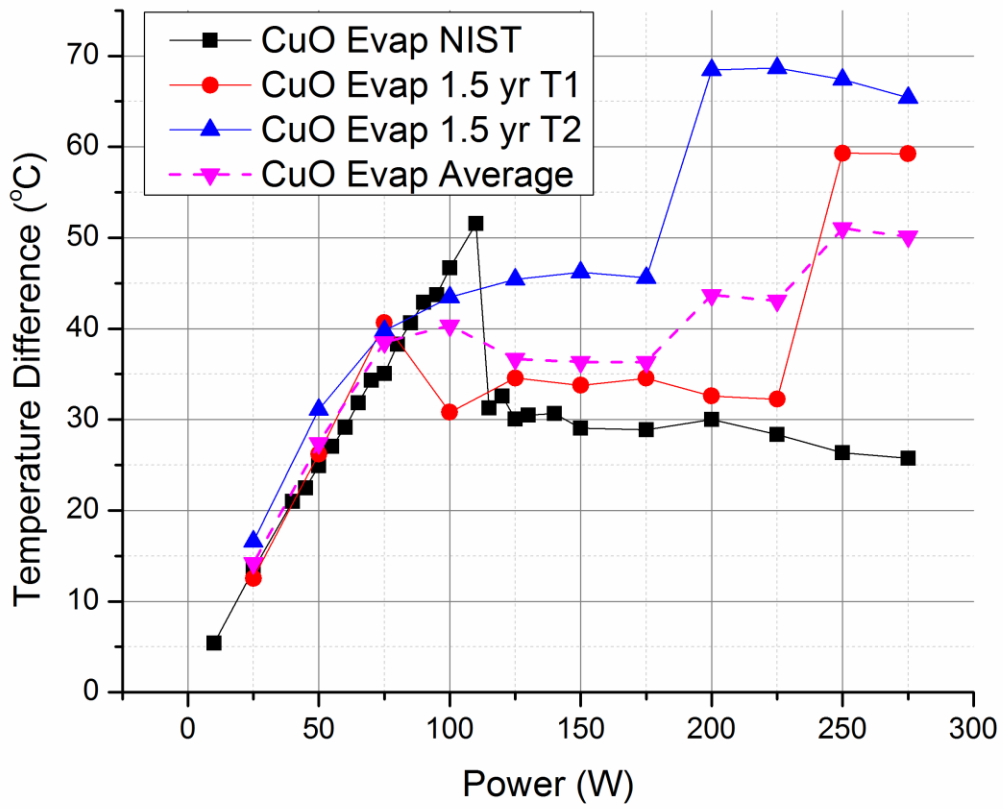


Figure 3.13. CuO in evaporator temperature difference measurements with data after 1.5 years.

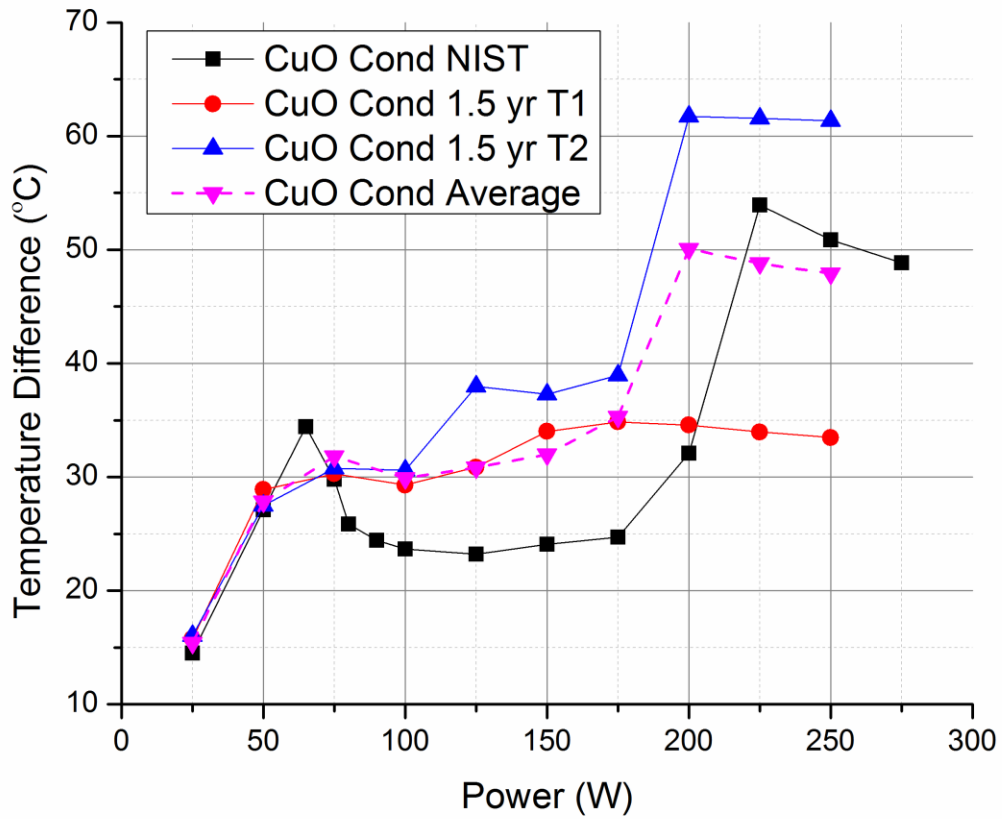


Figure 3.14. CuO in condenser temperature difference measurements with data after 1.5 years.

The average temperature differences of the plots from Figure 3.13 and Figure 3.14 are plotted against the non-treated version from the original NIST experiment is shown in Figure 3.15. The interesting piece is when comparing the trend of Figure 3.15 to the nanofluid OHP experiment performed by Ma et al [7]. Note the trend has a high performance enhancement near the beginning of the power input right when the OHP starts to oscillate. As the OHP goes to higher power inputs, the performance starts deteriorating.

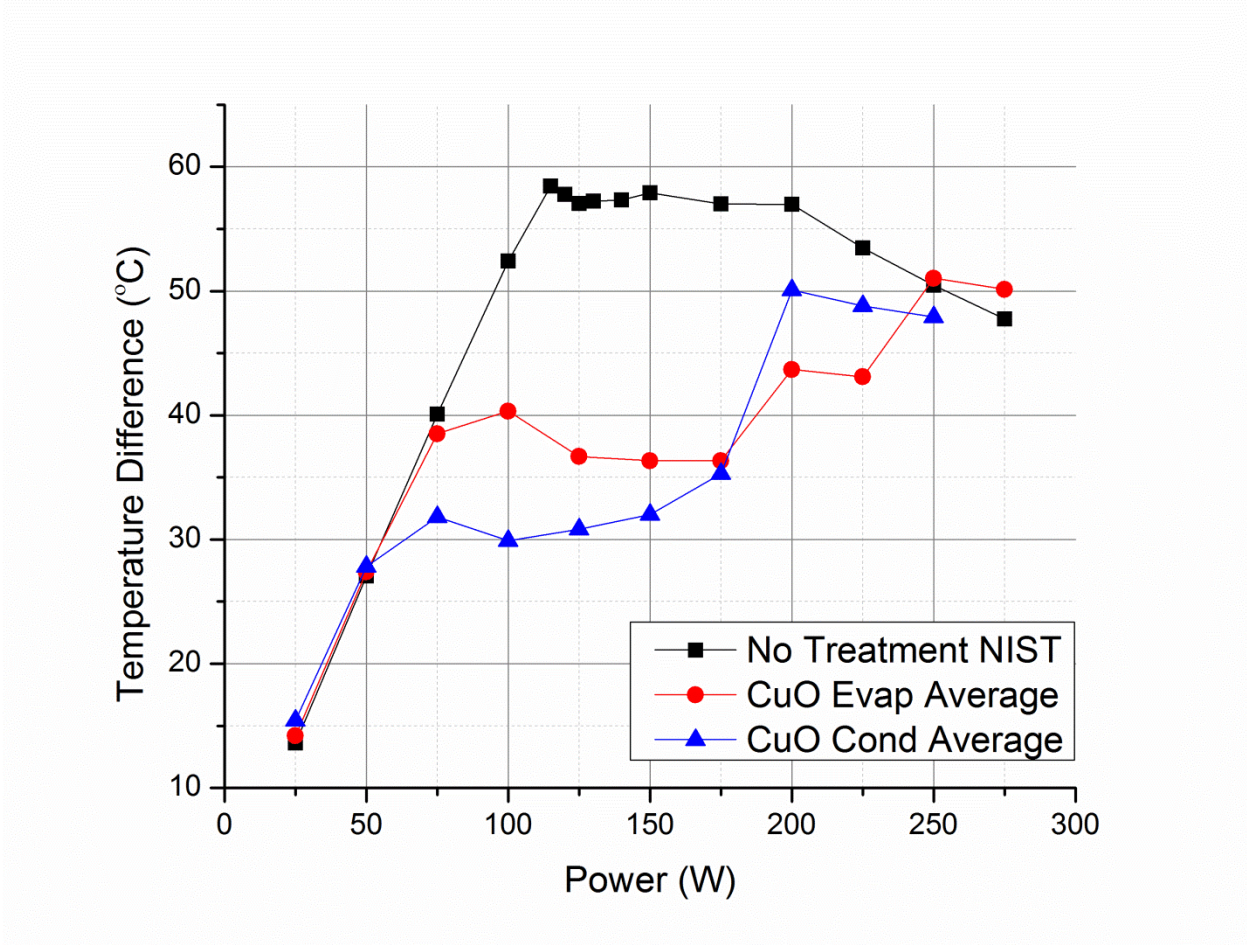


Figure 3.15. Comparison of average performance 1.5 years later to the original untreated OHP.

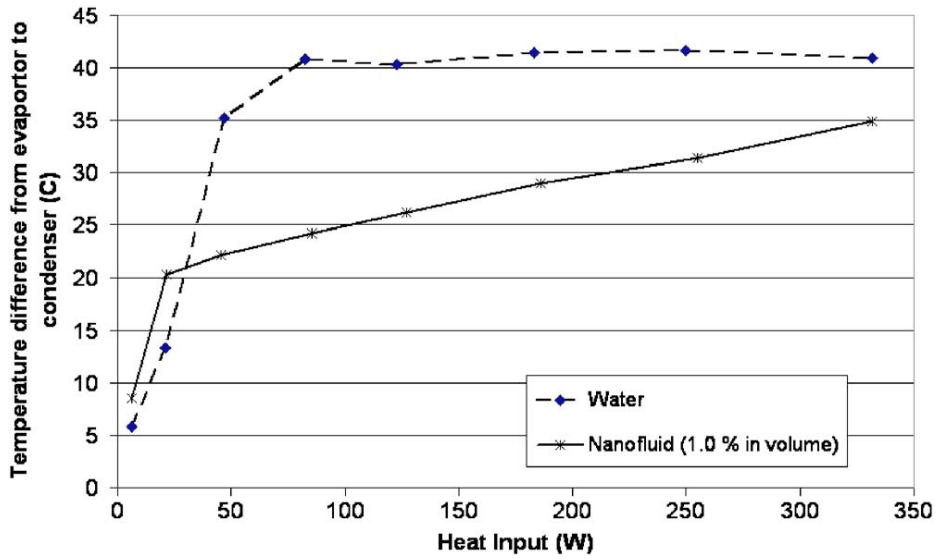


Figure 3.16. Temperature difference plot of a nanofluid OHP comparison from Ma et al [8].

3.4 SUMMARY

With the localized heat flux projected to be over 10 MW/m^2 with powers exceeding 300 W, the current low-cost thermal solutions on the market are limited in their ability to remove the heat of operation. The performance of a FP-OHP selectively treated with CuO nanostructures can far exceed a similar nontreated FP-OHP in this study and provides a promising novel approach for thermal solutions. Nanostructures in the evaporator improved thermal performance over the whole heat input range studied once fluid motions begin. In contrast, nanostructures in the condenser initiated oscillating motion and a corresponding thermal performance improvement at a lower heat input. However, the thermal performance improvement disappeared at higher heat input, which corresponds to the nanostructures being covered by the liquid phase and thus presumably not being able to contribute to enhanced vapor condensation. However after a 1.5 year repetition of the experiment performance is still better than the original control in some areas but deterioration is expected. The interesting component is the close trend following Ma et al. 2006 experiment done with nanofluids. This suggests there is a correlation between nanofluids and surface treatments. The reasoning for the strong correlation is due to the nanofluid deposition onto the surface of the internal channels causing changes in the wettability of the OHP which alters beneficially the performance.

4 HYBRID SUPERHYDROPHOBIC/SUPERHYDROPHILIC OSCILLATING HEAT PIPE

In this study, a hybrid hydrophilic and hydrophobic treatment of the OHP was investigated to study the effect of wetting on the heat transfer performance of a FP-OHP. Three FP-OHP configurations were investigated: 1) the evaporator inner surface is treated hydrophilically and the condenser hydrophobically; 2) the evaporator inner surface is treated hydrophobically and /condenser hydrophilically; and 3) both sections untreated. In addition, SEM was used to characterize the surface structures, a sessile drop test was used to measure the contact angle, i.e., determine the wetting condition, and TDMS was used to measure the plasmas polymer treatment.

4.1 EXPERIMENTAL INVESTIGATION

4.1.1 FP-OHP CNC Fabrication

In order to investigate the nanostructured surface effect on the heat transfer performance, a FP-OHP as shown in Figure 4.1 was developed. The FP-OHP design consists of the evaporator, adiabatic section, and condenser with the overall dimensions of FP-OHP being 122.30 mm x 60.80 mm x 3.5 mm. The evaporator section has a heated area of 25.4 mm x 50.80 mm; the adiabatic has an area of 57 mm x 50.80 mm; and the condenser section has a cooling area of 30 mm x 50.80 mm. The internal channels consist of 14 turns with dimensions of 1 mm width x 1.5 mm depth for better neutron imaging contrast. The fabrication process used Cu 110 alloy for its low cost and excellent thermal conductivity. Each FP-OHP, as shown in Figure 4.2, is

CNC machined with the exposed groove side lapped to a flatness difference between maximum and minimum height of less than 0.0025 mm for optimal sealing.

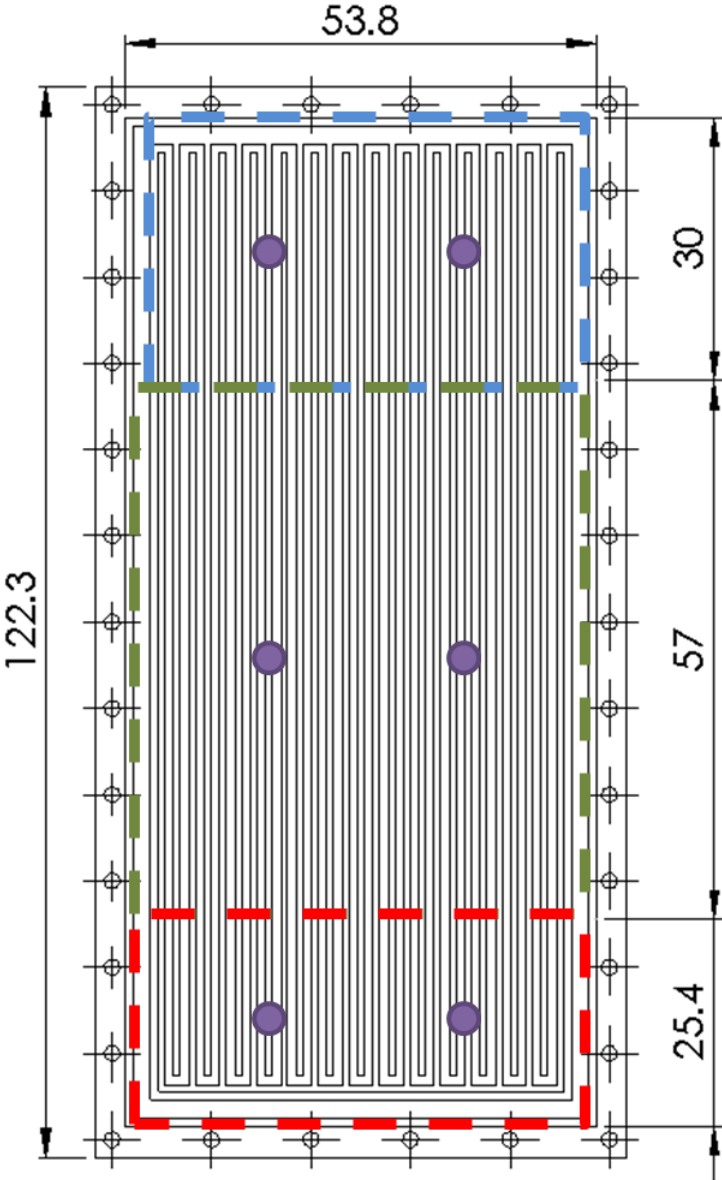


Figure 4.1. Schematic of a large FP-OHP investigated (all dimensions in mm). Purple circles indicate thermocouple location. Blue dashed line is the condenser section, green dashed line indicates the adiabatic section and red dashed line indicates the evaporator section.

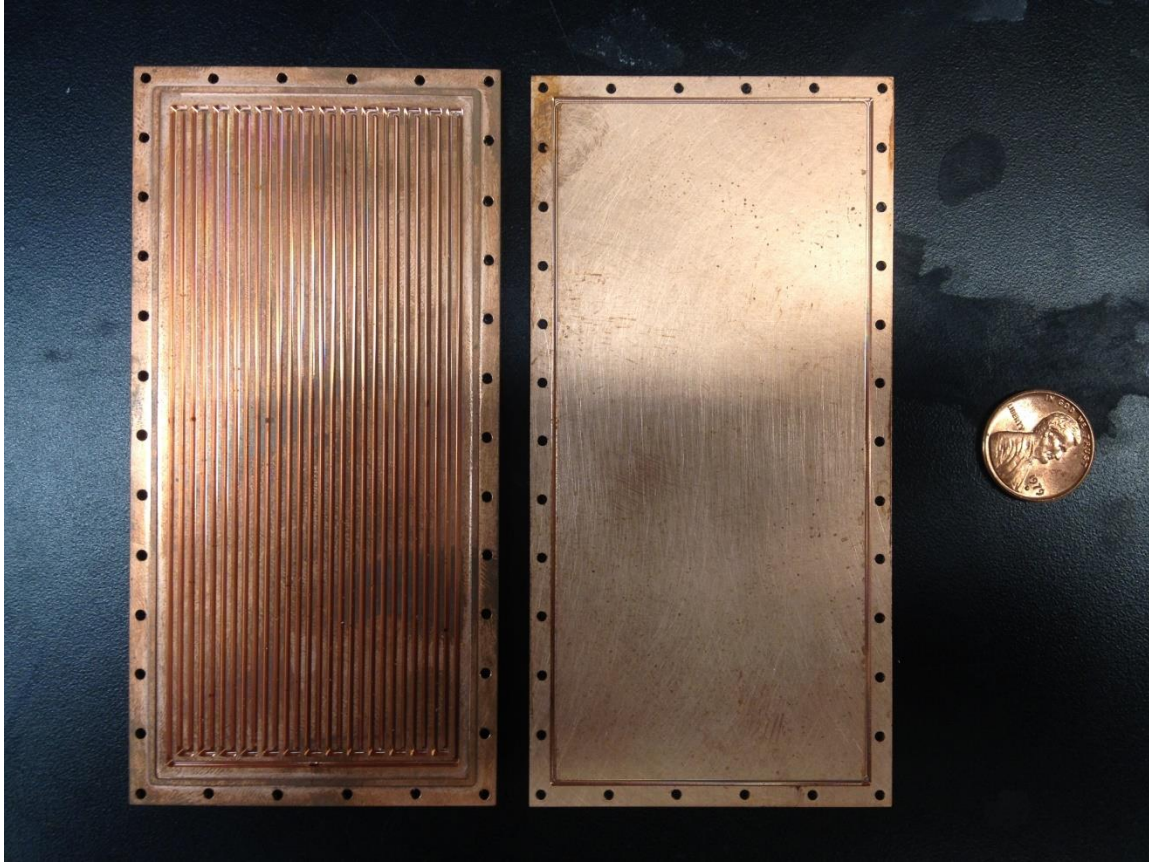


Figure 4.2. Fabricated FP-OHP with cover plate.

4.1.2 Nanostructure Growth

In the chemical treatment process, the hierarchical cupric oxide (CuO) nanostructures were produced on the surfaces using the procedure outlined in Liu *et al.* [30]. The machined FP-OHP and its cover plate were ultrasonically cleaned in 3.0 M HCl aqueous solution for 10 minutes. Ethanol and distilled water were used to remove residual HCl. The nanostructures were prepared by then immersing the copper in a 30 mM NaOH aqueous solution. To confine the nanostructured surface to the selected region, only the evaporator section of the FP-OHP, along with one third of the cover plate, was submerged in the solution. The entire treatment was performed inside a glass beaker that was sealed using Parafilm® and the nanostructured

CuO was allowed to grow in an oven at 60 °C for 20 hours. The FP-OHP was then washed with distilled water and allowed to dry before assembling the FP-OHP and cover plate following the sealing method described later.

4.1.3 Plasma Polymer Nanocoating Deposition

Cu(II) oxide FP-OHP was mounted to a two-row aluminum panel sample-holding frame. A copper mask as seen in Figure 4.3 was manufactured to cover the hydrophilic surfaces and expose the remainder for the plasma polymer deposition. The entire FP-OHP along with the mask was then wrapped in aluminum foil and was gripped by a metal clip in two corners in order to maximize the surface area for nanocoating deposition. Silicon wafers were included with the batches for coating thickness assessment during the deposition process. The aluminum sample holder was placed inside an 80-liter bell jar-type reactor and positioned between two titanium plates. For plasma treatment and nanocoating deposition, the aluminum panel and Cu(II) oxide coupons served as the cathode whereas the titanium panels served as electrically-grounded anodes. The electrodes were connected to the output of a MDX-1K magnetron drive (Advanced Energy Industries, Inc., Fort Collins, CO), which served as the DC excitation source. After closure and sealing of the chamber, the reactor was pumped to base pressure (< 1 mTorr) using a mechanical pump and booster pump connected in series. Oxygen plasma was utilized to remove organic contaminants from the Cu(II) oxide surface. Pure oxygen (Praxair, Inc., Danbury, CT) was introduced to the reactor at a flow rate of 1 standard cubic centimeter per minute (sccm) using an MKS mass flow controller (MKS Instruments, Inc., Andover, MA) and MKS 247C readout to adjust the flow rate. Reactor pressure was allowed to stabilize at 50 mTorr using an MKS pressure controller. The oxygen

was excited with the DC power supply at an applied power of 20 W in order to initiate the plasma glow discharge. Oxygen plasma treatment time was 2 min. Following oxygen plasma pre-treatment, the reactor was pumped to base pressure. Trimethylsilane (TMS, Gelest, Inc., Morrisville, PA) was introduced to the reactor at a flow rate of 1 sccm. Reactor pressure was allowed to stabilize at 50 mTorr. TMS plasma glow was initiated with the DC power supply at 5 W for 15 s.

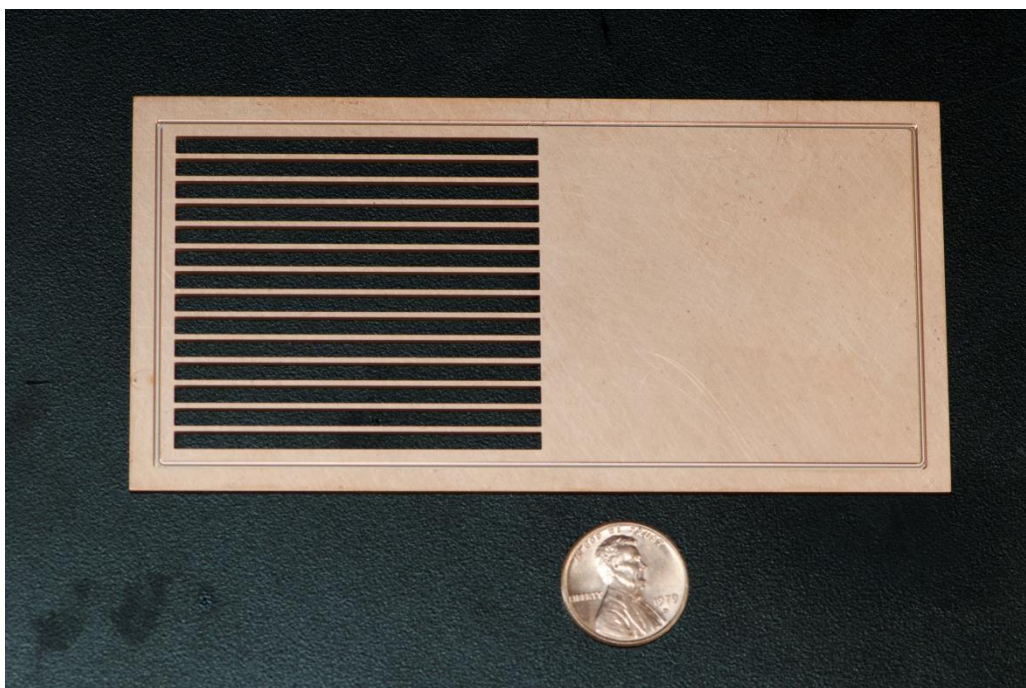


Figure 4.3. Template to cover hydrophilic FP-OHP and expose surface for plasma polymer treatment.

4.1.4 Characterization

SEM (FEI Quanta) was used to characterize the surface structure as shown in Figure 4.4. The magnified objects as shown in Figure 4.4 confirm the presence of hierarchical grass-like sheets of CuO reported by Liu et al. [30]. Each grass-like sheet has what appears to be a sharp

tip with additional roughness along the edges. This morphology greatly increases the roughness of the surface and thereby alters its wettability. A conventional sessile-drop technique employing a goniometer setup (VCA 2500 XE) was used to determine the wettability of the structures. In Figure 4.5, the hydrophilic CuO (top) has a contact angle of 0° compared to an untreated copper surface (middle) with a contact angle of $\sim 60^\circ$. At the bottom of Figure 4.5, there is a superhydrophobic [35] plasma polymer coated surface on top of existing CuO structures which has a contact angle of $\sim 152^\circ$ - 154° . These characterizations suggests Wenzel behavior [31] for the hydrophilic CuO surface and a Cassie-Baxter[36] behavior for the superhydrophobic plasma polymer treated surfaces.

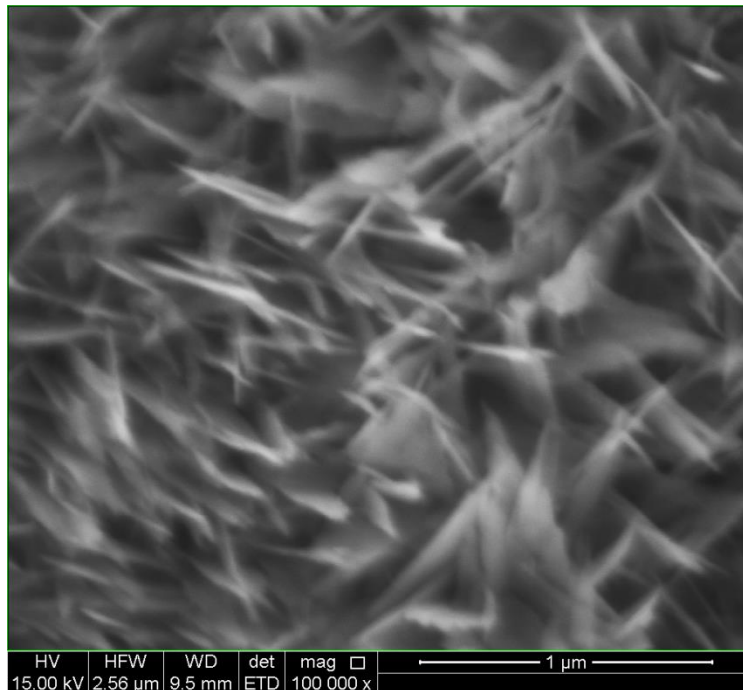
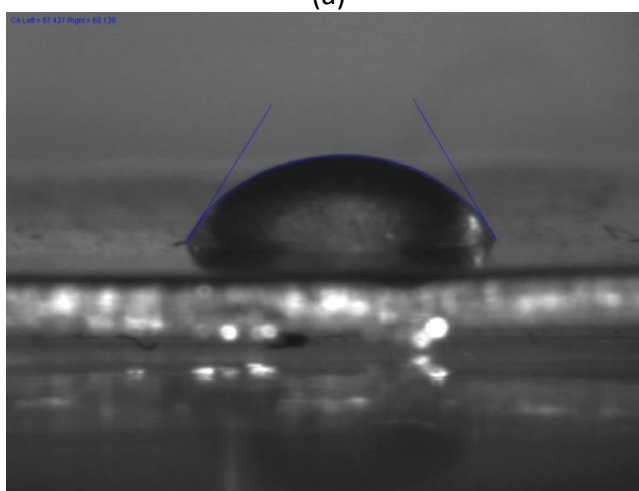


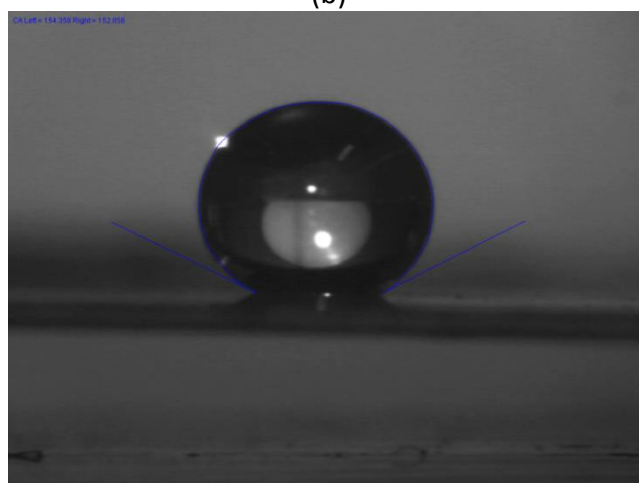
Figure 4.4. SEM image of the CuO nanostructures with magnification of 100,00X.



(a)



(b)



(c)

Figure 4.5. Contact angle measurements; (a) sessile drop test on a treated CuO (top) with contact angle of 0° ; (b) nontreated copper (middle) with contact angle $\sim 60^\circ$; and (c) a treated CuO with an additional plasma polymer layer with contact angle of $\sim 152^\circ$ - 154° .

Surface elemental composition was determined through X-ray photoelectron spectroscopy (XPS) as seen in Figure 4.6. A Kratos Axis 165 X-ray photoelectron spectrometer was utilized for analysis. Surface composition was determined for uncoated and TMS-nanocoated copper and copper(II) oxide substrates. XPS utilized a monochromatic Al K α X-ray (1486.6 eV) source operating at 150 W. X-ray source take-off angle was 90° relative to the sample surface. Standard spot size (200 μm \times 200 μm) was utilized for XPS analysis. High resolution spectra were charge compensated by adjusting the binding energy of the C 1s peak to 284.5 eV. C 1s peaks were fitted after Shirley background subtraction using CASA XPS (Casa Software Ltd., version 2.3.15).

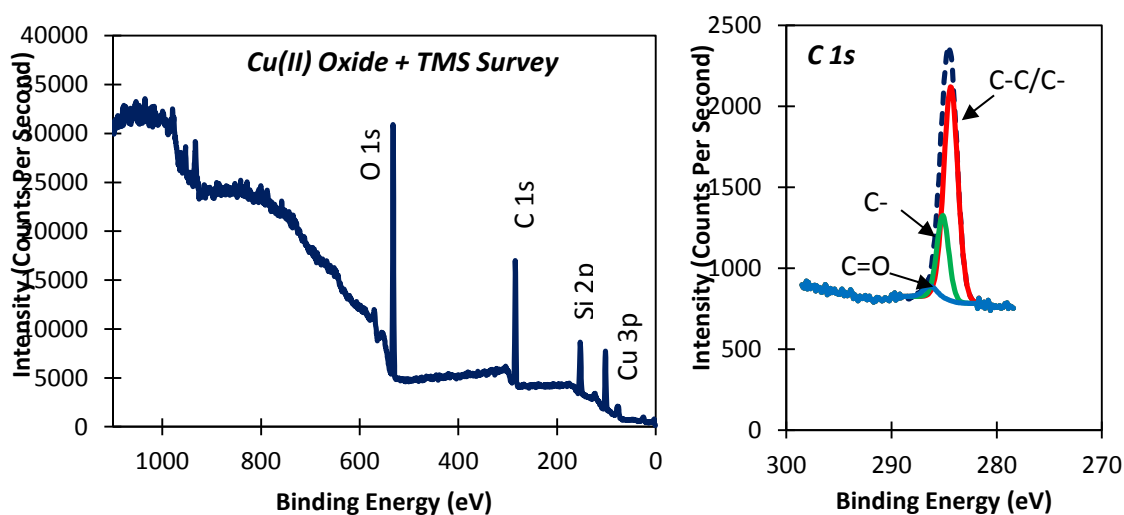


Figure 4.6. XPS analysis.

4.1.5 Assembling and Charging

The use of nanostructures limits sealing of the assembly to low-temperature methods (< 200 °C). The FP-OHP incorporates adhesives, a tongue and groove joint, and a mechanical seal to meet these requirements. Once the nanostructures were grown on the FP-OHP and characterized, the groove surrounding the interior channels (see Figure 4.2) was filled with EPO-

TEK-301, a low outgassing epoxy adhesive. The cover plate had a matching tongue partially filling the groove. The holes outside the tongue were used for screws, which applied an additional mechanical force to join the plates. Afterwards, Vacseal® was applied along the exterior seam between the plates to achieve a vacuum tight seal.

After a day of curing, fluid charging can be started. First, the base weight of the system is measured with only air in the channels. Then the newly sealed channels are evacuated using a rotary pump. Once the vacuum is at an acceptable level ($< 10^{-3}$ Torr), the is isolated and high-performance liquid chromatography (HPLC) grade water is then circulated in the FP-OHP system via an additional line. The completely filled FP-OHP is then weighed. At this point, the HPLC line is closed and the vacuum line is opened to pull out 35% of the water resulting in a charging ratio of 65%. The FP-OHP is then reweighed and the charging tube lines are crimped and soldered to prevent any leaking.

4.2 THERMAL TESTING

The thermal portion of the experimental setup, shown in Figure 4.7, consisted of one 750 W power supply for two ceramic aluminum nitride heaters (1"x1" each) attached to the evaporator of the OHP, one custom aluminum cooling block for the condenser, one high-capacity cooling bath for the condenser, and a data acquisition system (DAQ) to record temperatures. A total of 6 type-T thermocouples were used to measure the temperatures in the three regions of the FP-OHP, as shown in Figure 4.1. Each pair of thermocouples was placed in the center of evaporating, adiabatic, and condenser sections equidistant along the short side. Temperatures on all thermocouples were recorded at 500 Hz using a National Instruments SCXI-1000 box with SCXI-1303 card for the data acquisition system with SignalExpress software.

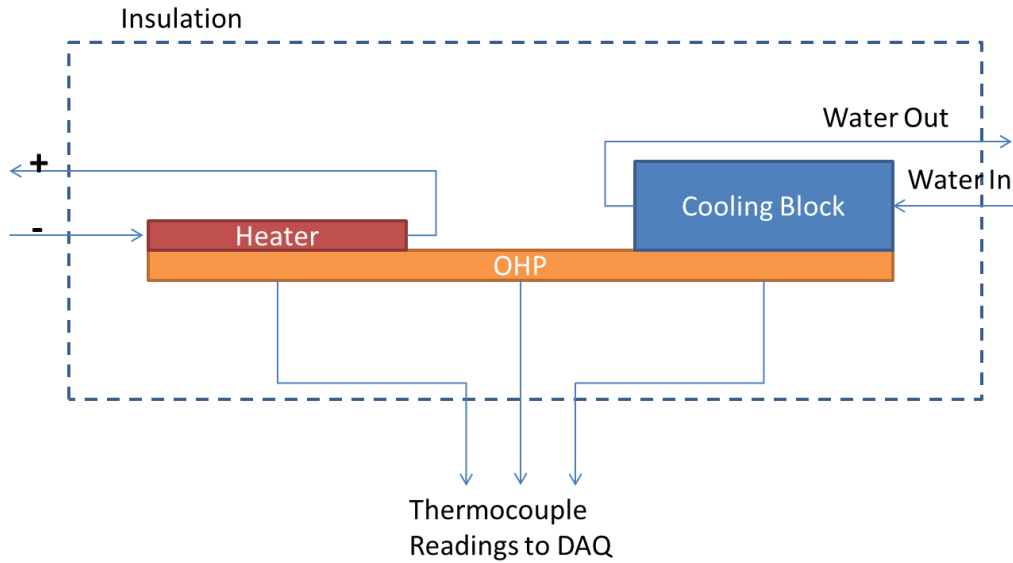


Figure 4.7. Schematic of the entire experimental setup.

The FP-OHPs were set in a vertical orientation for all tests with the condenser on top. Heat was conducted onto the FP-OHPs with a $50.80 \times 25.4 \text{ mm}^2$ footprint, while the other end of the FP-OHP was cooled with a flow-through block of area $50.80 \times 30 \text{ mm}^2$. The heat input was controlled with an Agilent N5750A power supply with a resolution of $\pm 0.01 \text{ W}$. Deionized water was circulated through the aluminum cooling block and temperature-controlled to $20 \text{ }^\circ\text{C}$ ($\pm 0.5 \text{ }^\circ\text{C}$) with the cooling bath (Julabo FP40). Four C-clamps held the cooling block and the heating elements onto the FP-OHP. Thermal paste (Omegatherm “201”) was used between all contact surfaces to reduce thermal resistance. Fiberglass was used to insulate the system from the surrounding environment.

The system was first allowed to reach steady state with no heat input. Then heat was added into the system, and the FP-OHP was allowed to reach a steady state with temperature data collected for 3 minutes at each step. The maximum heat input was 150 W . All thermocouple data were read through the DAQ and recorded on the personal computer.

Four tests were conducted, measuring thermal performance over a range of heat inputs from 0 W to 150 W at increments of 25 W. All measurements were repeated at least three times over the range of heat inputs with the same setup. First a copper plate of the same size as the FP-OHP was tested as the baseline data set. Second, a control FP-OHP with no surface treatments was tested to demonstrate typical performance. Third, the FP-OHP with a hydrophilic evaporator and hydrophobic condenser was tested then recharged and tested again to negate charging effects; and fourth, the FP-OHP was flipped where the evaporator is now hydrophobic and the condenser is hydrophilic and was recharged and tested also.

4.3 RESULTS

A pure copper plate, untreated FP-OHP, hydrophilic evaporator/hydrophilic condenser FP-OHP, and hydrophobic evaporator/hydrophilic condenser FP-OHP were tested. In Figure 4.8 the heating input effect on the temperature difference is compared amongst all the previous stated configurations. The temperature difference plotted is the average of the two evaporator thermocouples minus the average of the two condenser thermocouples. A smaller temperature difference implies better thermal performance of the FP-OHP. All FP-OHP configurations show a linear dependence from 25 W to 75 W which means it behaves as a solid like the bare copper shown in Figure 4.8. Just after 75 W, all FP-OHP configurations started oscillating and deviate from bare copper. The temperature difference comparison of the hybrid FP-OHP compared to untreated FP-OHP showed a 15% worse performance.

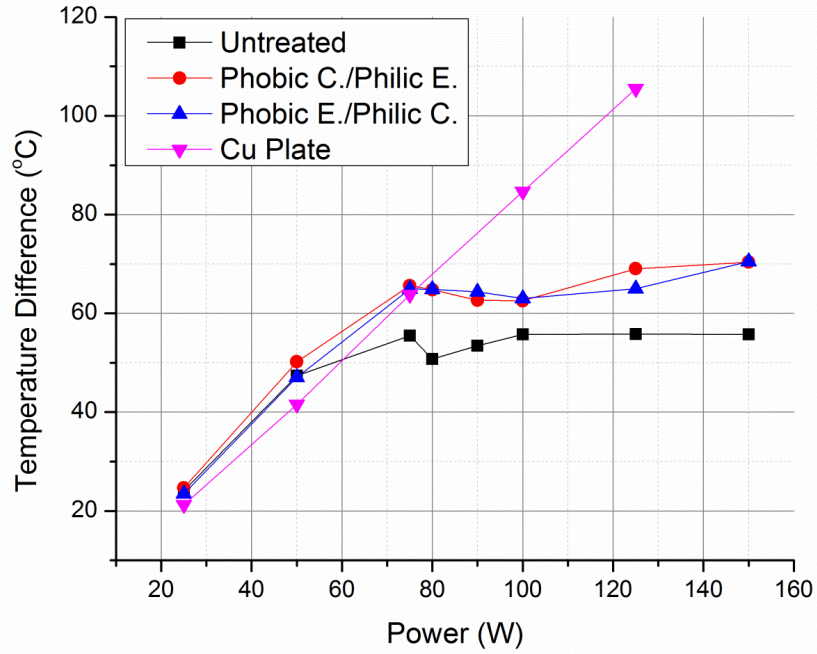


Figure 4.8. Comparison of temperature difference with multiple runs of the hybrid FP-OHP.

In Figure 4.9, the thermal resistance comparison is seen amongst all configurations and bare copper. The thermal resistance is the temperature difference divided by the heat input. A lower thermal resistance means better performance. Once oscillation starts with the FP-OHPs, the thermal resistance starts decreasing compared to bare copper.

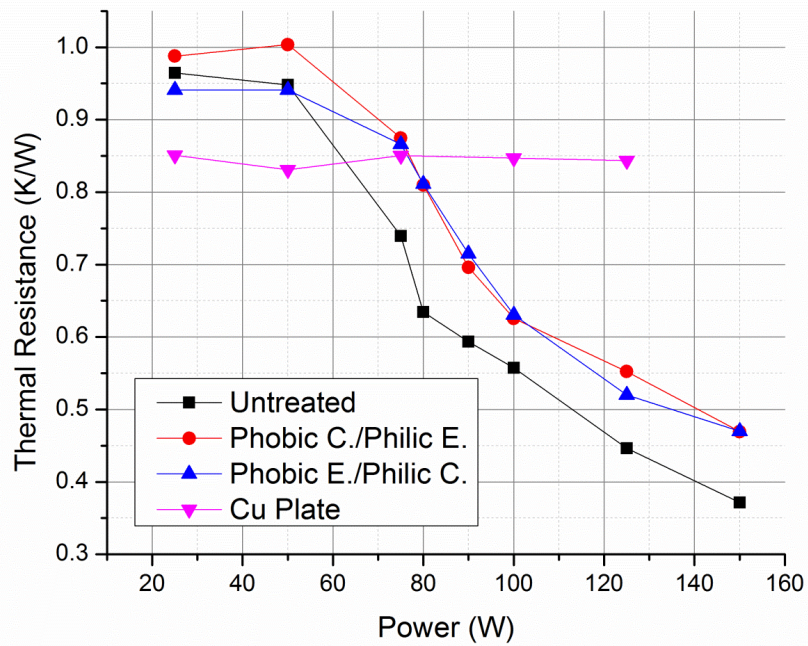


Figure 4.9. Thermal resistance versus power input.

A comparison of multiple condenser temperatures as seen in

Figure 4.10 and multiple evaporator temperatures as seen Figure 4.11 was made to view consistency.

Figure 4.10 for the condensers all show very consistent linear temperature profile due to large amounts of cooling from the cooling block. Figure 4.11 shows a nonlinear temperature profile most likely due to the oscillation patterns.

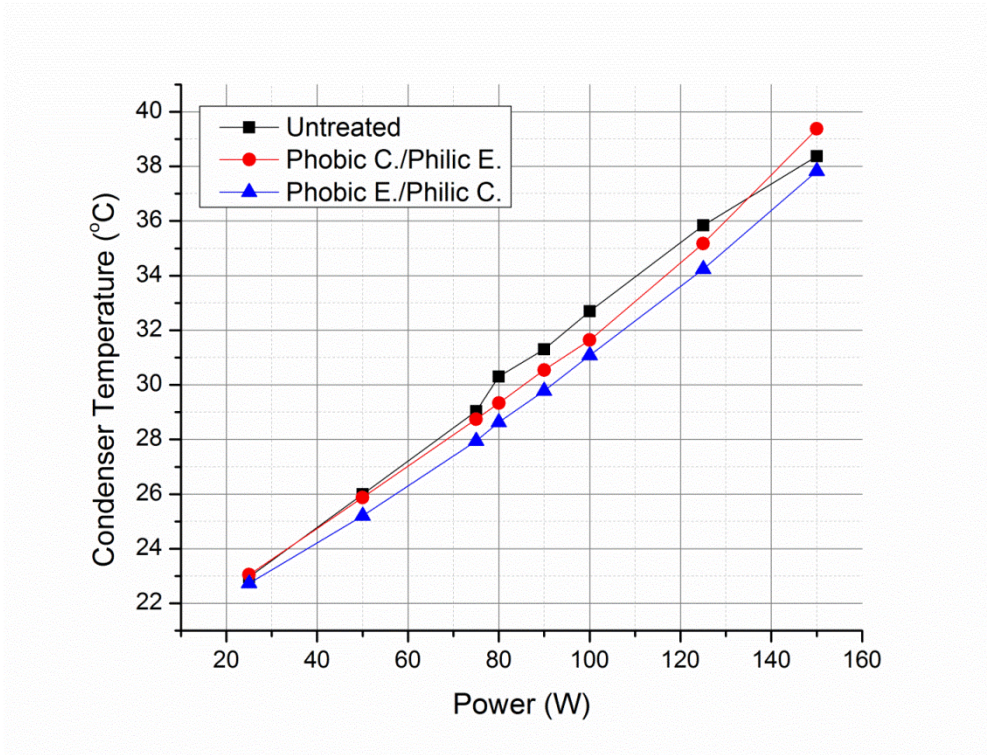


Figure 4.10. Condenser temperature comparison as a function of power input.

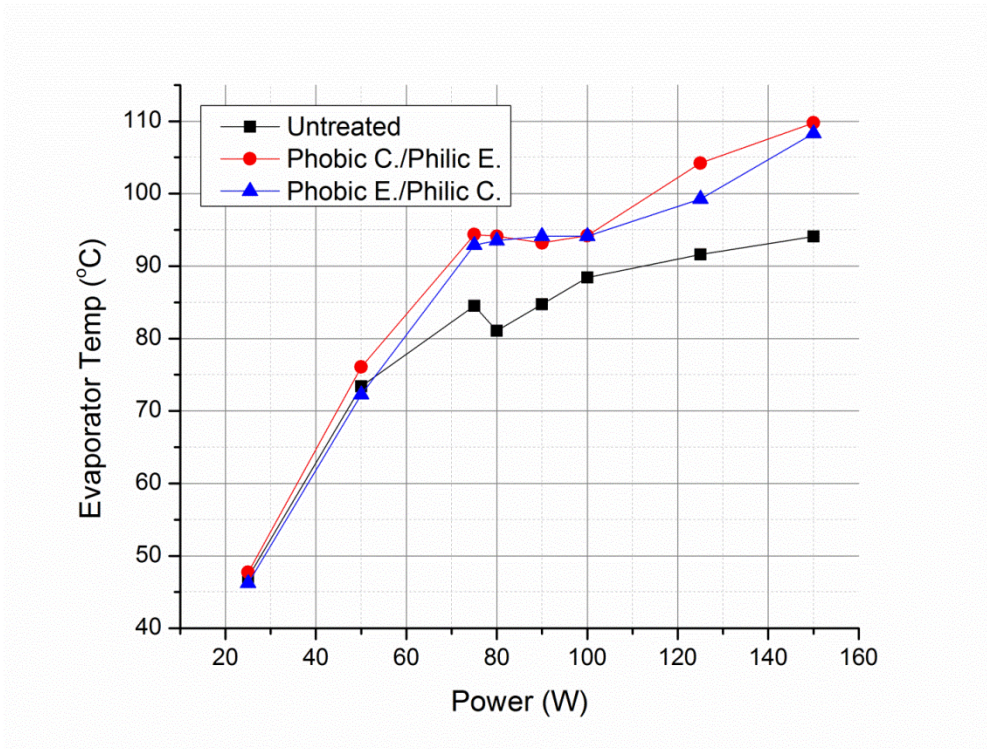


Figure 4.11. Evaporator temperature comparison as a function of power input.

When observing the steady state temperature oscillations of the three FP-OHP configurations as seen in Figure 4.12, notice the untreated FP-OHP has much higher amplitude of temperature ranges compared to the two hybrid FP-OHP configurations. A normalized version can be viewed in Figure 4.13. In the condenser side, a similar condition can be viewed as seen in Figure 4.14 and the normalized Figure 4.15. In order to characterize this phenomenon, a standard deviation was taken of the temperatures in the evaporator and condenser as seen in Figure 4.16 and Figure 4.17 respectively. In observing Figure 4.16 and Figure 4.17, notice the untreated has a much higher standard deviation compared to both the hydrophilic/hydrophobic configurations. This implies that the surface treatments are altering the oscillations occurring in the FP-OHP.

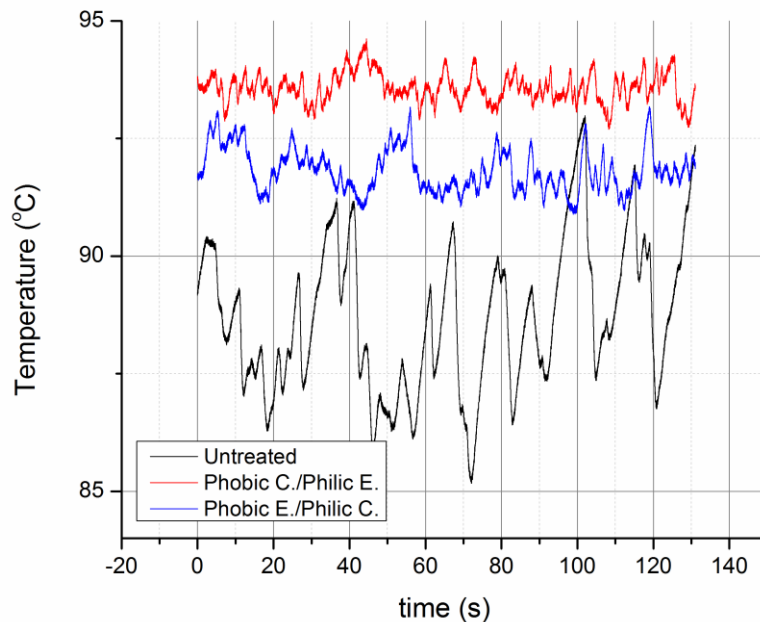


Figure 4.12. Steady state temperature oscillation in the evaporator at 100 W.

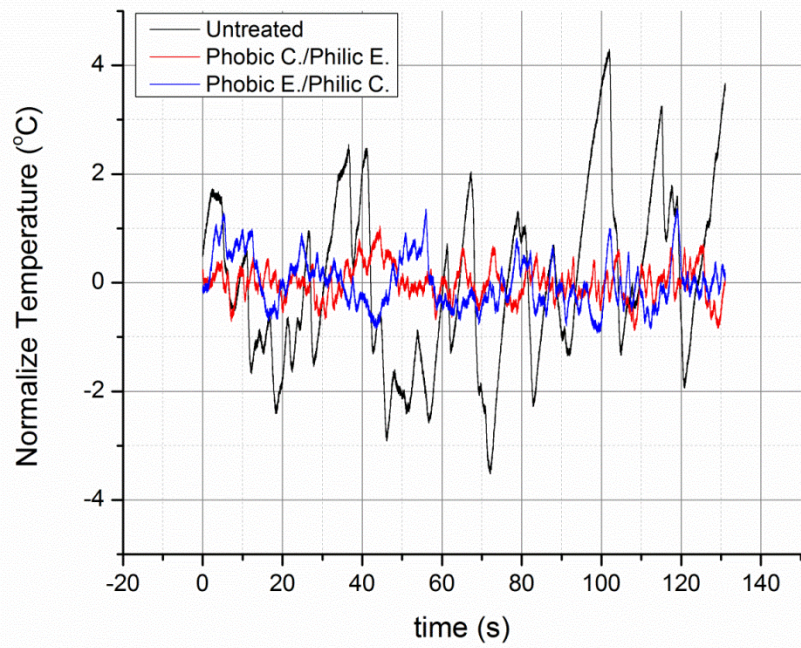


Figure 4.13. Normalized temperature oscillations at 100 W heat input in the evaporator.

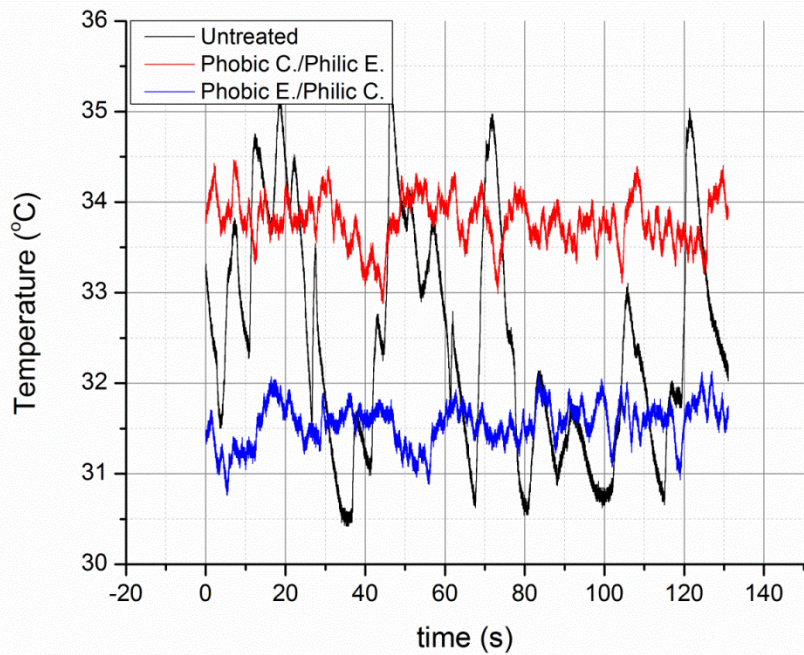


Figure 4.14. Temperature oscillations in condenser at 100 W heat input.

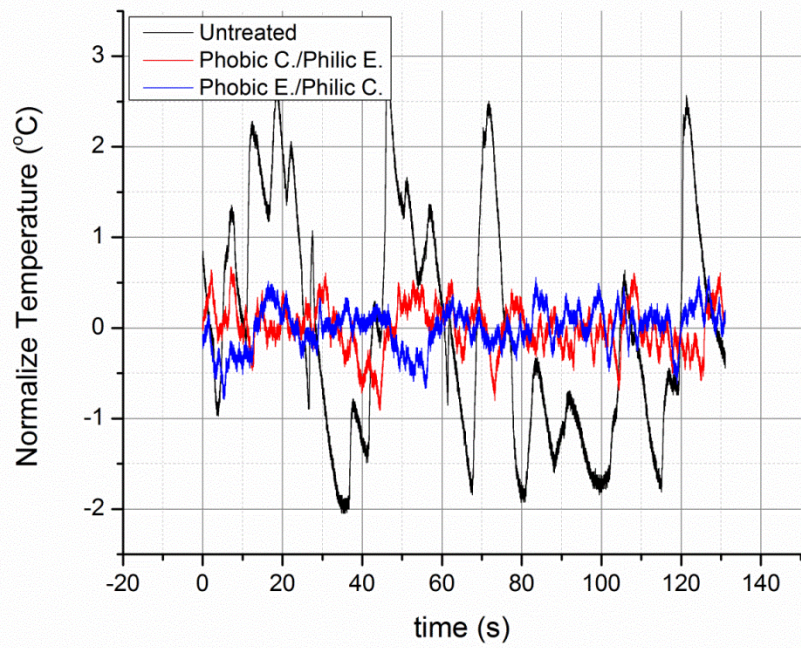


Figure 4.15. Normalized temperature oscillations in condenser at 100 W heat input.

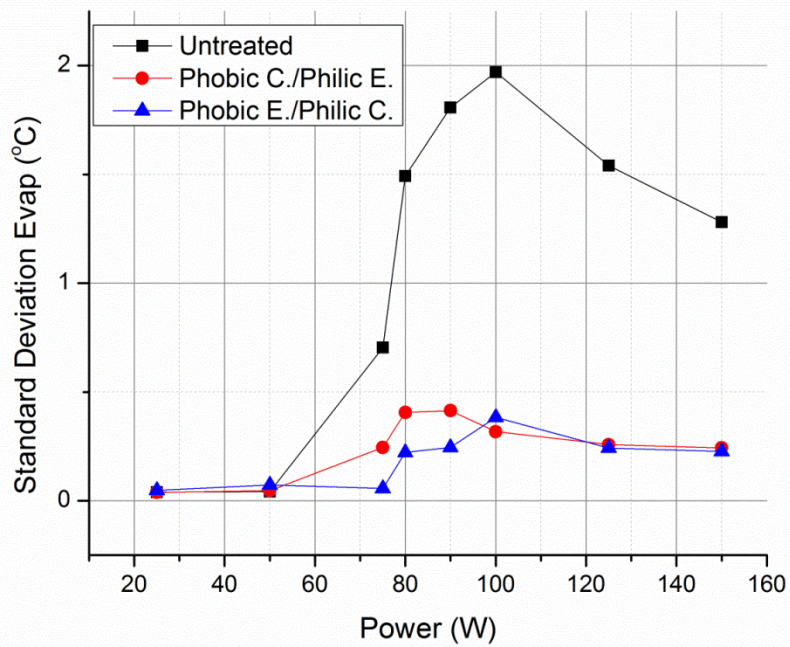


Figure 4.16. Standard deviation comparison of the evaporation temperature versus power.

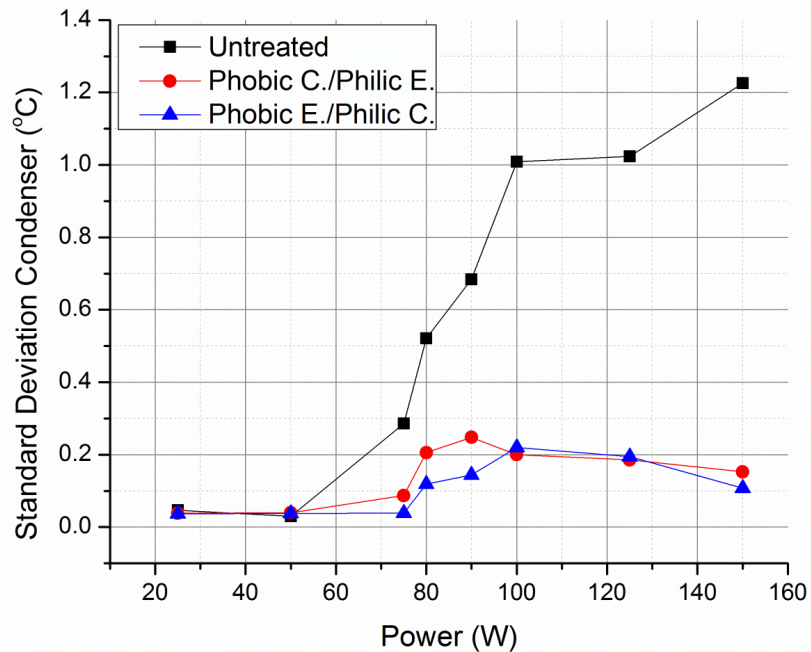


Figure 4.17. Standard deviation comparison of the condenser temperature versus power.

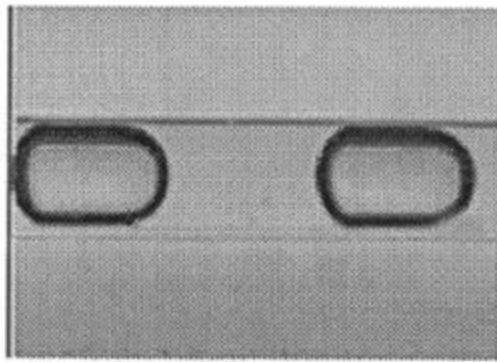
4.4 SUMMARY

Applications that require better thermal performance but emphasize strict temperature variance control may find a promising solution in the hybrid FP-OHP. The hydrophilic/hydrophobic configurations in evaporator and condenser and then vice versa seem to have no advantage over each other in terms of thermal performance and temperature uniformity. The overall thermal performance of the hybrid FP-OHPs seem to be about 15% worse, but has a much better oscillation amplitude control compared to the untreated FP-OHP.

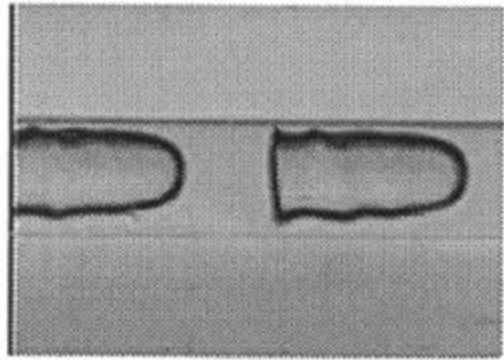
5 OPERATING LIMIT OF AN OSCILLATING HEAT PIPE

5.1 INTRODUCTION

Taylor or slug flow named after G.I. Taylor [37] is where the liquid slug and vapor bubble or Taylor bubble both coexist in the same confinement typically on the order of microchannels as seen in Figure 5.1. In an OHP, this flow exists as the so called slug flow due to the similarity of velocities in the liquid and vapor as seen in Figure 5.2. Neutron radiography [32, 33, 38, 39] further verified the existence of Taylor flow as seen in Figure 5.3. The area of interest in Taylor bubbles from OHP perspective is the relationship of velocity to the film thickness that exists in the bubble as the fluid moves due to the thin film evaporation that occurs to create enough pressure to drive the OHP. Fairbothor and Stubbs [40] were the ones to perform the first experiments related to Taylor bubbles, but Taylor[37] expanded the flow velocity relationship to film thickness with highly viscous fluids. Later Brethorton [41] developed a theoretical model, but was only for a small range of velocities. Aussillous and Quere[42] experimented with a much broader variations of fluids and velocities compared to Taylor. Finally Han and Shikazono [43] produced a set of experimental data comparing three working fluids along with a correlation of the film thickness of the Taylor bubble as a function of velocity.



4(c) $U_{LS} = 0.213 \text{ m/s}$
 $U_{GS} = 0.154 \text{ m/s}$



4(d) $U_{LS} = 0.608 \text{ m/s}$
 $U_{GS} = 0.498 \text{ m/s}$

Figure 5.1. Taylor bubble [44].

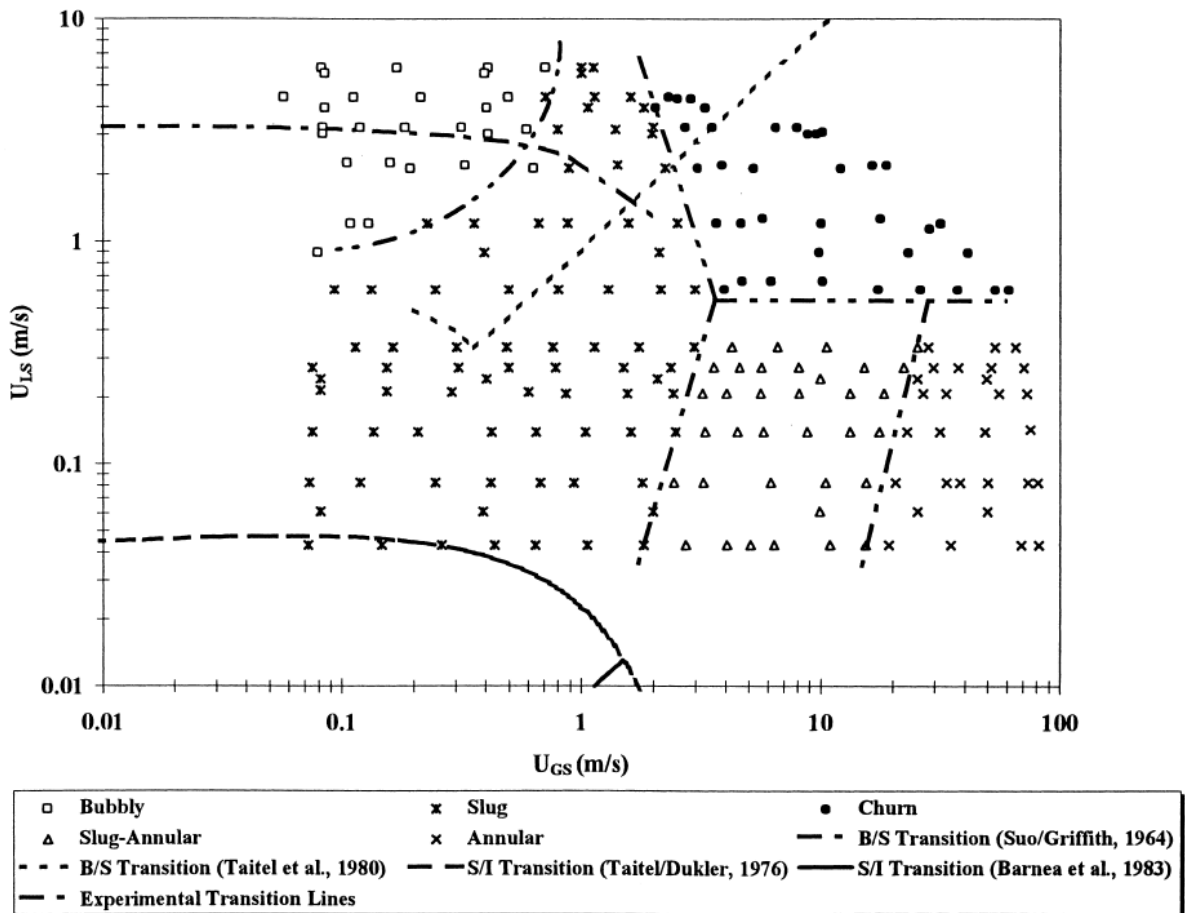


Figure 5.2. Flow regime [44].

In this investigation, a combination of maximizing the film thickness with velocity increases will lead to the development of the first operating limit model for OHPs. The highest recorded power input was 8 kW [45, 46] and a few investigators have attempted to experimentally find the operating limit with refrigerants [47]. The model follows Han and Shikazono's correlation [43] that compares to Taylor's bubble experiment [37]. The effects of tube radius, filling ratio, and tube length will be considered. Different working fluids will be investigated also.

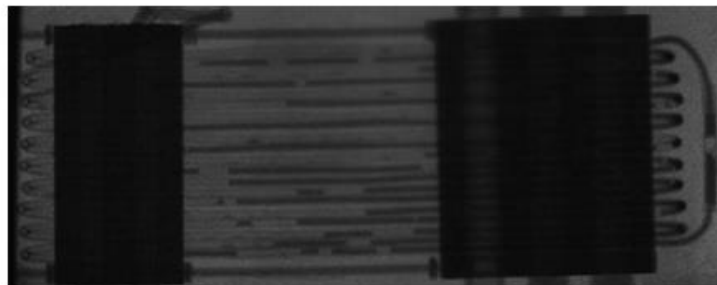
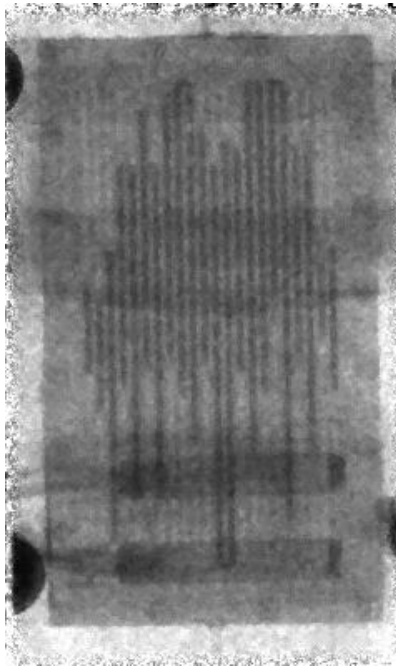


Figure 5.3. Top is a small scale FP-OHP design using neutron radiography [38], Bottom is a much larger 12 turn 3D tubular OHP size [33].

5.2 THEORETICAL MODEL

Taylor bubbles can be visualized as a bubble as seen in Figure 5.4 where a velocity U elongates the bubble length while leaving behind a film of height b as seen in Figure 5.5. Various nondimensional numbers have been used to help characterize the bubble interaction with different phenomena. The key expression is the relationship of film thickness as a function of velocity. From Table 5.1, each nondimensional number compares force ratios that are relevant to the system. In this model, only horizontal channels are considered, therefore, the Froude number and Bond number will not be considered.

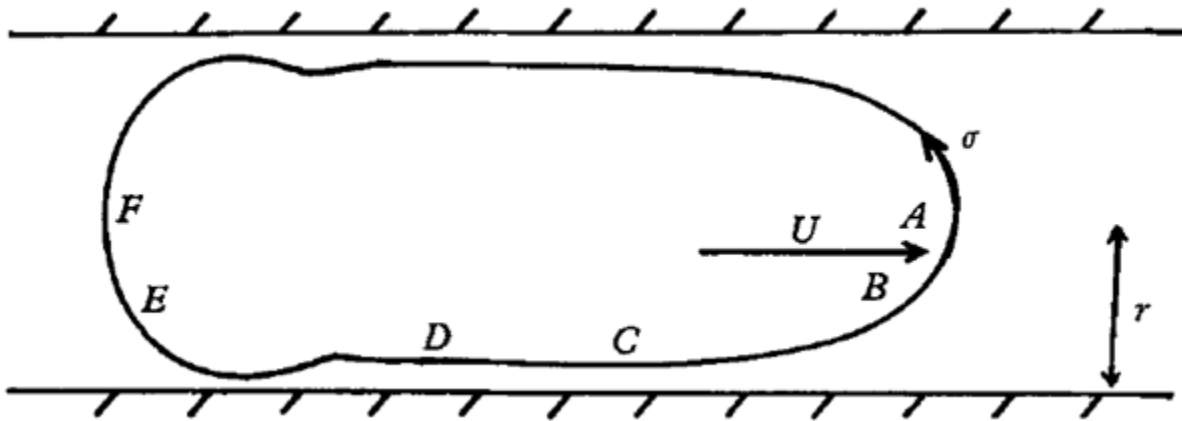


Figure 5.4. Taylor bubble schematic from Bretherton [41].

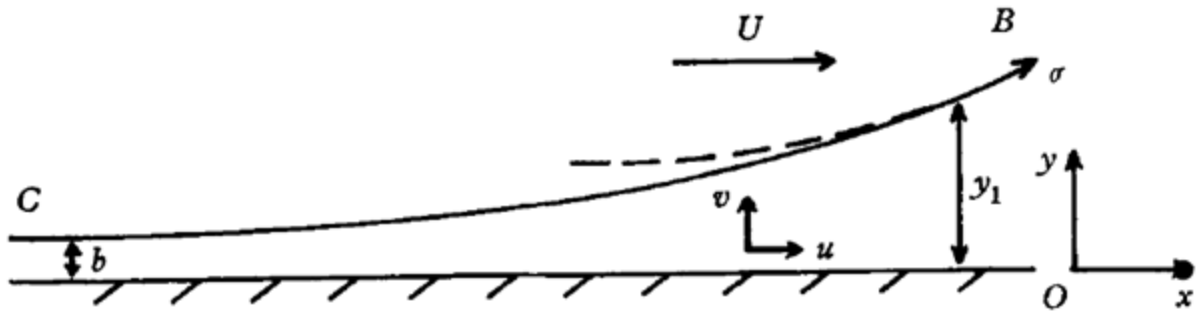


Figure 5.5. Schematic of the thin film region where b is the film thickness [41].

Table 5.1. List of relevant nondimensional numbers.

Name	Relation	Phenomena
Reynolds Number	$\frac{\rho u D}{\mu}$	$\frac{\text{Inertial Force}}{\text{Viscous Force}}$
Froude Number	$\frac{\rho u^2}{\Delta \rho g D}$	$\frac{\text{Inertial Force}}{\text{Gravitational Force}}$
Bond Number	$\frac{\Delta \rho g D^2}{\sigma}$	$\frac{\text{Gravitational Force}}{\text{Surface Tension}}$
Capillary Number	$\frac{\mu u}{\sigma}$	$\frac{\text{Viscous Force}}{\text{Surface Tension}}$
Weber Number	$\rho u^2 D$	$\frac{\text{Inertial Force}}{\text{Surface Tension}}$

Aussillous and Quere [42] proposed an empirical fit of Taylor's experiment as seen in Figure 5.7. Han and Shikazono results comparing working fluid [43].Figure 5.6 as

$$\frac{\delta_0}{D} = \frac{0.67Ca^{\frac{2}{3}}}{1 + 2.5 \times 1.34 Ca^{\frac{2}{3}}} \quad (5.1)$$

With high viscosity fluids such as glycerine, syrup-water, and lubricating oil from Taylor's experiment [37] and found that Capillary number is the only needed factor with no relationship to Reynold's number as shown in Eq. (5.1). When moderately viscous to low viscosity fluids such as water or ethanol are consider, Reynolds number become a factor which should be included. As the liquid film thickness increases as a consequence of the inertial forces, Weber number is considered. A rough relationship is considered by Han and Shikazono as follows

$$\frac{\delta_o}{R} \sim \frac{(Ca)^{\frac{2}{3}}}{(Ca)^{\frac{2}{3}} + 1 + f(Re, Ca) - g(We)} \quad (5.2)$$

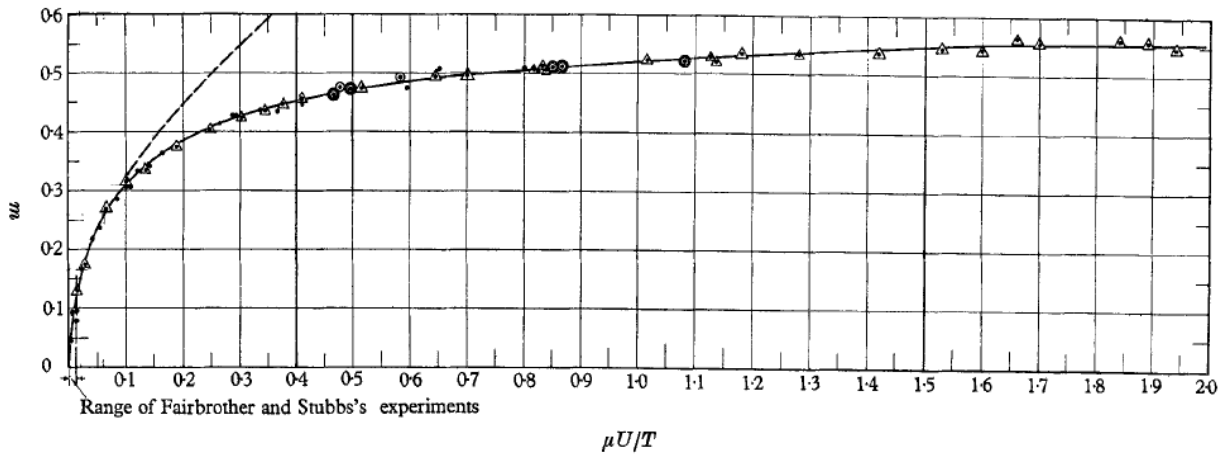


Figure 5.6. Experimental data from Taylor 1961 [37].

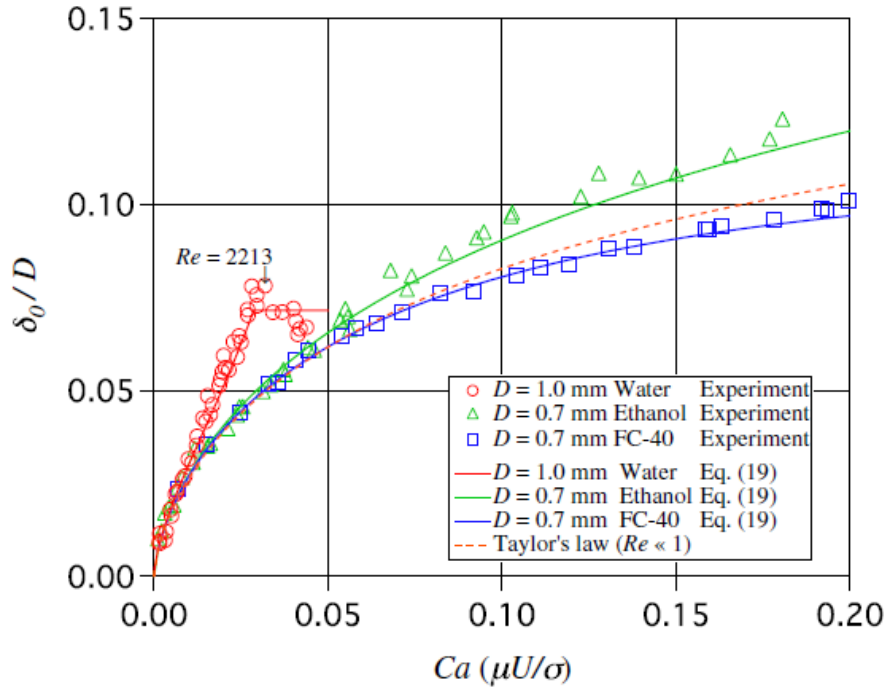


Figure 5.7. Han and Shikazono results comparing working fluid [43].

Han and Shikazono then compared Eq. (5.2) to empirically fit onto the experimental data as seen in Figure 5.7 as

$$\frac{\delta_{max}}{R} = \frac{1.34Ca^{2/3}}{1 + 3.13Ca^{2/3} + 0.54Ca^{0.672}Re^{0.589} - 0.352We^{0.629}} \quad (5.3)$$

Han and Shikazono developed a correlation that encompasses all the nongravitational dimensionless numbers (Reynolds, capillary, Weber) as seen in Table 5.1. Their experiment uses a laser focus displacement meter to measure the film thickness with set velocities comparing diameters of 0.3 mm, 0.5 mm, 0.7 mm, 1.0 mm, and 1.3 mm. Three working fluids of water, ethanol, and FC-40 were compared.

The OHP is effectively a single meandering tube that is composed of many vapor bubbles and liquid slugs. In order to simplify this structure, the meandering tube is unwound into a long singular tube where all the vapor bubbles and liquid slugs become one singular bulk bubble and slug as shown in Fig. 9. The bubble curvature will be a hemispherical cap that scales with the vapor radius.

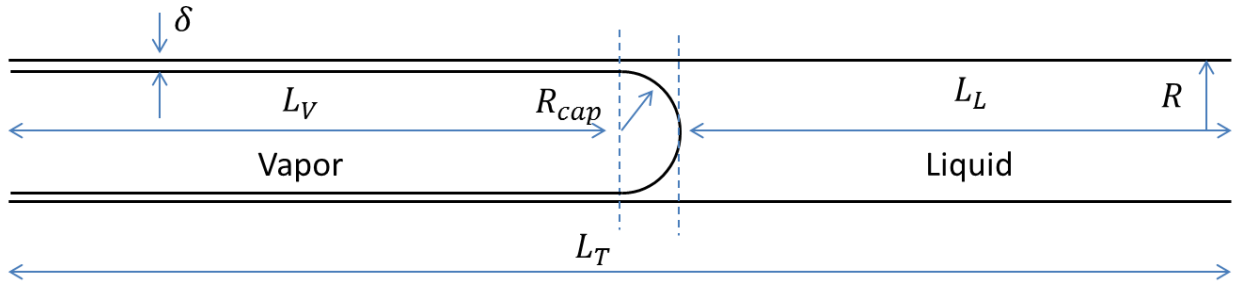


Figure 5.8. Schematic of a typical slug flow with the film thickness in a tube.

From the geometry as shown in Figure 5.8, the liquid and vapor volumes can be found as

$$V_L = L_L \pi R^2 + \left[\pi R^2 (R - \delta) - \frac{2}{3} \pi (R - \delta)^3 \right] + L_V \pi (R^2 - (R - \delta)^2) \quad (5.4)$$

$$V_V = L_V \pi (R - \delta)^2 + \frac{2}{3} \pi (R - \delta)^3 \quad (5.5)$$

where V_L , V_V , L_L , L_V , R , δ are the liquid volume, vapor volume, liquid length, vapor length, tube radius, and film thickness respectively.

For the initial case, the film thickness would not exist as seen from Figure 5.9 since no movement has occurred. Then for $\delta = 0$, Eqs. (5.4) and (5.5) becomes

$$V_L = L_L \pi R^2 + \frac{1}{3} \pi R^3 \quad (5.6)$$

$$V_V = L_V \pi R^2 + \frac{2}{3} \pi R^3. \quad (5.7)$$

This makes sense since when there is no film thickness, only the volumes rely on the tube radius. Notice the hemispherical volume for the bubble cap has been considered also.

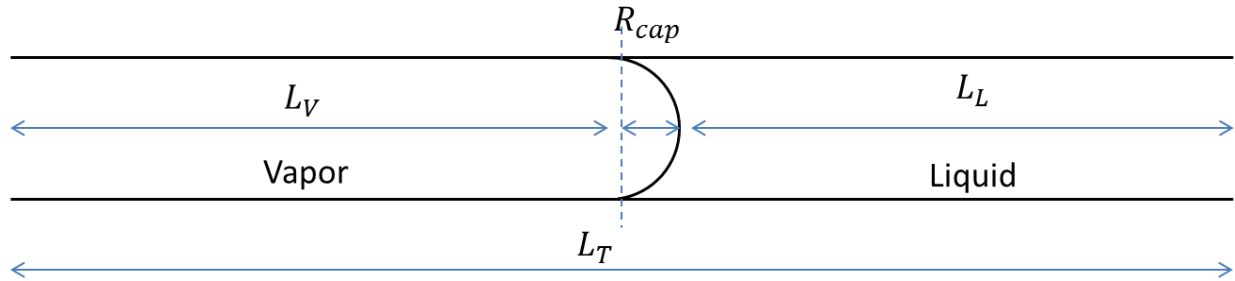


Figure 5.9. Schematic of an initial condition case where there is no movement and no film thickness.

For the case of operating limit, the key assumption is the OHP dry-out during annular flow as seen in Figure 5.10. Therefore the maximum film thickness occurs when the bulk liquid slug length becomes zero as follows

$$V_L = \left[\pi R^2 (R - \delta_{max}) - \frac{2}{3} \pi (R - \delta_{max})^3 \right] + L_V \pi (R^2 - (R - \delta_{max})^2) \quad (5.8)$$

$$V_V = L_V \pi (R - \delta_{max})^2 + \frac{2}{3} \pi (R - \delta_{max})^3 \quad (5.9)$$

The total length for the annular case can be found as

$$L_T = L_V + (R - \delta_{max}). \quad (5.10)$$

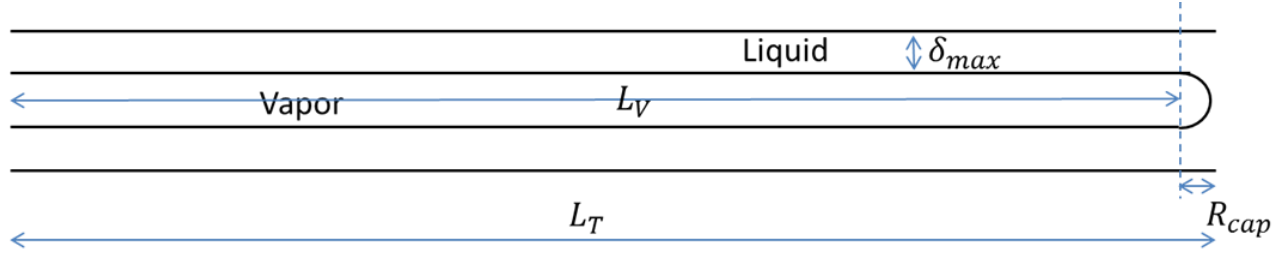


Figure 5.10. Schematic of limiting case where flow is annular.

The bulk vapor and liquid volumes can be related to a set charging or filling ratio as follows

$$\Phi = \frac{V_L}{V_L + V_V} \quad (5.11)$$

Now substitute Eqs. (5.8) and (5.9) into Eq. (5.11) to get

$$\Phi = \frac{\left[\pi R^2(R - \delta_{max}) - \frac{2}{3}\pi(R - \delta_{max})^3 \right] + L_V \pi(R^2 - (R - \delta_{max})^2)}{\left[\pi R^2(R - \delta_{max}) - \frac{2}{3}\pi(R - \delta_{max})^3 \right] + L_V \pi(R^2 - (R - \delta_{max})^2) + L_V \pi(R - \delta_{max})^2 + \frac{2}{3}\pi(R - \delta_{max})^3} \quad (5.12)$$

Rearranging yields

$$\Phi = \frac{R^2(R - \delta_{max}) - \frac{2}{3}(R - \delta_{max})^3 + L_V(R^2) - L_V(R - \delta_{max})^2}{R^2(R - \delta_{max}) + L_V R^2} \quad (5.13)$$

Substituting Eq. (5.10) into Eq. (5.13) produces

$$\Phi = \frac{R^2(R - \delta_{max}) - \frac{2}{3}(R - \delta_{max})^3 + (L_T - (R - \delta_{max}))(R^2) - (L_T - (R - \delta_{max}))(R - \delta_{max})^2}{R^2(R - \delta_{max}) + (L_T - (R - \delta_{max}))R^2} \quad (5.14)$$

Rearranging Eq (5.14) gets

$$(R - \delta_{max})^3 + (-3L_T)(R - \delta_{max})^2 + (0)(R - \delta_{max}) + 3L_TR^2(1 - \Phi) = 0 \quad (5.15)$$

Equation (5.15) is now the same structure as a cubic formula as follows

$$ax^3 + bx^2 + cx + d = 0 \quad (5.16)$$

where

$$a = 1$$

$$b = -3L_T$$

$$c = 0$$

$$d = 3L_TR^2(1 - \Phi)$$

$$x = R - \delta_{max}$$

Three roots exist for Eq. (5.15). A typical scenario consists of one negative, one large positive, and one small positive root. The following equation is used to compare the roots

$$\delta_{max} = R - x \quad (5.17)$$

After comparison, only the small positive root gives a reasonable answer. The negative root gives $\delta_{max} > R$, and the large positive gives a negative δ_{max} which is not possible. The geometric δ_{max} , Eq. (5.17) is then compared with Eq. (5.3) to obtain the maximum velocity, u_{max} where Ca , Re , and We are the capillary, Reynolds, and Weber numbers. The operating limit can then be readily obtained with the following relationship

$$Q_{max} = u_{max}\rho(2\pi R^2)h_{lv} \quad (5.18)$$

where ρ , h_{lv} are the density, latent heat of vaporization. If heat added on the heat pipe reaches the highest, annular flow occurs therefore leading to dryout.

5.3 RESULTS AND DISCUSSION

Figure 5.11 shows the tube radius effect on the operating limit. As shown, as the radius of the tube increases, the film thickness increases. Interestingly in

Figure 5.12, the maximum velocity decreases as the radius increases which means annular flow occurs easier in larger tubes than smaller tubes. Figure 5.13 shows that even if the velocity decreases the increase in radius still raises the operating limit. This effect is due to Eq. (5.18) where there is an R^2 effect from the area.

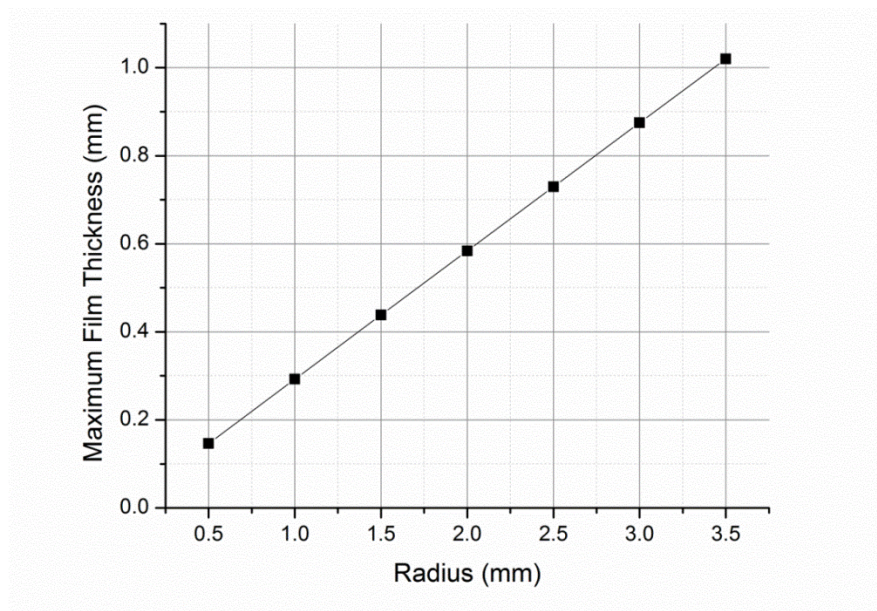


Figure 5.11. Radius effect on the maximum film thickness with water at 100°C, length of 20 cm and charging ratio of 50%.

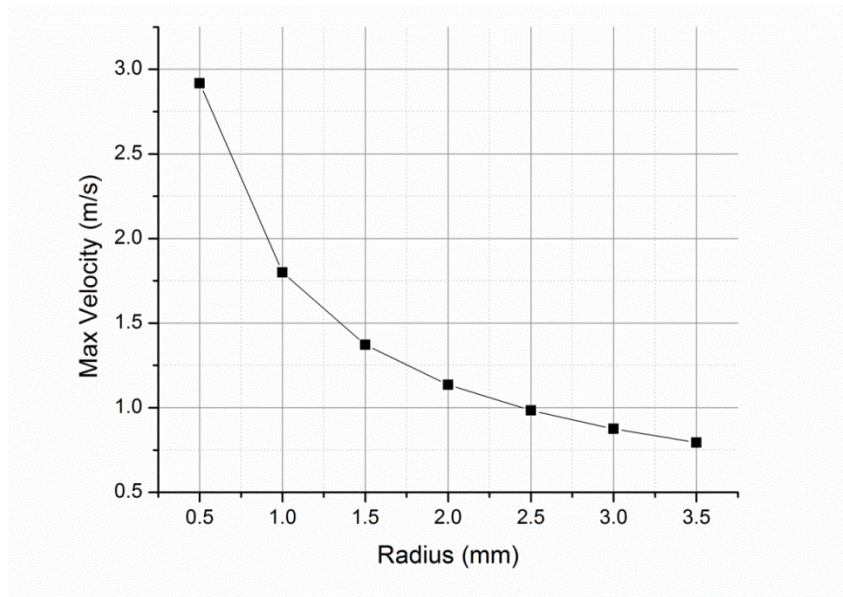


Figure 5.12. Radius effect on the velocity with water at 100°C, length of 20 cm and charging ratio of 50%.

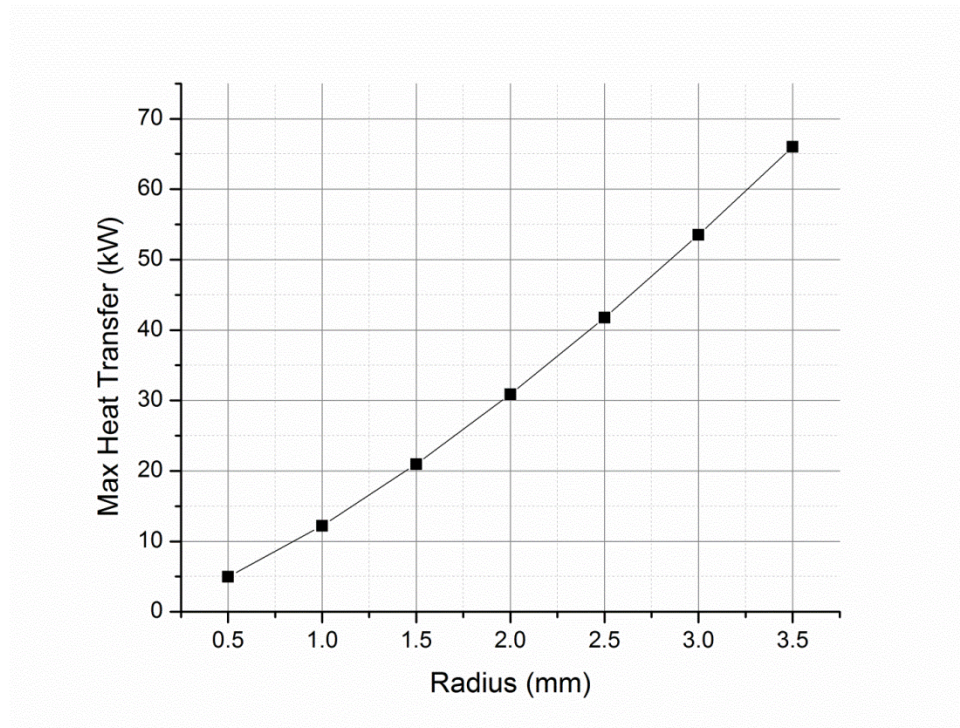


Figure 5.13. Radius effect on the maximum heat transfer rate with water at 100°C, length of 20 cm and charging ratio of 50%.

The charging ratio has a significant effect on the system as seen in Figure 5.14 through Figure 5.16. The film thickness rises as charging ratio rises as seen in Figure 5.14. This is contributed to extra liquid in the system therefore extra film along the tube. The maximum velocity is higher as charging ratio increases as seen in Figure 5.15. This means annular flow has a higher ceiling with higher charging ratios. Figure 5.16 shows the charging ratio effect on the operating limit. At a 1 mm radius tube with length of 20 cm in water, the operating limit goes as high as 9 kW. This is higher than the highest recorded wattage of 8 kW [46].

Figure 5.17 to Figure 5.19 show the length effect. As shown, the length does not affect much of the operating limit. Most likely this is due to no frictional force considerations which is consistent with results presented by Han and Shikazono [43], i.e., there is not much effect on the velocity occurred with different lengths.

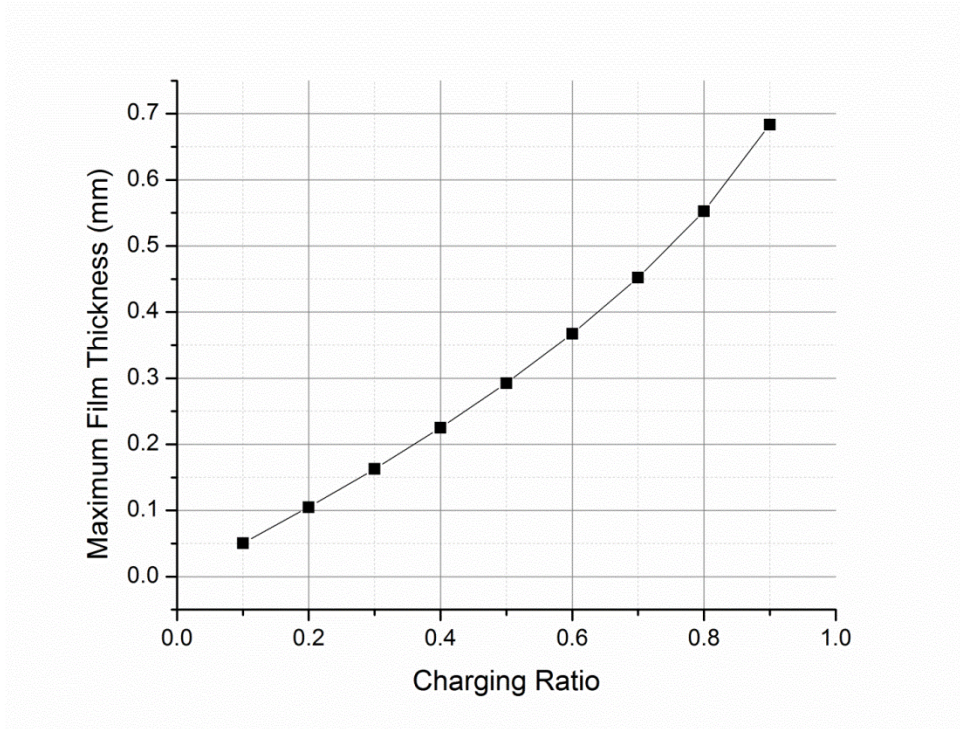


Figure 5.14. Charging ratio effect on the film thickness with water at 100°C, length of 20 cm and radius of 1 mm.

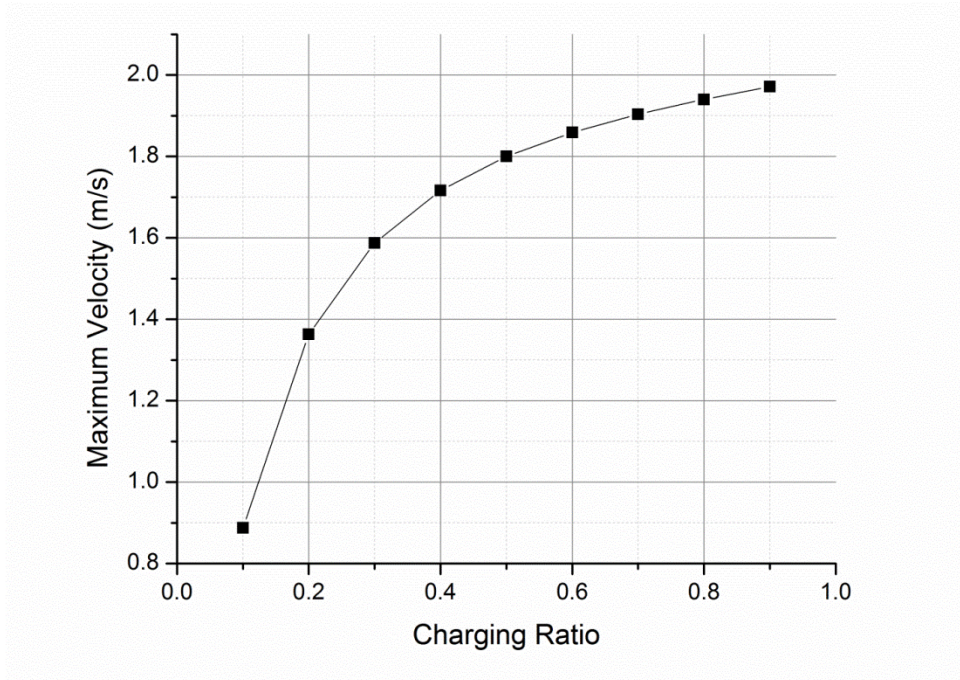


Figure 5.15. Charging ratio effect on velocity with water at 100°C, length of 20 cm and radius of 1 mm.

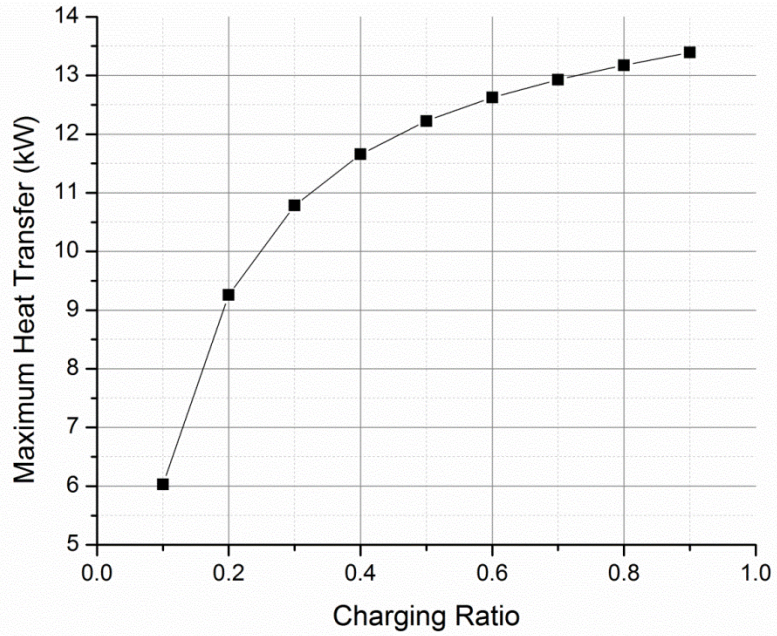


Figure 5.16. Charging ratio effect on the maximum heat transfer rate with water at 100°C, length of 20 cm and radius of 1 mm.

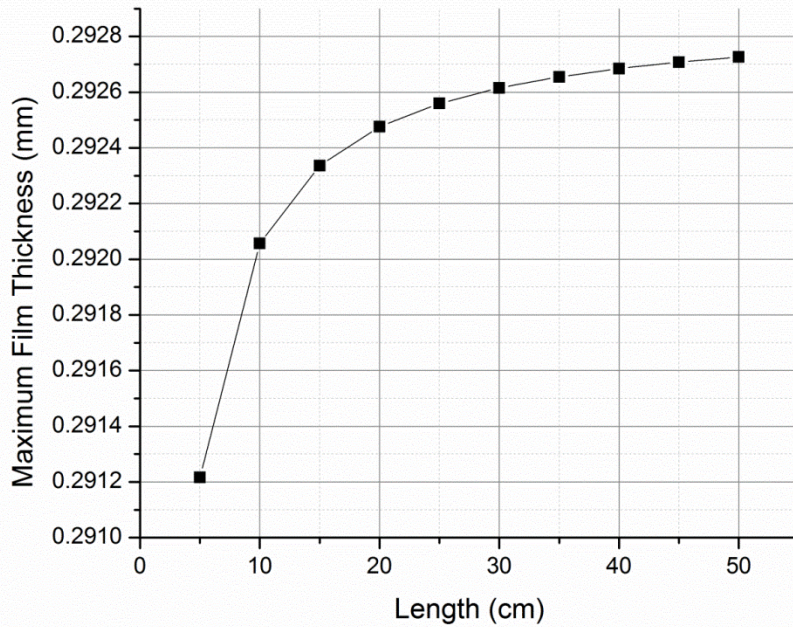


Figure 5.17. Length effect on film thickness with water at 100°C, radius of 1 mm and charging ratio of 50%.

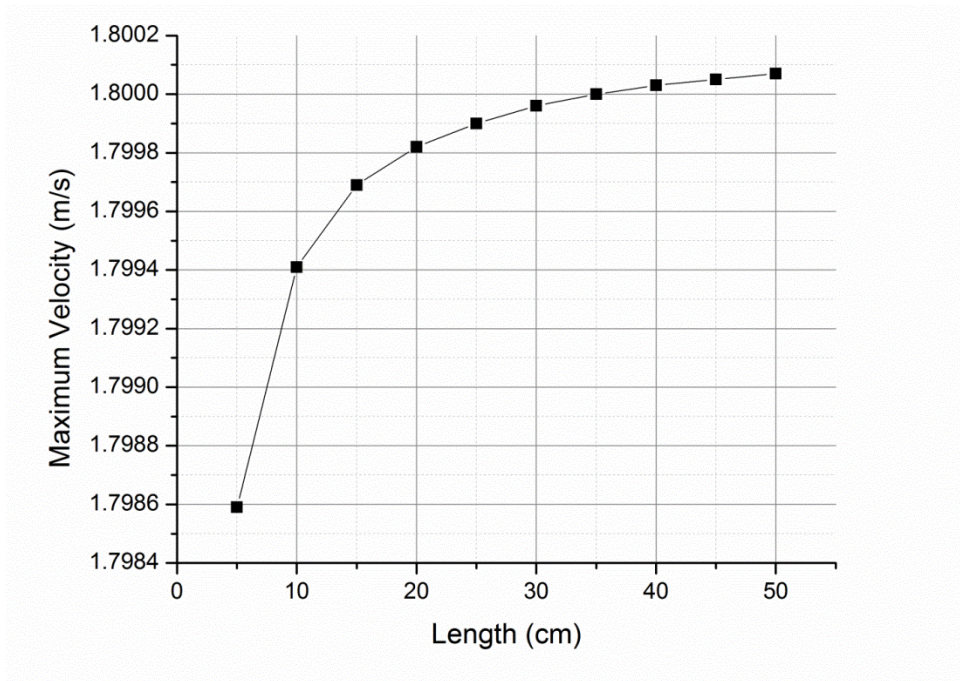


Figure 5.18. Length effect on the velocity with water at 100°C, radius of 1 mm and charging ratio of 50%.

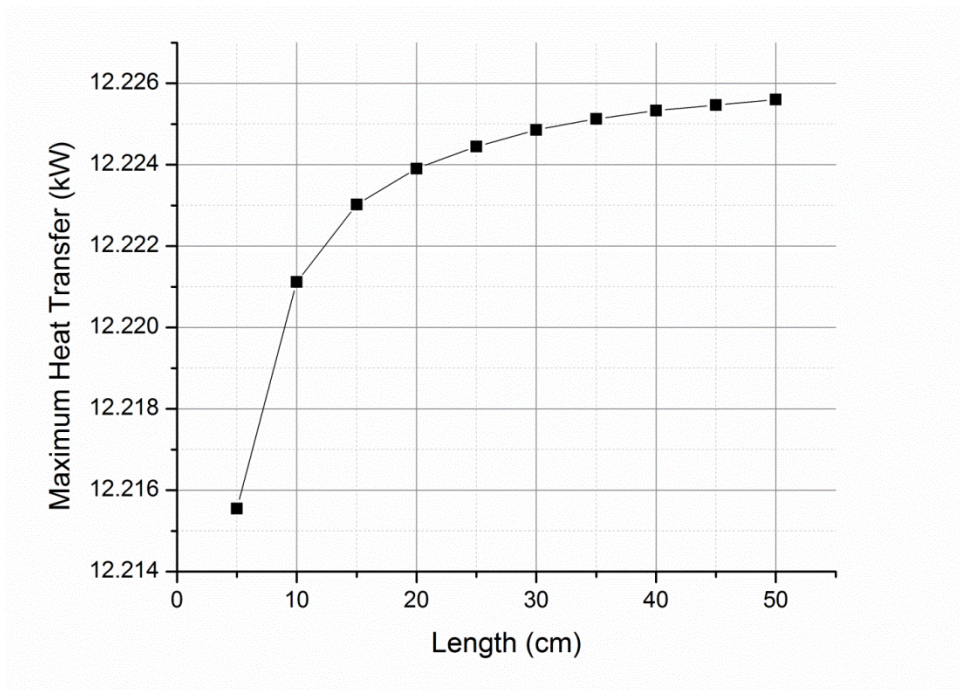


Figure 5.19. Length effect on the maximum heat transfer rate with water at 100°C, radius of 1 mm and charging ratio of 50%.

The effect of working fluid is investigated. Acetone's results are shown in Figure 5.20, and R123 in Figure 5.21. Figure 5.22 shows a comparison of the three working fluids. Smoot and Ma [46] reported a maximum heat input of 8000 W, however; it should be noted that the results reported by Smoot and Ma [46] is due to the limitation of the heater. The current model predicts a maximum heat input is closer to around ~12 kW of power which means there is still more room for improvement.

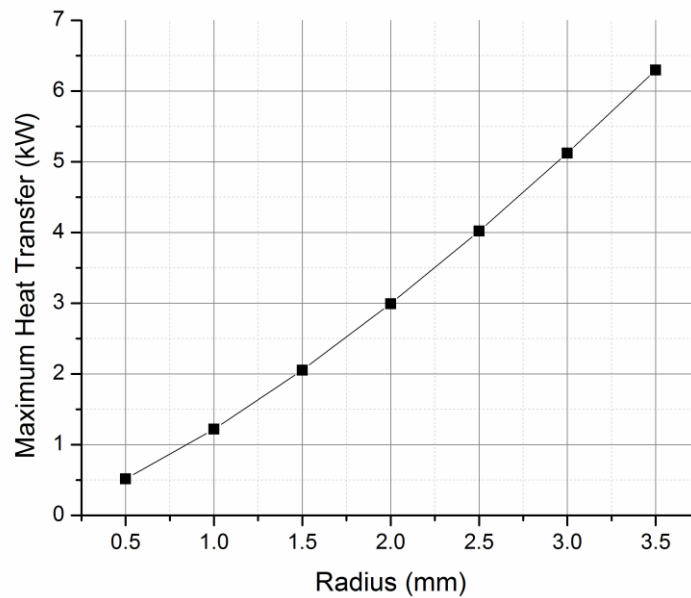


Figure 5.20. Acetone as working fluid at 100°C, length of 20 cm, and charging ratio of 50%.

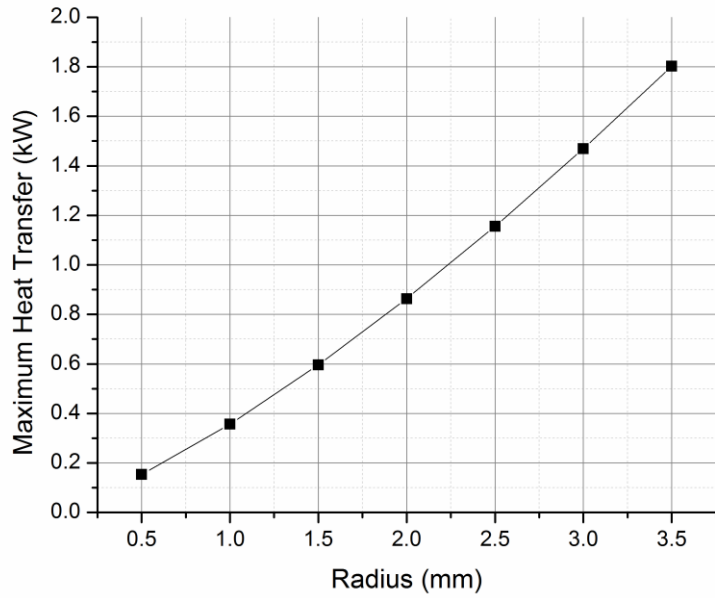


Figure 5.21. Refrigerant 123 as working fluid at 100°C, length of 20 cm, and charging ratio of 50%.

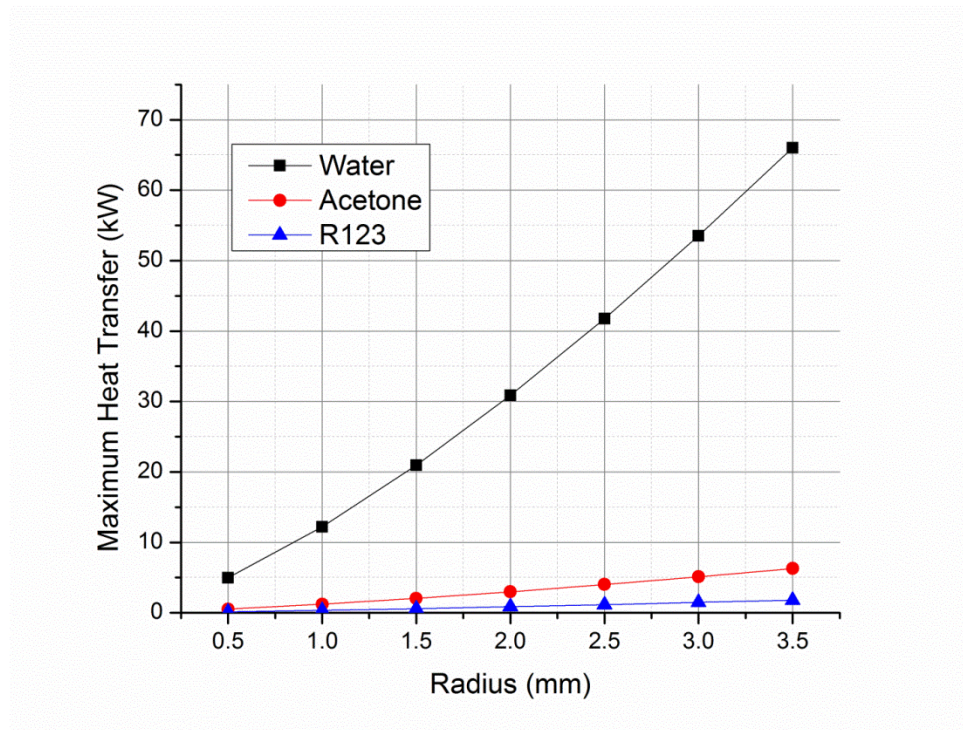


Figure 5.22. Comparison of three different working fluids at 100°C, length of 20 cm, and charging ratio of 50%.

5.4 SUMMARY

A theoretical model for the operating limit of the OHP has been developed. The maximum operating limit for a water system with a charging ratio of 50%, length of 20 cm and radius of 1 mm is 12 kW. The radius and charging ratio have significant effects on the operating limit while the length effect is insignificant. Working fluids of water, acetone, and R123 were considered and water has a much higher operating limit than acetone or R123.

6 CONTACT ANGLE EFFECT ON THE OSCILLATING MOTION OF AN OSCILLATING HEAT PIPE

6.1 INTRODUCTION

The principle operation starts with a two-phase liquid plug/vapor slug formation within partially evacuated small diameter channels. The channel meanders bending back and forth throughout itself and eventually connecting back to beginning. Heat is then added in the evaporating section and removed in the condensing section. The temperature difference between these two sections causes a pressure drop which produces the driving force necessary for creating the oscillating motion unique to OHPs. Many different models have been conducted to predict the internal OHP mechanisms [48-53] but the most interesting conclusion of an OHP lies in the fact that the performance gets better as heat input increases. However studies have not considered the effect of contact angle on the oscillating motion.

The capillary effect on static contact angle was first developed in 1921 by Washburn [54] but the dynamic contact angle has not been observed. In 1969, Blake [55] based the dynamic contact angle on molecular kinetics (atom to atom interactions). Afterwards, Dussan [56], Hoffman [57, 58], and Cox [59] used the hydrodynamic theory (viscosity based) to describe the dynamic contact angle phenomenon. A more radical numerical version developed by Shikmurzaev [60-62] is more complete but the solution is not closed form. All the models stated are rather complicated and but an empirical fit developed by Joos et al. [63] is the simplest compared to all. A study comparing the different models by Popescu et al. [64] showed that the hydrodynamic, molecular kinetics, and the empirical models are rather close within the laminar

flow regime and low velocities. This provides the basis of relating the contact angle to the flow inside the pipes.

The objective of this study is to develop a model for predicting how contact angle can affect the oscillating motion in an OHP. The model will consider all forces added on the liquid plugs including the frictional force, driving force, inertial force, and an additional force due to surface tension that relates to the Laplace-Young equation. Using this model, the effects of static contact angle on the position and the velocity will be investigated. Then the velocity effect on the dynamic contact angle will be studied. The results will provide a better look into the trends and characteristics of the pulsating motion in oscillating heat pipes.

6.2 THEORETICAL MODEL

The OHP model proposed by Ma et al. [48, 49] will be the basis for the further refined inclusion of the contact angle effect. First consider the liquid plug and vapor bubbles shown in Figure 6.1 along with the following fundamental Newton's law, i.e.,

$$\Sigma F = m \left(\frac{d^2 x}{dt^2} \right) \quad (6.1)$$

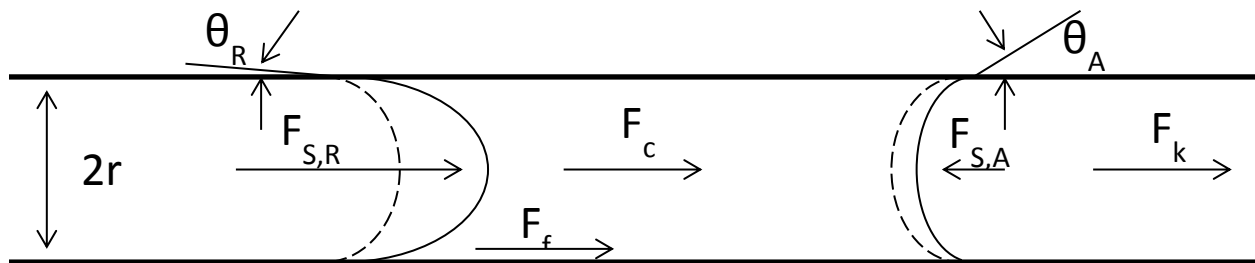


Figure 6.1. Schematic of liquid plug (the dotted line is the equilibrium angle while the solid lines near $F_{S,R}$, $F_{S,A}$ are the receding and advancing contact angle forces when there is a movement).

Ma et al[49] consider the summation of three forces: the inertial force (F_c), friction force (F_f) and elastic restoring force (F_k) being equal to the thermally driven force ($F(t)$) as

$$F_c + F_f + F_k = F(t) \quad (6.2)$$

However, the surface tension force was not considered. Considering the surface tension, Eq. (6.2) becomes

$$F_c + F_f + F_s + F_k = F(t) \quad (6.3)$$

with F_s being the surface tension.

The inertial force is due to the mass of the vapor/liquid accelerating, i.e.,

$$F_c = (L_l \rho_l + L_v \rho_v) A \frac{d^2 x}{dt^2} \quad (6.4)$$

where the subscript l and v denote liquid slug and vapor plug respectively, and A means the cross sectional area. The friction force arises due to the interaction between the vapor/liquid and the wall of the tube. This creates a pressure gradient along the x-direction which can be evaluated as

$$\frac{dp_f}{dx} = -\frac{4\tau_s}{D_h} \quad (6.5)$$

where τ_s is the shear stress between the interface of liquid/slug and pipe wall and D_h being the hydraulic diameter. Considering the friction factor and Reynolds number, the force due to friction factor can be expressed as

$$F_f = A \left[f_l Re_l \left(\frac{\mu_l L_l}{2D_h^2} \right) + f_v Re_v \left(\frac{\mu_v L_v}{2D_h^2} \right) \right] \quad (6.6)$$

where f , Re , μ , L are the friction factor, Reynolds number, viscosity, and total length respectively and the subscripts l and v stand for liquid and vapor. In addition to the friction factor, the contact angle effect is also a damping force since it also affects the liquid/vapor interaction along the wall, which can be expressed as

$$F_s = F_{s,R} - F_{s,A} \quad (6.7)$$

where $F_{s,R}$ is the receding surface tension force along with a counteracting advancing surface tension force, $F_{s,A}$. Considering the receding and advancing contact angles, Eq. (6.7) can be found as

$$F_s = \frac{A\sigma}{r} (\cos(\theta_R) - \cos(\theta_A)). \quad (6.8)$$

It is assumed that θ_R is zero for a perfectly wetted receding section which allows for Eq. (6.7) to be rewritten as

$$F_s = \frac{A\sigma}{r} (1 - \cos(\theta_A)). \quad (6.9)$$

Since the advancing contact angle, θ_A , changes with velocity, a relationship needs to be found. Joos et al. [63] found that this advancing contact angle, θ_A , or called dynamic contact angle, θ_D can be expressed as

$$\cos\theta_D = \cos\theta_E - 2(1 + \cos\theta_E)(Ca)^{0.5} \quad (6.10)$$

where θ_D is the dynamic contact angle, θ_E is the equilibrium or static contact angle, and Ca is the capillary number, i.e.,

$$Ca = \frac{\mu V}{\sigma} \quad (6.11)$$

By combining Eqs. (6.7), (6.8), (6.9), and (6.10), the expression due the surface tension can be found as

$$F_s = \frac{A\sigma}{r} \left(1 - \left(\cos\theta_E - 2(1 + \cos(\theta_E)) \left(\frac{\mu V}{\sigma} \right)^{0.5} \right) \right) \quad (6.12)$$

The elastic restoring force is due to the vapor bubble contracting and expanding similar to a spring. An ideal gas assumption can be made due to the volume being constant throughout time. Since the x is small compared to L_v , a linear assumption has been made and the elastic restoring force is calculated by

$$F_k = \frac{A\rho_v RT}{L_v} x \quad (6.13)$$

The driving force is due the pressure difference between the evaporator and condenser, which can be found by the Clapeyron equation, i.e.,

$$p_e = p_0 \exp\left(\frac{h_{lv}(T_e - T_0)}{RT_e T_0}\right) \quad (6.14)$$

where the reference temperature and pressure are T_0 and p_0 respectively. T_e is the evaporator temperature along with latent heat of vaporization (h_{lv}) and gas constant (R). As one takes pressure difference between the evaporator and condenser section of the heat pipe, i.e.,

$$\Delta p = p_e - p_c = p_c \left[\exp\left(\frac{h_{lv}(T_e - T_c)}{RT_e T_c}\right) - 1 \right] \quad (6.15)$$

This is then expanded using Taylor's series ignoring the higher order terms and the following is obtained

$$\Delta p = (T_e - T_c) \left(\frac{h_{lv} \rho_{v,c}}{T_e} \right) \quad (6.16)$$

The temperature difference between the evaporator and condenser causes the expansion and compression of the vapor plugs trapped between the liquid slugs, thus creating an oscillating motion expressed as

$$\Delta T = \left(\frac{\Delta T_{max} - \Delta T_{min}}{2} \right) [1 + \cos(\omega t)] \quad (6.17)$$

where the ΔT_{max} and ΔT_{min} are the max and min temperature differences between the condensing and evaporating sections. The system oscillating frequency is ω . substituting Eq. (6.17) into Eq. (6.16), the driving force can be found as

$$F(t) = \frac{Ah_{f,g}\rho_{v,c}}{T_e} \left(\frac{\Delta T_{max} - \Delta T_{min}}{2} \right) [1 + \cos(\omega t)] \quad (6.18)$$

Substituting Eqs. (6.4), (6.6), (6.12), (6.13) and (6.18) into Eq. (6.3) yields

$$\begin{aligned} (L_l \rho_l + L_v \rho_v) A \frac{d^2 x}{dt^2} + \left[f_l Re_l \left(\frac{\mu_l L_l}{2D_h^2} \right) + f_v Re_v \left(\frac{\mu_v L_v}{2D_h^2} \right) \right] A \frac{dx}{dt} + \frac{A\sigma}{r} (1 \\ - \left(\cos \theta_E - 2(1 + \cos(\theta_E)) \left(\frac{\mu}{\sigma} \frac{dx}{dt} \right)^{0.5} \right) + \frac{A\rho_v RT}{L_v} x \\ = \frac{Ah_{f,g}\rho_{v,c}}{T_e} \left(\frac{\Delta T_{max} - \Delta T_{min}}{2} \right) [1 + \cos(\omega t)] \end{aligned} \quad (6.19)$$

With the additional surface tension force, a square root velocity has made this system solvable by numerical method. As the velocity is obtained from the model the dynamic contact angle can be calculated by

$$\theta_D = \arccos(\cos \theta_E - 2(1 + \cos \theta_E)(Ca)^{0.5}). \quad (6.20)$$

6.3 RESULTS

With the model used in the theoretical analysis, the effects of static contact angle on the oscillating motion and velocity can be found. The basic parameters used are water properties at 40°C for properties such as surface tension, density, dynamic viscosity, and latent heat. The length, charging ratio, diameter, operating temperature and temperature difference, are $L = 25\text{ cm}$, $\Phi = 50\%$, $D = 1.0\text{ mm}$, $T_e = 40^{\circ}\text{C}$, and $\Delta T = 3^{\circ}\text{C}$, respectively.

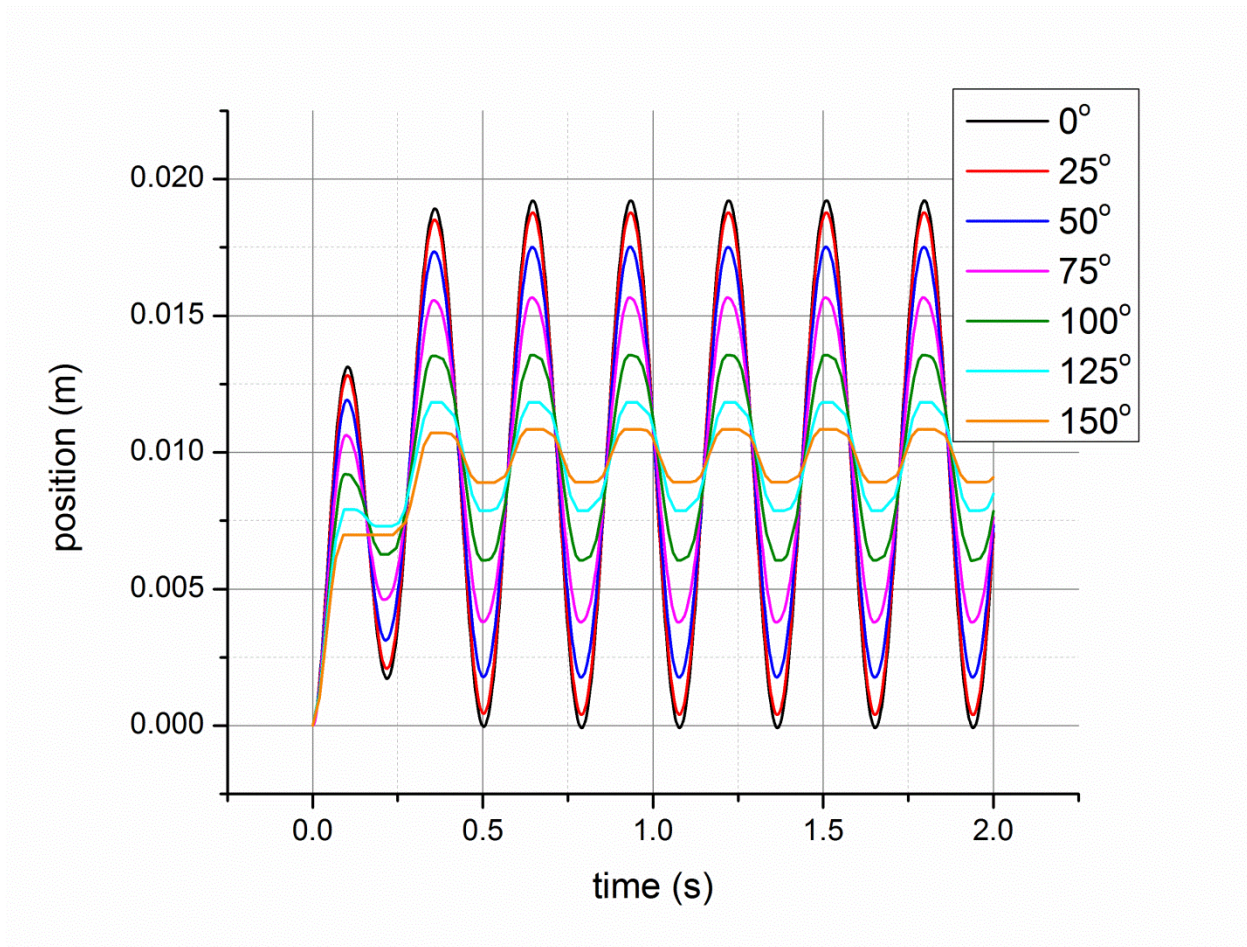


Figure 6.2. Position with various contact angles (Water is the working fluid with the following parameters: $L=25\text{mm}$, $D=1\text{mm}$, $\phi=50\%$, $T_e=40^{\circ}\text{C}$, $\Delta T=3^{\circ}\text{C}$).

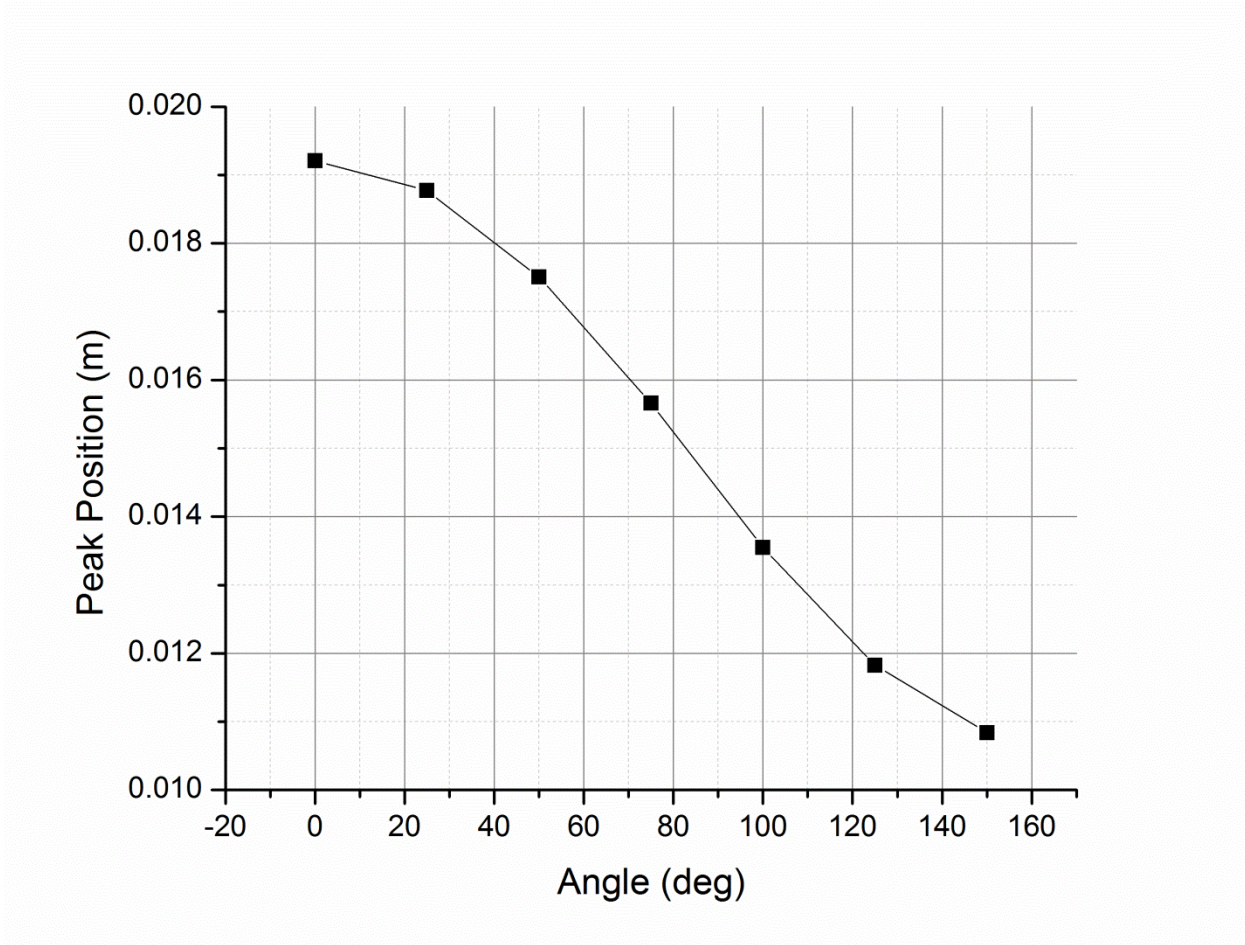


Figure 6.3. Peak Position as a function of contact angle (working fluid is water).

A comparison of the slug position as a function of time has been plotted in Figure 6.2. The multiple lines that appear show the effect of contact angle on the oscillating position of the slug. As the contact angle increases which means a more hydrophobic surface, the maximum distance the slug oscillates will be decreased. Figure 6.3 shows contact angle effect on the peak oscillation position of the slug. The effect of contact angle from a superhydrophobic angle of 150° compared to a superhydrophilic angle of 0° is about an order of magnitude decrease in peak position. This means a hydrophobic condition will decrease oscillations while hydrophilic condition will increase oscillations.

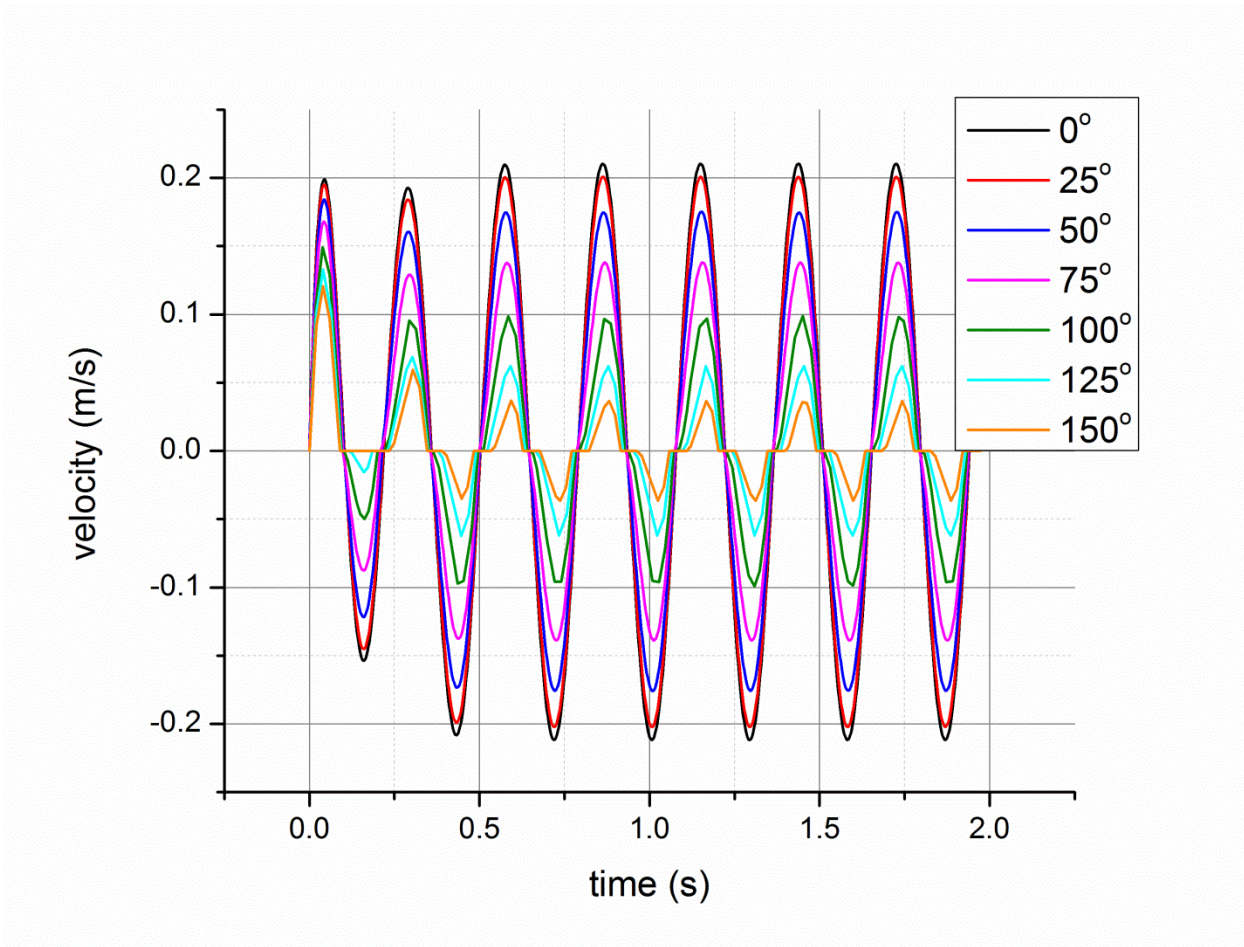


Figure 6.4. Velocity with various contact angles (water is the working fluid with the following parameters: $L=25\text{mm}$, $D=1\text{mm}$, $\phi=50\%$, $T_e=40^\circ\text{C}$, $\Delta T=3^\circ\text{C}$).

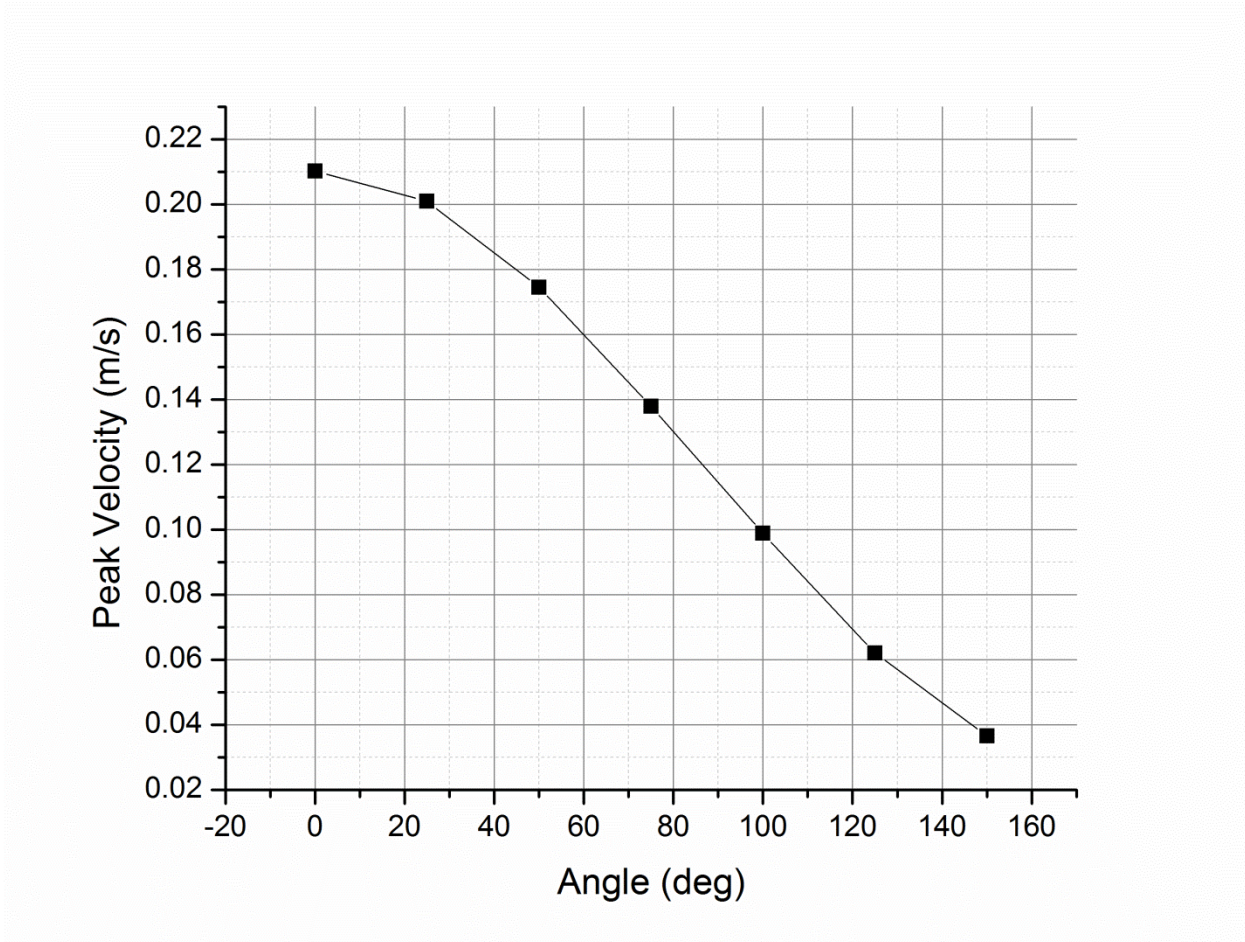


Figure 6.5. Peak velocity as a function of contact angle.

A comparison of the velocity of the slug is compared to the oscillating time frame as seen in Figure 6.5. A similar behavior of high contact angle has a slowing effect on the velocity while a low contact angle has a velocity increase. In Figure 6.5 the peak velocity shows a ~5x decrease in speed from a contact angle of 0° to 150°. This means a hydrophobic surface causes slower velocities which leads to slower movements of the slug that ultimately leads to less available convection heat transfer from the slug to condenser end.

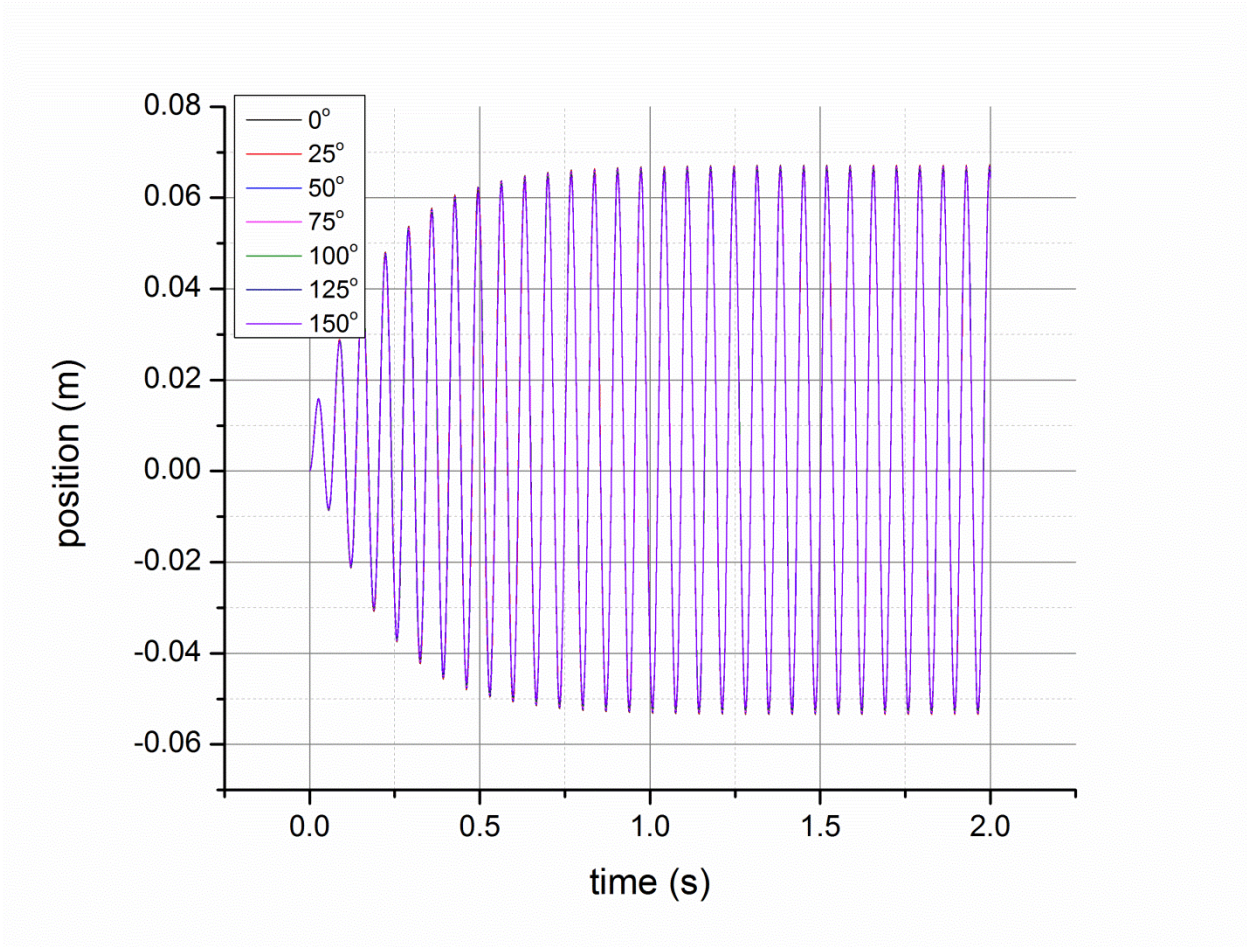


Figure 6.6. Position effect from contact angle (acetone is working fluid change with parameters: $L=25\text{mm}$, $D=1\text{mm}$, $\phi=50\%$, $T_e=60^\circ\text{C}$, $\Delta T=3^\circ\text{C}$).

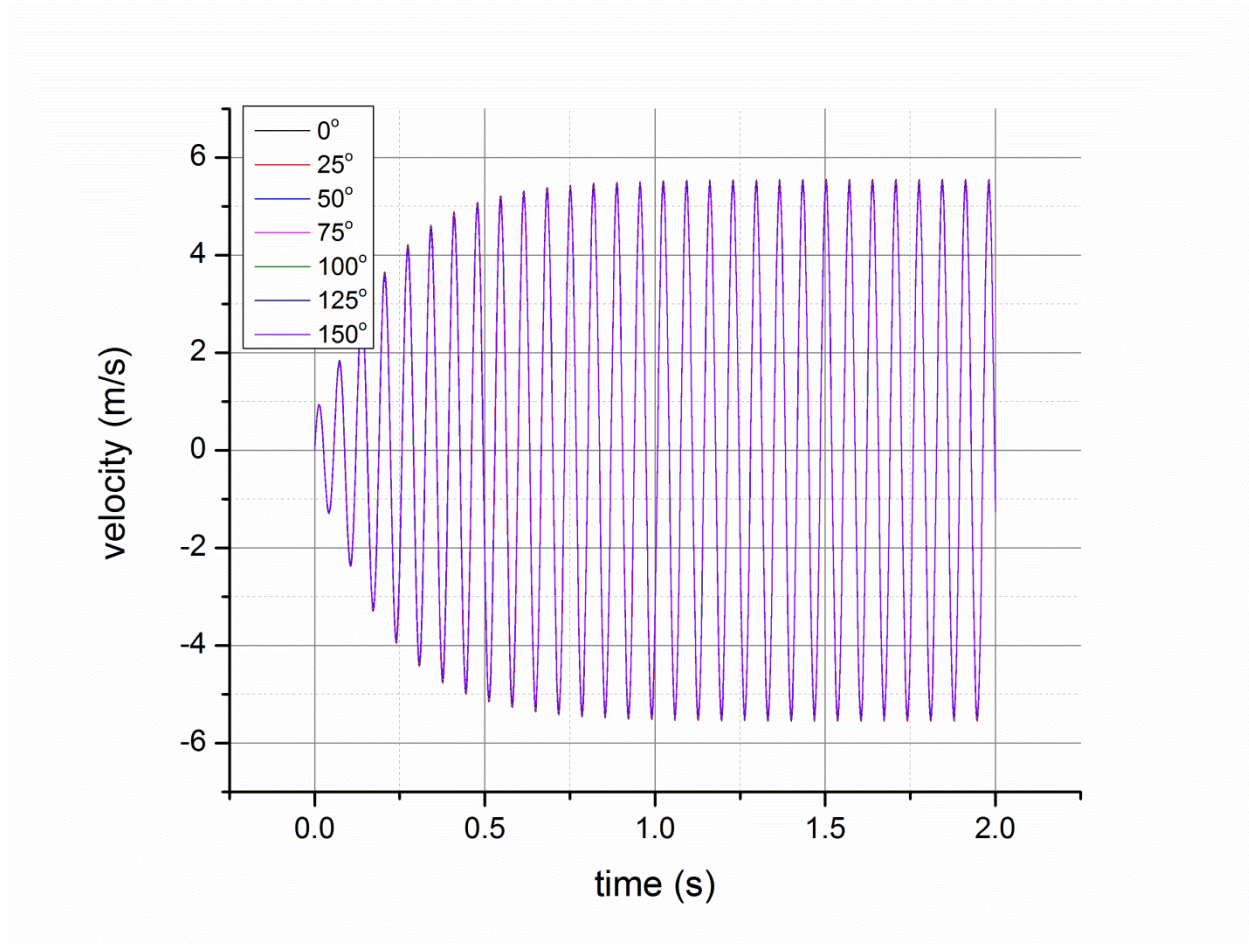


Figure 6.7. Velocity effect from contact angle (acetone is working fluid change with parameters: $L=25\text{mm}$, $D=1\text{mm}$, $\phi=50\%$, $T_e=60^\circ\text{C}$, $\Delta T=3^\circ\text{C}$).

Acetone is another common working fluid studied in this model. In Figure 6.6 and Figure 6.7 the effect of contact angle on the slug position and velocity respectively are shown. There seems to be very little effect on the peak position and velocity for acetone. Acetone wets the surface of most material very well. This model shows that trying to change the contact angle of acetone may not be useful for performance.

6.4 SUMMARY

A mathematical model of the contact angle effect on oscillating motion has been developed. The changes in static contact angle have significant effects on oscillating motion and velocity with as much as an order of magnitude difference in peak slug position from a contact angle of 0° to 150° . The advancing contact angle can now be predicted with variance to time. This model demonstrates that the minimum contact angle or hydrophilic surface will have the highest level of oscillations as compared to a high contact angle or hydrophobic surface which causes an oscillation with low amplitudes.

7 CONCLUSIONS

With the localized heat flux projected to be over 10 MW/m² with powers exceeding 300 W, the current low-cost thermal solutions are limited in their ability to remove the heat with high density. The performance of a FP-OHP selectively treated with CuO nanostructures can far exceed a similar nontreated FP-OHP in this study and provides a promising novel approach for thermal solutions. Nanostructures in the evaporator improved thermal performance over the whole heat input range studied once fluid motions begin. In contrast, nanostructures in the condenser initiated oscillating motion and a corresponding thermal performance improvement at a lower heat input. However, the thermal performance improvement disappeared at higher heat input, which corresponds to the nanostructures being covered by the liquid phase and thus presumably not being able to contribute to enhanced vapor condensation. However after a 1.5 year repetition of the experiment performance is still better than the original control in some areas but deterioration is expected. The interesting component is the close trend following Ma et al. 2006 experiment done with nanofluids. This suggests there is a strong correlation between nanofluids and surface treatments. The reasoning for the strong correlation is due to the nanofluid deposition onto the surface of the internal channels causing changes in the wettability of the OHP which alters beneficially the performance.

Applications that require better thermal performance but emphasize strict temperature variance control may find a promising solution in the hybrid FP-OHP. The hydrophilic/hydrophobic configurations in evaporator and condenser and then vice versa seem to have no advantage over each other in terms of thermal performance and temperature uniformity. The overall thermal performance of the hybrid FP-OHPs seem to be about 15%

worse, but has much better oscillation amplitude compared to the untreated FP-OHP. The mechanism is most likely linked to a contact angle component that can be modeled.

A theoretical model for the operating limit of the OHP has been developed once it has been determined that superhydrophilic surfaces generate better performance. The maximum operating limit for a water system with a charging ratio of 50%, length of 20 cm and radius of 1 mm is 12 kW. The radius and charging ratio have significant effects on the operating limit while the length effect is insignificant. Working fluids of water, acetone, and R123 were considered and water has a much higher operating limit than acetone or R123.

A mathematical model of the contact angle effect on oscillating motion has been developed to compare the results found from the hybrid OHP system that encompasses the hydrophilic and hydrophobic surfaces in the OHP channels. The changes in static contact angle have significant effects on oscillating motion and velocity with as much as an order of magnitude difference in peak slug position from a contact angle of 0° to 150°. The advancing contact angle can now be predicted with variance to time. This model demonstrates that the minimum contact angle or hydrophilic surface will have the highest level of oscillations as compared to a high contact angle or hydrophobic surface which causes a very low amount of oscillation. This model is indirectly proven from the hybrid OHP experiment which experienced lower amplitudes when hydrophobic surfaces were introduced versus non-treated surfaces.

In conclusion, multiple evidence have been shown to support the fact that the surface alteration of the internal channels in the OHP can significantly alter performance whether the goal is to decrease the temperature difference or lower the oscillating amplitude. These studies also show that the nanofluid performance increase in the OHPs is attributed to the

enhancement of the surface of the channels especially since the nanofluid that performed the best is diamond nanoparticles which are naturally hydrophilic. This further supports the fact that an upper operating limit to the OHP is only approached with maximum hydrophilicity. Therefore further research is necessary to investigate smart placement of hybrid OHP nanostructures to further optimize and control the desired performance metrics.

8 REFERENCES

- [1] Perkins, L. P. a. B., W.E., 1982, "Improvements in devices for the diffusion or transference of heat,"United Kingdom.
- [2] Gaugler, R. S., 1942, "Heat transfer device,"United States.
- [3] Grover, G. M., Cotter, T.P., and Erickson, G.F., 1964, "Structures of very high thermal conductance," Journal of Applied Physics, 35, pp. 1990-1991.
- [4] Akachi, H., 1990, "Structure of a heat pipe," Actronics Kabushiki Kaisha, United States.
- [5] Akachi, H., 1993, "Structure of micro-heat pipe," Actronics Kabushiki Kaisha, United States.
- [6] Lin, Y. H., Kang, S. W., and Chen, H. L., 2008, "Effect of Silver Nano-Fluid on Pulsating Heat Pipe Thermal Performance," Applied Thermal Engineering, 28(11-12), pp. 1312-1317
- [7] Ma, H. B., Wilson, C., Yu, Q., Park, K., Choi, U.S., and Tirumala, M., 2006, "An experimental investigation of heat transport capability in a nanofluid oscillating heat pipe," Journal of Heat Transfer, 128, pp. 1213-1216.
- [8] Ma, H. B., Wilson, C., Borgmeyer, B., Park, K., Yu, Q., Choi, S. U. S., and Tirumala, M., 2006, "Effect of Nanofluid on the Heat Transport Capability in an Oscillating Heat Pipe," Applied Physics Letters, 88(14), pp. 143116-143111 - 143116-143113.
- [9] Qu, J., Wu, H., and Cheng, P., 2010, "Thermal performance of an oscillating heat pipe with Al₂O₃-water nanofluids," International Communications in Heat and Mass Transfer, 37, pp. 111-115.
- [10] Qu, J., and Wu, H., 2011, "Thermal Performance Comparison of Oscillating Heat Pipes with SiO₂/Water and Al₂O₃/Water Nanofluids," International Journal of Thermal Sciences, 50(10), pp. 1954-1962
- [11] Ji, Y., Xu, C., Ma, H., and Pan, X., 2013, "An experimental investigation of the heat transfer performance of an oscillating heat pipe with copper oxide (CuO) microstructure layer on the inner surface," Journal of Heat Transfer, 135(7), pp. 074504-074507.

- [12] Ji, Y., Chen, H., Ma, X., Ma, H.B., Kim, Y.J., and Yu, Q., 2012, "Hydrophobic surface effect on heat transfer performance in an oscillating heat pipe," *Journal of Heat Transfer*, 134(7), pp. 74502-74505.
- [13] Slack, G. A., 1972, "Nonmetallic crystals with high thermal conductivity," General Electric, Schenectady, NY.
- [14] Borom, M. P., Slack, G.A., and Szymaszek, J.W., 1972, "Thermal conductivity of commercial aluminum nitride," General Electric, Schenectady, NY.
- [15] Richerson, D. W., 1982, *Modern Ceramic Engineering: Properties, Processing and Use in Design*, Marcel Dekker Inc., New York.
- [16] Rahaman, M. N., 2007, *Ceramic Processing*, Taylor and Francis, New York.
- [17] Callister, W. D., 2007, *Material Science and Engineering: An Introduction*, John Wiley and Sons, Inc, New York.
- [18] 2008, "Beryllium Oxide," MSDS.
- [19] De Baranda, P. S., Knudsen, A.K., and Ruh, E., 1994, "Effect of yttria on the thermal conductivity of aluminum nitride," *Journal of American Ceramics Society*, 77(7), pp. 1946-1950.
- [20] Molisani, A. L., Goldenstein, H., Cruz, A.C., Bressiani, A.H.A., Dutra, J.C., Manholetti, J.L.A., Horita, G.I., and Yoshimura, H.N., 2003, "Sintering behavior of aluminum nitride doped with Y₂O₃," *Materials Science Forum*, 416-418, pp. 591-596.
- [21] Zarinejad, M., and Drew, R.A.L., 2002, "Second phase evolution in a yttria-sintered aluminum nitride ceramic," *Materials Science Forum*, 383, pp. 55-70.
- [22] Chernetskaya, M. D., Glotov, D.V., Popova, N.A., Sarkisyan, T.M., and Kuznetsova, I.G., 1994, "Effect of yttrium compounds on sintering of aluminum nitride," *Glass and Ceramics*, 51(1-2), pp. 78-80.
- [23] Qiao, L., Zhou, H., Xue, H., and Wang, S., 2003, "Effect of Y₂O₃ on low temperature sintering and thermal conductivity of AlN ceramics," *Journal of the European Ceramic Society*, 23, pp. 61-67.

- [24] Komatsu, M., and Kimiya, M., 2010, "High thermal conductive aluminum nitride sintered body," France.
- [25] Troczynski, T. B. a. N., P.S., 1989, "Effect of additives on the pressureless sintering of aluminum nitride between 1500 °C and 1800 °C," *Journal of American Ceramics Society*, 7(8), pp. 1488-1491.
- [26] Patrick, E. P., 1975, "Vacuum brazing of aluminum," *Welding Journal*, pp. 159-163.
- [27] Miller, C. J., 1968, "Fluxless Aluminum Brazing," United States.
- [28] Miller, C. J., 1967, "Aluminum Brazed Article," United States.
- [29] Terrill, J. R., Cochran, C.N., Stokes, J.J., and Haupin, W.E., 1971, "Understanding the mechanisms of aluminum brazing," *Welding Journal*, 50, pp. 833-839.
- [30] Liu, J., Huang, X., Li, Y., Sulieman, K.M., He, X., and Sun, F., 2006, "Hierarchical nanostructures of cupric oxide on a copper substrate: controllable morphology and wettability," *Journal of Materials Chemistry*, 16, pp. 4427-4434.
- [31] Wenzel, R., 1936, "Resistance of solid surfaces to wetting by water," *Industrial and Engineering Chemistry*, 28(8), pp. 988-994.
- [32] Wilson, C., Borgmeyer, B., Winholtz, R.A., and Ma, H.B., 2008, "Visual observation of the oscillating heat pipes using neutron radiography," *Journal of Thermophysics and Heat Transfer*, 22(3), pp. 366-372.
- [33] Borgmeyer, B., Wilson, C., Winholtz, R.A., Ma, H.B., Jacobson, D., and Hussey, D., 2010, "Heat transport capability and fluid flow neutron radiography of three-dimensional oscillating heat pipes," *Journal of Heat Transfer*, 132.
- [34] Hussey, D. S., Jacobson, D.L., Arif, M., Huffman, P.R., Williams, R.E., and Cook, J.C., 2005, "New neutron imaging facility at the NIST," *Nuclear Instruments and Methods in Physics Research A*, 542, pp. 9-15.
- [35] Lafuma, A., and Quere, D., 2003, "Superhydrophobic states," *Nature Materials*, 2, pp. 457-460.

- [36] Cassie, A. B. D., and Baxter, S., 1944, "Wettability of porous surfaces," Transactions of Faraday Society, 40(546-551).
- [37] Taylor, G. I., 1961, "Deposition of a viscous fluid on the wall of a tube," Journal of Fluid Mechanics, 10, pp. 161-165.
- [38] Zhang, F. Z., Winholtz, R.A., Black, W.J., Wilson, M.W., Taub, H., and Ma, H.B., 2015, "Effect of hydrophilic nanostructured cupric oxide (CuO) surfaces on the heat transport capability of a flat plate oscillating heat pipe."
- [39] Wilson, C., Borgmeyer, B., Winholtz, R.A., Ma, H.B., Jacobson, D., and Hussey, D., 2011, "Thermal and Visual Observation of Water and Acetone Oscillating Heat Pipes," Journal of Heat Transfer, 133(6), pp. 061502-061505
- [40] Fairbrother, F., and Stubbs, A.E., 1935, "Studies in electro-endosmosis. Part VI. The "bubble-tube" method of measurement," Journal of the Chemical Society, pp. 527-529.
- [41] Bretherton, F. P., 1961, "The motion of long bubbles in tubes," Journal of Fluid Mechanics, 10, pp. 166-188.
- [42] Aussillous, P. a. Q., D., 2000, "Quick deposition of a fluid on the wall of a tube," Physics of Fluids, 12(10), pp. 2367-2371.
- [43] Han, Y., and Shikazono, N., 2009, "Measurement of the liquid film thickness in micro tube slug flow," International Journal of Heat and Fluid Flow, 30, pp. 842-853.
- [44] Triplett, K. A., Ghiaasiaan, S.M., Abdel-Khalik, S.I., and Sadowski, D.L., 1999, "Gas-liquid two-phase flow in microchannels-Part I: two-phase flow patterns," International Journal of Multiphase Flow, 25, pp. 377-394.
- [45] Smoot, C. D., 2013, "Factors affecting oscillating motion and heat transfer in an oscillating heat pipe," PhD, University of Missouri.

- [46] Smoot, C. D. a. M., H.B., 2014, "Experimental investigation of a three-layer oscillating heat pipe," *Journal of Heat Transfer*, 136, pp. 051501-051506.
- [47] Yang, H., Khandekar, S., and Groll, M., 2008, "Operational limit of closed loop pulsating heat pipes," *Applied Thermal Engineering*, 28, pp. 49-59.
- [48] Ma, H. B., Borgmeyer, B., Cheng, P., and Zhang, Y., 2008, "Heat transport capability in an oscillating heat pipe," *Journal of Heat Transfer*, 130.
- [49] Ma, H. B., Hanlon, M.A., and Chen, C.L., 2006, "An investigation of oscillating motions in a miniature pulsating heat pipe," *Microfluid Nanofluid*, 2, pp. 171-179.
- [50] Shafii, M. B., Faghri, A., and Zhang, Y., 2002, "Analysis of heat transfer in unlooped and looped pulsating heat pipes," *International Journal of Numerical Methods for Heat and Fluid Flow*, 12(5), pp. 585-609.
- [51] Zhang, Y., Faghri, A., and Shafii, M. B., 2002, "Analysis of Liquid–Vapor Pulsating Flow in a U-shaped Miniature Tube," *International Journal of Heat and Mass Transfer*, 45(12), pp. 2501-2508
- [52] Zhang, Y., and Faghri, A., 2002, "Heat Transfer in a Pulsating Heat Pipe with Open End," *International Journal of Heat and Mass Transfer*, 45(4), pp. 755-764
- [53] Zuo, Z. J., North, M. T., and Wert, K. L., 2001, "High Heat Flux Heat Pipe Mechanism for Cooling Of Electronics," *IEEE Transactions on Components and Packaging Technologies*, 24(2), pp. 220-225.
- [54] Washburn, E. W., 1921, "The dynamics of capillary flow," *The Physical Review*, 18(3), pp. 273-283.
- [55] Blake, T. D. a. H., J.M., 1969, "The kinetics of liquid/liquid displacement," *Journal of Colloid and Interface Science*, 30(3), pp. 421-423.
- [56] Dussan V., E. B., 1979, "On the spreading of liquids on solid surfaces: static and dynamic contact lines," *Annual Review of Fluid Mechanics*, 11, pp. 371-400.
- [57] Hoffman, R. L., 1983, "A study of the advancing interface II. Theoretical prediction of the dynamic contact angle in liquid-gas systems," *Journal of Colloid and Interface Science*, 94(2), pp. 470-485.

- [58] Hoffman, R. L., 1975, "A Study of the Advancing Interface: I. Interface shape in liquid-gas systems," *Journal of Colloid and Interface Science*, 50(2), pp. 228-241.
- [59] Cox, R. G., 1986, "Dynamics of the spreading of liquids on a solid surface. Part 1. Viscous flow.," *Journal of Fluid Mechanics*, 168, pp. 169-194.
- [60] Shikhmurzaev, Y. D., 1997, "Moving contact lines in liquid/liquid/solid systems," *Journal of Fluid Mechanics*, 334, pp. 211-249.
- [61] Shikhmurzaev, Y. D., 1993, "The moving contact line on a smooth solid surface," *International Journal of Multiphase Flow*, 19(4), pp. 589-610.
- [62] Shikhmurzaev, Y. D., 1994, "Mathematical modeling of wetting hydrodynamics," *Fluid Dynamics Research*, 13, pp. 45-64.
- [63] Joos, P., Van Remoortere, P., and Bracke, M., 1990, "The kinetics of wetting in a capillary," *Journal of Colloid and Interface Science*, 136(1), pp. 189-197.
- [64] Popescu, M. N., Ralston, J., and Sedev, R., 2008, "Capillary rise with velocity-dependent dynamic contact angle," *Langmuir*, 24(21), pp. 12710-12716.

VITA

Feng Zhao Zhang or Tom Zhang was born in Fuzhou, China in 1989. He immigrated to the United States in New York in 1995. He spent his childhood in Fort Payne, Alabama and graduated from Fort Payne High School as the Salutatorian in 2008. He first went to Auburn University in Alabama from 2008-2009, but later transferred to the University of Missouri to finish his Bachelor of Science in Mechanical Engineering in 2011. While in undergraduate studies, he started honors research in 2010 and joined Dr. Ma's lab with the topic of studying fabrication methods to create an aluminum nitride oscillating heat pipe. Upon graduation Tom got accepted to the Integrative Graduate Education and Research Traineeship ("IGERT") program where he is subsidized for two years towards his PhD. His dissertation focused primary on the nanostructured surface effects on flat plate oscillating heat pipes. Currently Tom is working at a startup consulting firm called Optimus Process Solutions as the process engineering advisor.